2021

Analysis and Design of Infrared Fiber Bundles for Large Field-of-View Thermal Imaging

Cesar A. Lopez-Zelaya
University of Central Florida

ANALYSIS AND DESIGN OF INFRARED FIBER BUNDLES FOR LARGE FIELD-OF-VIEW THERMAL IMAGING

by

CESAR A. LOPEZ-ZELAYA

A thesis submitted in partial fulfillment of the requirements
for Honors in the Major Program in Photonic Science and Engineering
in the College of Optics and Photonics (CREOL)
and in the Burnett Honors College
at the University of Central Florida
Orlando, Florida

Spring Term
2021

Thesis Chair: C. Kyle Renshaw

Abstract

During the DARPA SCENICC program, J. Ford, et al., demonstrated that CFBs provide a compelling route to compact, wide angle imagers. Monocentric lenses readily provide diffraction-limited images over wide field but onto a hemispherically curved image surface. They demonstrated visible CFBs can be tapered, cut and polished to relay curved images to flat sensors. We have shown that this provides a volumetric imaging efficiency a hundredfold larger than bulk optics can produce; a hundred times the resolution in the same volume or a hundred times less volume for the same resolution. Ford's work leveraged commercial fiber bundles available for the visible spectrum based on silica. We have developed hybrid fiber bundles using step-index confinement between chalcogenide glass cores and polymer cladding with high index-contrast. The high contrast is necessary to provide tight confinement to the high-index As-Se core with minimal crosstalk between closely spaced cores. Tight confinement also minimizes absorption losses in the PEI polymer cladding. The high contrast of this system also provides a large NA to optimize coupling into the CFB from fast lenses. We introduce disorder into the core radius as a mechanism to further decouple adjacent cores, reduce crosstalk and increase fill-factor. We present coupled-mode theory, modal crosstalk superposition, and finite-element modelling to quantify coupling losses and crosstalk as a function of geometry and disorder. We fabricated preforms, drew small fiber bundles and characterized optical properties of the bundles to aid scale-up to megapixel MWIR CFBs.

DEDICATION

With the hopes that this work will help advance the field of optics in some way or another, I dedicate this thesis to all scientists and engineers who discover the secrets of the universe one photon at a time.

In memory of a great friend, who lived driven by curiosity and love for his family, friends, and science.

“memento mori” -Ethan Hall

Above all, I dedicate this work to God.

ACKNOWLEDGEMENTS

A big thank you to Dr. C. Kyle Renshaw, Dr. Rodrigo Amezcua-Correa, and Dr. Christian Keyser, who believed in me and gave me the opportunity to be challenged and learn.

To, Li Zhang, for being a great colleague and helping with many of the findings presented in this work.

To our collaborators: Joshua Kaufman, Felix Tan, and Anthony Badillo. Without their advice and expertise in infrared fiber drawing, this project would not have been possible.

To my family: Ale, Vale, Kenya, Cesar, and Betsy, who encouraged me to follow my dreams and inspired me each and every day.

Special thanks to the Air Force Research Laboratory (AFRL) and the National Science Foundation (NSF) Multi-functional Integrated System Technology (MIST) Center for funding this project.

Table of Contents

Table of Figures

Chapter 1: Introduction

1.1 Thermal imaging and applications

A little over two centuries ago, infrared radiation was discovered by Sir William Herschel in the year 1800 [1]. This was an unintentional discovery since Herschel was testing different eye-protecting filters to be able to observe sunspots. He noticed that, for some of the filters, the sensation of heat was more noticeable. Then, he performed an experiment to test this phenomenon by using a prism to disperse light and measure the temperature produced by different colors. He found out that from blue to red, colors would register increasing temperatures. However, this did not stop at the point where red light ended. Higher temperatures could be registered beyond red light, which indicated that there was an invisible form of radiation beyond what was visible [2]. Hence, why this type of "invisible light" is called infrared (IR) light; this word has the Latin prefix infra-, which means below, and red, for the last color that can be seen by our eyes before the IR.

Following the discovery of this new type of radiation, development of IR technologies was extremely slow and primarily aimed at applications in astronomy [3]. It was not until 1929 when the Hungarian physicist Kalman Tihanyi invented the IR-sensitive electronic television camera for anti-aircraft defense in Britain [4]. This slowly led to the expansion of IR technologies in defense, medicine, and industry [5]–[9]. What makes the IR spectrum so attractive is that it enables us to see what would otherwise be impossible to see with the naked eye and beyond; it enables the detection of heat signatures, characterization of materials and chemicals via spectroscopic techniques, studying the universe more in depth, and seeing through degraded environments and in the dark with night vision.

All of the colors that we see and bring to our world are part of the infrared spectrum. The small section of radiation that our eyes can see, from blue to deep red, is called the visual spectrum and it spans the wavelength range of $0.4 - 0.7\mu m$. Then, the IR regime starts at the longer-wavelength edge of the

visible spectrum (deep red, $\sim 0.7\mu m$ wavelength) and goes all the way to the radio-wave range (~1mm wavelength) [10]. In fact, the IR spectrum is so large that it has to be divided into sub-categories, each having its own unique applications. First, the near-IR (NIR) spans the $0.7 - 1.1\mu m$ wavelength range. NIR radiation is detectable by silicon [11] and image intensifiers are sensitive in this region. Thus, making it possible for this section of the IR spectrum to be used for night and IR "x-ray" vision [12]. Second, the short-wavelength IR (SWIR) spans the $1.1 - 3\mu m$ wavelength range where, in addition to operating in the NIR, image intensifiers and long-distance telecommunication in the O- $(1.25 - 1.36\mu m)$, E- $(1.36 - 1.46\mu m)$, S- $(1.46 - 1.53\mu m)$, C- $(1.53 - 1.565\mu m)$, L- $(1.565 - 1.625\mu m)$, and U- $(1.625 - 1.675\mu m)$ bands is dominant because of ultra-low loss in silica glass [13].

Deeper into the IR spectrum, there are two important bands for imaging and sensing. These bands exhibit high transmission through the atmosphere because they are far from vibrational transitions of carbon dioxide, water vapor and ozone. Figure 1 displays the atmospheric transmission [14]; overlays show the mid-wavelength IR (MWIR) band at $3 - 5\mu m$ and the long-wavelength IR (LWIR) band, typically considered $8 - 12\mu m$. These parts of the electromagnetic spectrum are called the "thermal imaging" regions due to sensors being able to detect light based on thermal emissions, making it possible to image objects and scenes without the need of the sun or an IR light source to be present [5], with the added benefit of being able to see through the atmosphere at long range. Applications that benefit from this are mostly military-related, such as target acquisition, fire control, aerial navigation, surveillance, and intelligence gathering [15]. Lastly, the far IR (FIR) region is the deepest part of the IR spectrum, spanning the $15 - 1000\mu m$ wavelength range, but its applications are beyond the scope of this text.

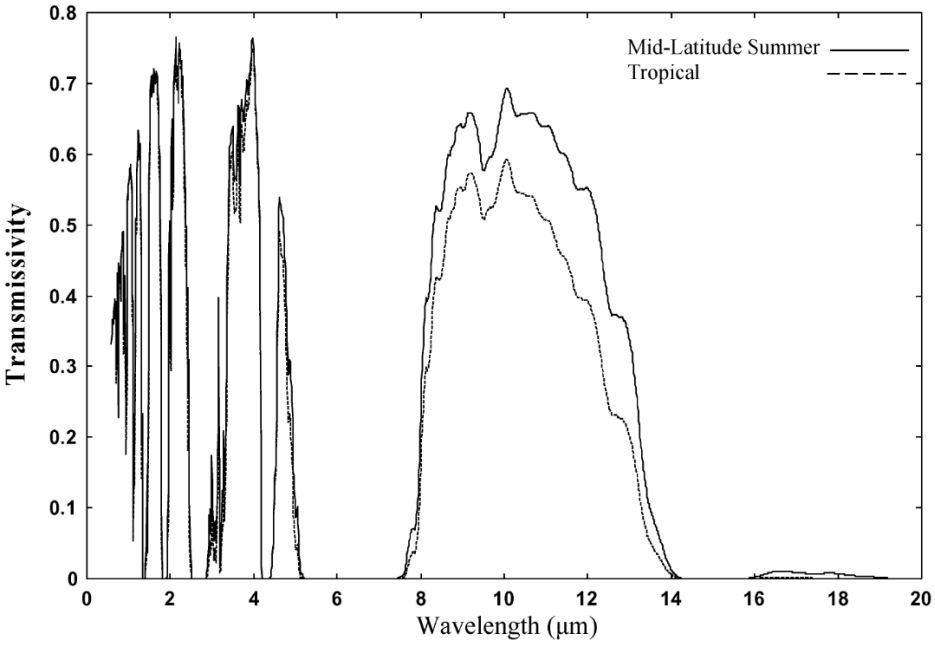

Figure 1: Transmission of IR radiation in the atmosphere during mid-latitude summer and tropical conditions. Image obtained from [14].

1.2 Challenge of wide-angle imaging

Designing and analyzing imaging systems is a laborious task [16], even with specialty software such as ZEMAX and Code V that provide extensive tools designers use to optimize lens characteristics for a specific application. Unfortunately, there is no perfect lens or a one-size-fits-all solution in lens design; that is because there are so many degrees of freedom and characteristics to consider in a typical design problem. Driving characteristics are typically focal length, image size, field-of-view (FOV), and wavelength range; while things like f-number, resolution, size, and cost are optimized according to a merit function reflecting their relative importance. Low size, weight, and cost (SWaC) imagers with the widest FOV possible are paramount to many surveillance applications [17]. The wider the FOV, the larger the angle that can be resolved by the imaging system. This results in an easier and more effective characterization of objects and scenes.

Achieving this is not easy, however. Wide FOV devices tend to be very intricate, consisting of a large number of lenses which are hard to cram inside of a compact imager [18], [19]. This becomes an obstacle in developing wide-angle imagers with low SWaC, especially in the IR where special materials such as silicon, germanium, and metal salts (ZnSe, ZnS, MgF2, BaF2, etc.) are needed to transmit light effectively through the system [20]–[22]. Optics used for this are roughly 10x more expensive than their visible counterparts made of glass, but plastic optics for IR imaging are slowly but surely emerging [23].

These devices also suffer from (and must be carefully designed to avoid) aberration effects, which are a property of the optical system that cause light to spread out instead of focusing at a point. The six most common types of aberrations are: defocusing, spherical aberration, coma, astigmatism, image distortion, and field curvature [24], [25]. Aberrations cause undesirable effects that can sometimes be detrimental to image quality and resolution, but systems can be engineered to mitigate these effects. The sixth aberration mentioned is the most drastic and is also known as Petzval field curvature [25]. This type of aberration occurs when a flat object normal to the optical axis (i.e. a photodetector) cannot be brought properly into focus on a flat image plane at wider angles [26], [27]. To address this effect for an optical system, one must first ensure that the Petzval sum

$$P_{sum} = \sum_{i} \frac{n_{i+1} - n_i}{r_i n_{i+1} n_i}, \tag{1.1}$$

where r_i is the radius of the ith surface and n is the refractive index of the first and second side of the specific surface, equals zero [28]. Most, if not all, commercially available imaging sensors are flat, so after field curvature is corrected, all the other aberrations are addressed.

We have developed a new, fundamental metric to characterize imaging systems in terms of their size and resolution - the volumetric imaging efficiency (VIE) [29], [30]. This tool is extremely useful in describing the compactness of an imager against the fundamental limits imposed by diffraction as well as

quantifying the overall size and complexity of an imaging system. By computing the VIE for hundreds of imaging systems, we have shown that as the FOV increases so does system size and complexity, thus resulting in a lower VIE. This can be seen in Figure 2, which shows an exponential reduction in efficiency with increasing FOV. Introducing a curved focal plane has shown that ultra-wide FOV with low SWaC (or at least, smaller overall imager size) is possible, even in the IR spectrum [30]–[33].

Efforts have been made by DARPA to develop technology for enabling the fabrication of curved image sensors with programs like HARDI in 2008 and FOCII in 2020 along with others to utilize curved image surfaces (AWARE and SCENICC both ~2010) [34]–[37].

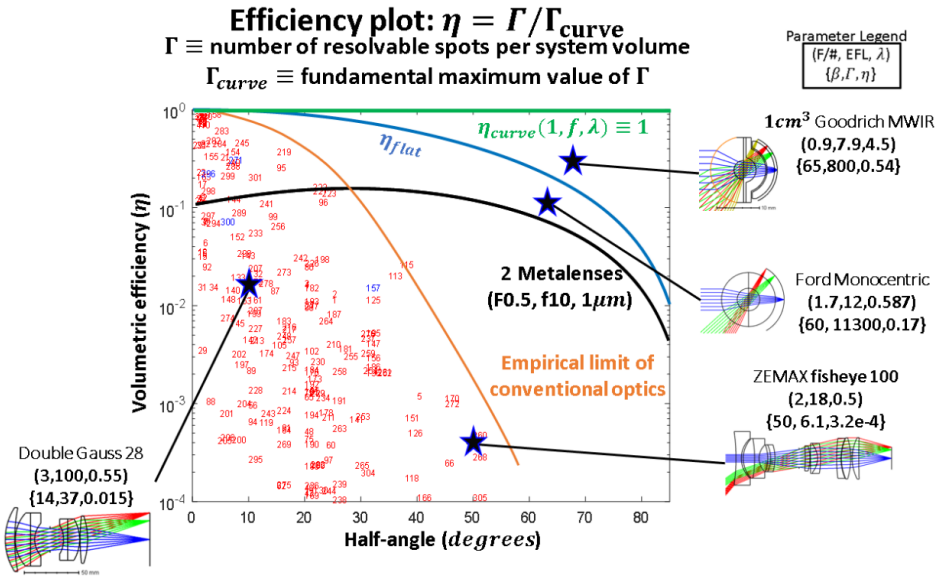

Figure 2: Volumetric imaging efficiency (VIE) for different lens designs. Numbers in the plot represent conventional lenses using homogenous, bulk optics. The orange line represents the empirical limit of conventional optics that degrades as field-of-view (FOV) increases. Stars represent the data of systems illustrated outside of the plot. Note, the outliers "Goodrich MWIR" and "Ford Monocentric" take advantage of curved sensor technologies to surpass the conventional limit. The black line shows optimization results of using two metasurfaces with different FOV. The

blue curve and the flat green line represent the fundamental upper limits of idealized flat and curved imagers, respectively.

The ability to fabricate a curved image sensor is difficult and time-consuming because expensive current device patterning techniques cannot be used with nonplanar substrates [38]. Several attempts at making a curved sensor have been made [39]–[41] with the most promising example coming out of Hughes Research Lab using thinned back-side illuminated CMOS to achieve 30 degrees of curvature [42], but a practical alternative to curving image sensors is to use coherent fiber bundles (CFBs) to relay curved images to flat sensors. One great example of a CFB made for wide-angle imaging in the visible spectrum was developed Ford et al. in 2013 as part of the SCENICC program [43] and shown in Figure 3. This provides the optical advantages of imaging onto a curved surface with a much easier and more cost-effective approach.

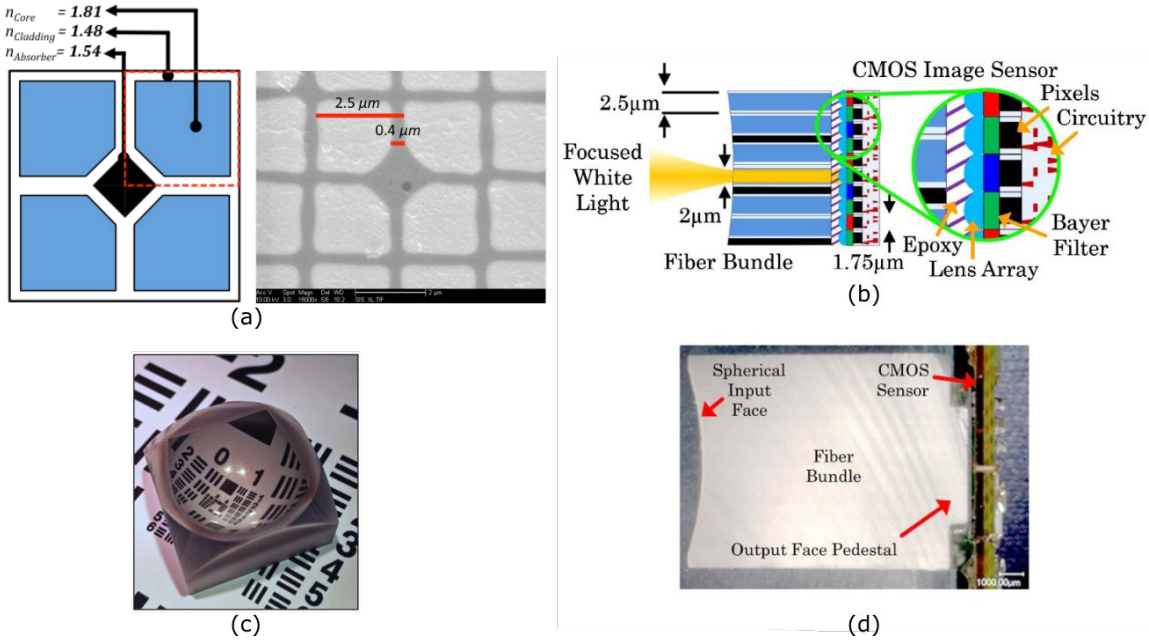

Figure 3: Coherent fiber bundle (CFB) developed by Ford et al. in 2013 as part of the SCENICC program. Diagram of the CFB's cross-section showing the refractive index of the core, cladding, and absorptive element compared to a scanning-electron microscope image of a manufactured bundle showing a ~2.5μm pitch between cores (a).

Diagram showing that same bundle coupled to a detector and light being focused into it (b). Macroscopic image of curved CFB showing image of target under it (c). Actual longitudinal cross-section of the bundle coupled to an image detector (d), note the spherical input surface for wide-angle imaging. Images obtained from [44]–[46].

1.3 Coherent fiber bundles

As the name implies, CFBs are made up of thousands of optical fiber cores (where light is confined and guided by total internal reflection) placed in a common cladding. The word "coherent" in CFBs is different than what is usually referred to as coherent in optics, i.e., optical coherence of a field of light. In the context of CFBs, coherent refers to the order in which the fibers are placed. A bundle is most coherent when the fibers are ordered in such a way as to have both ends be identical and images cast on a CFB remain the same at all points along the bundle as seen in Figure 4.

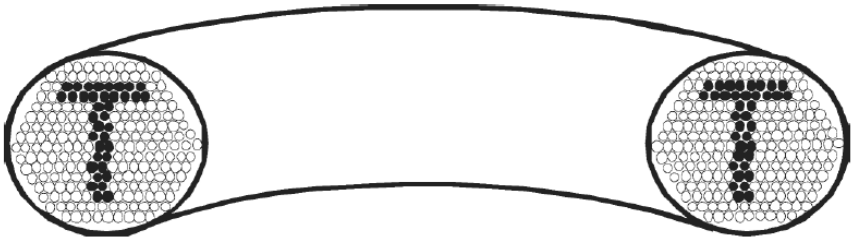

Figure 4: Bundle of fibers showing coherent alignment from end to end. Image obtained from [47].

The CFB used by Ford et al. consisted of thousands of small ~2.2μm square-shaped cores separated by a ~0.30μm cladding gap. Index-matched absorptive glass was also included in the cladding to suppress light from tunneling through there. With cores having a refractive index of 1.81 and the cladding an index of 1.48, the numerical aperture of the individual fibers was really high. Doing this enables CFBs to confine light within small diameter cores while keeping them close together as needed to relay high-resolution images [48]. Simply put, the individual optical fibers that make up the CFB can be thought of as extruded pixels that can be tapered and bent to accommodate a certain shape or curvature. Thus, acting like curved

detectors that are much easier to manufacture and offer significant performance gains over conventional flat detectors. This can be seen in Figure 5.

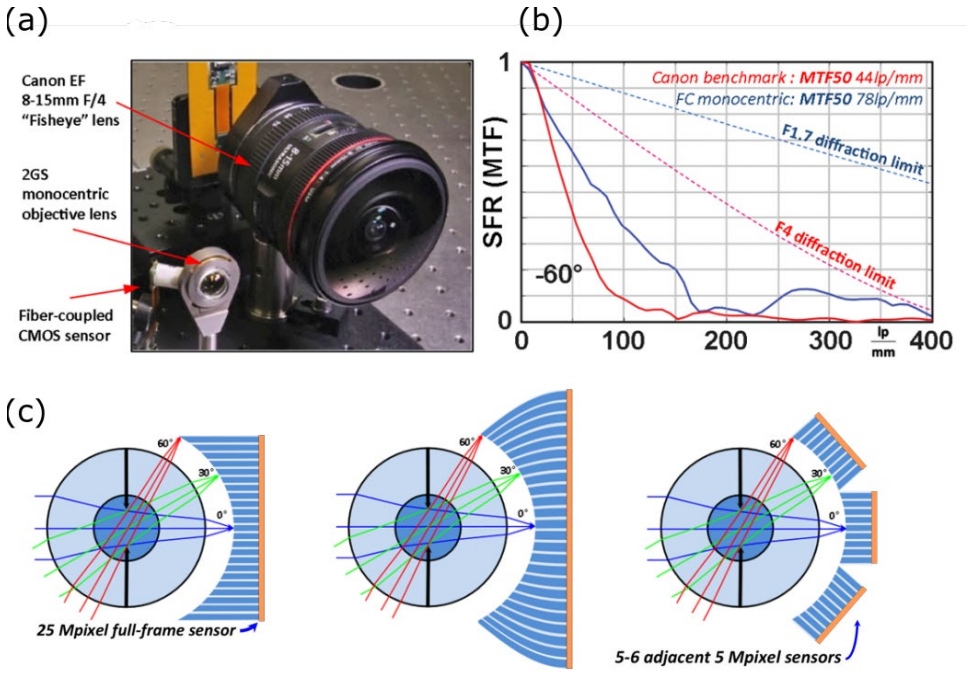

Figure 5: Conventional wide-angle fisheye lens system compared to a fiber-coupled two-glass symmetric (2GS) lens system (a). The modulation transfer function (MTF) plot (b) shows performance improvement for the fiber-coupled system despite it being 10x smaller in volume. Different coherent fiber bundle (CFB) architectures are presented (c). These show how having curvature in a CFB acts as a curved focal plane while being exceptionally good at capturing light at wide angles [49].

1.4 Materials and types of fibers for IR CFBs

Despite how well CFBs have performed in the visual spectrum [49], this has been difficult to translate to the IR. There have been several attempts to make CFBs that operate in this regime [50]–[57], but there are a number of fundamental differences that make this a challenge, such as: needing larger-sized cores due to longer wavelengths, higher intrinsic losses, and lack of mechanical robustness [47]. Silica glass has become the standard in optical fiber telecommunication since it has an excellent transmission in the

NIR and SWIR. However, at wavelengths longer than ~1.6μm, intense infrared absorption occurs due to vibrational resonances [58]. This motivated the search for materials that transmit better in the IR and ways of confining light by using silica to "trap" it in a hollow core where it has very minimal contact with the glass cladding.

With silica being such an excellent material for use in optical fibers due to its transmission properties and mechanical robustness, other ways of transmitting light beyond ~1.6μm with it have been investigated. An approach to this problem was to construct hollow-core fibers with metallic coatings at the edges of the core [59]. This same principle was used to manufacture a silica-based CFB made up of 100μm cores coated with silver and a silver iodide film to transmit in the IR with the added benefit of having similar mechanical properties to conventional silica fibers [60]. Light can be guided through these fibers with minimal losses, as long as the core diameter is kept large and the appropriate metallic film thickness is used to prevent absorption losses [61].

By using the concept of guiding light in a hollow core, silica-only hollow-core fibers were devised. Without using metal films at the core-cladding boundary, the efficient transmission of light is possible by taking advantage of two mechanisms that "trap" light in the core while making very little contact with the cladding glass. The two types of fibers that do this are photonic bandgap (PBG) fibers and negative-curvature anti-resonant reflecting optical waveguides (ARROWs) [62], [63]. PBG fibers transmit light by using the photonic bandgap effect, where only certain frequencies forbidden to propagate in the fiber's cladding are confined in the core [64]. Thus, only narrow frequency bands are allowed to propagate, while the rest leak out. ARROWs, on the other hand, rely on anti-resonant reflections from the cladding structure, which means that the frequencies allowed to propagate in the core are trapped there due to destructive interference that occurs at the thin glass interfaces of the cladding, similar to what occurs in a Fabry-Perot cavity. Thus, while resonances in a Fabry-Perot cavity are narrow-band, antiresonances are spectrally broad [65]. An important characteristic of these fibers is that as long as the geometrical arrangement of the

cladding permits light to be trapped in the core, negative curvature can be used to further reduce the amount of light that is in contact with the glass, thus reducing material-related losses [66]–[68].

Both of these fiber types are very promising because they are not hard to manufacture, are made with only silica glass, and can transmit well up to the MWIR [66]. Beyond that, confinement and material losses start increasing to the point where they become significant. Between these two fibers, only ARROWs have been used to make an IR CFB for relaying images (to our knowledge and more than likely because PBG fibers require a special arrangement of inclusions in the cladding, making them hard to have cores together) [69]. One major drawback with the CFB shown in [69] is that the cores had to be kept large to reduce confinement losses and were coupled, which means that light in one core leaks out to other cores as it propagates. This directly impacts resolution since larger core sizes and the spacing between them degrade image quality (i.e. less lines/mm are resolvable). However, due to the design freedom that ARROWs provide and the properties of the guidance mechanism, we were able to come up with a novel negative-curvature deign with the aim of improving what was shown in [69].

To effectively confine light in the MWIR, this novel hollow-core fiber design consists of the following three parameters that determine its transmission. First, a small core diameter of $50\mu m$ to maximize resolution if a bundle of these fibers is made. Using a smaller diameter would increase the confinement losses drastically. Then, $8.7\mu m$ wide (measured radially) hollow capillaries were included to further reduce confinement losses and introduce negative curvature. Lastly, the third parameter was the $1.3\mu m$ thickness of the glass struts that make up the capillaries. The thickness of the struts, which determines the position of the lossy resonant peaks, can be determined by using

$$\lambda_k = 4t\frac{\sqrt{n^2 - 1}}{2k + 1}, \tag{1.2}$$

where λ_k is the guided wavelength that lies between resonant loss peaks, n is the refractive index of the glass, t is the thickness of the struts, and $k = 0,1,2,...$ is the anti-resonant window integer (where $k = 0$ corresponds to the first and largest anti-resonant widow) [70]. With the parameters presented here, the next step was to calculate the loss [71]. To begin, the confinement loss in dB/m is given by

$$CL(\lambda) = 6.686 \cdot Im[n_{eff}(\lambda)] \cdot k_0(\lambda), \tag{1.3}$$

where 6.686 is the neper, $Im[n_{eff}(\lambda)]$ is the imaginary part of the mode's effective index (mode theory is discussed more in depth in chapter 2), and $k_0(\lambda)$ is the free-space wave number. The material absorption loss in dB/m is given by

$$AL(\lambda) = \alpha_d(\lambda)FOPS(\lambda), \tag{1.4}$$

where $\alpha_d(\lambda)$ is the glass's absorption coefficient in dB/m and $FOPS(\lambda) = \int_{S_d}|P_z|dS/\int_{S_\infty}|P_z|dS$ is the fraction of power in silica (where S_d is the glass-only cross section, S_∞ is the entire fiber cross section, and P_z is the longitudinal component of the mode's Poynting vector). Note, surface scattering loss also plays a role, but may be neglected in the IR. Adding up these two loss contributions yields the total loss . Finally, with the information presented here, a negative-curvature ARROW was designed and improved after rigorous numerical simulations using the finite-element (FEM) method solver COMSOL Multiphysics and the results are show in Figure 6.

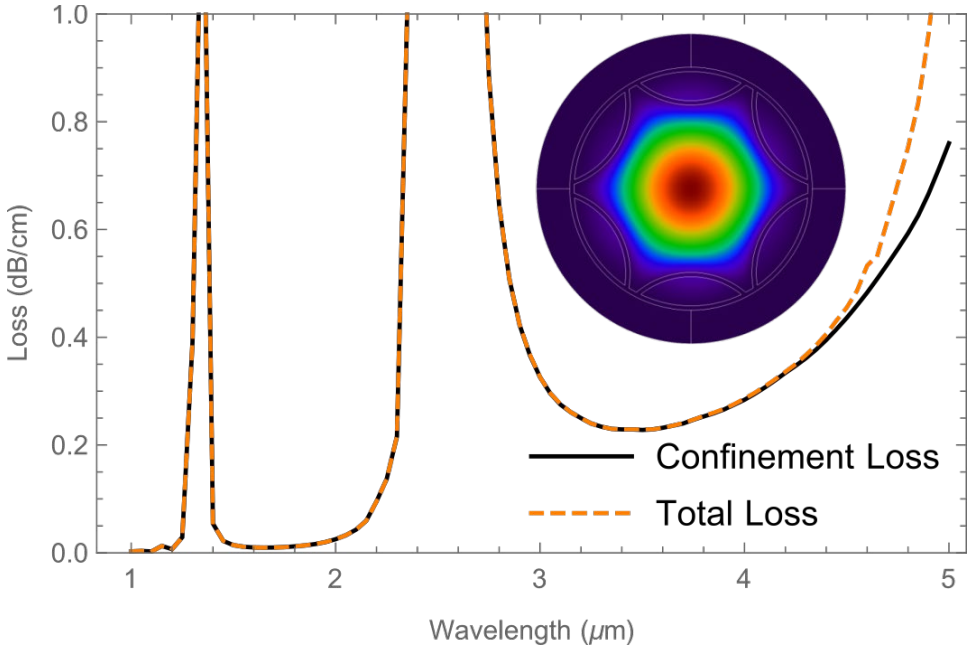

Figure 6: Silica glass-based hollow-core anti-resonant reflecting optical waveguide (ARROW) designed with a core diameter of $50\mu m$*, capillary width of* $8.7\mu m$*, and strut thickness of* $1.3\mu m$ *for transmitting in the MWIR. Confinement losses for the fundamental mode resulting from light "leaking" out while guided through the ARROW and the total loss, which accounts for silica's absorption, are plotted. As expected, results show a transmission window that spans the entirety of the MWIR and for all guided wavelengths the material absorption was low because the fraction of power in silica (FOPS) was less than 0.1%.*

ARROWs enable efficient fibers despite silica's hefty loss in the MWIR and LWIR. However, the geometries needed to achieve a proper transmission in the IR would make a bundle have a bundle have a pitch much larger than the small $10\mu m$ pitch required for state-of-the-art sensors. Aside from using hollow-core fibers, there is a third method of guiding light (hinted to it earlier on) that it is the most reliable and has been used the most for making CFBs. This method only works with solid-core fibers and is called total internal reflection. It can easily be described by using ray optics and the critical angle condition

$$\theta_{crit} = \sin^{-1}\left(\frac{n_{clad}}{n_{core}}\right), \tag{1.5}$$

where θ_{crit} is the critical angle, n_{clad} is the refractive index of the cladding, and n_{core} is the refractive index of the core. Equation (1.5) states that any ray of light that is incident onto the core-cladding boundary of an optical fiber at an angle greater than $90° - \theta_{crit}$, with respect to the fiber's cladding, will leak out. More of this will be covered in chapter 2 and there are several kinds of solid-core fibers, but in this text we will only concentrate on step-index fibers.

In comparison to ARROWs, these fibers can have cores with diameters of the same length as the longest wavelength that they are to guide. These fibers may also be placed in close proximity to one another, making them ideal candidates for making high resolution CFBs. In the 1960s the first chalcogenide glass (ChG) fibers made of arsenic trisulfide were reported by N. S. Kapany [72]. ChG fibers are typically composed of two or more chalcogen elements, some of which include As, Ge, Sb, P, Te, Se, and S. When these materials are mixed together in an oxygen-free environment, very stable and simple glasses result. A great advantage of using these glasses over conventional oxide glasses, like silica, is that their intrinsic losses are not as severe; the intrinsic losses can be attributed to the Urbach tail, Rayleigh scattering, and multiphonon absorption [47]. Now, extrinsic losses of ChGs are the dominant loss mechanisms and can sometimes be detrimental; these include impurity losses and those arising from scattering. The most significant source of loss in ChGs comes from hydrogen-based impurities, but can be reduced substantially by purifying the glasses properly [47]. One major drawback of using these materials, however, is their lack of mechanical robustness and tendency to crystalize [47], [73].

ChG fibers started gaining traction in many IR applications years after Kapany first presented his first draws. In fact, the from first time that ChG fibers were reported by him, they were assembled into imaging cones, fused plates, field flatteners, and image dissectors; all of these being CFBs used to transmit and manipulate images in the IR. Thus, showing the ease and versatility of using ChG glasses for imaging applications. As fabrication methods improved, it was found that by drawing ChG fibers with a polymer

cladding, their strength was vastly improved too [74]–[76]. Making these fibers ideal to many IR applications in high-power laser pulse delivery, sensing, and imaging [77]–[79].

1.5 CFB Requirements

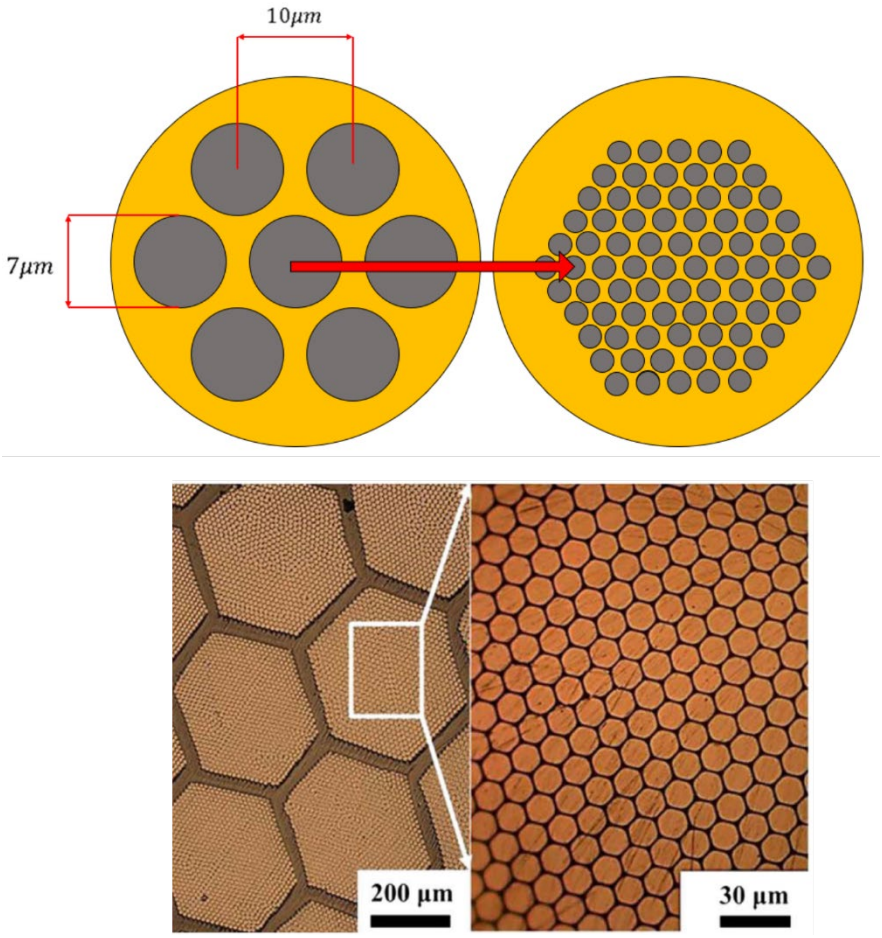

Figure 7: Diagram showing how chalcogenide glass (ChG) cores (diameter of 7μm) with a polymer cladding fit into a six-core unit cell with pitch of 10μm (center). A more intricate multi-core bundle made up of unit cells used for imaging applications and resembles the arrangement of pixels on a sensor (top). Actual high-resolution ChG fiber bundle for the MWIR made up of 810,000 single fibers of 9μm in diameter and a polymer cladding with a 10μm outer diameter, reported by [54].

In this work, ChG fibers were investigated as viable candidates to be used in high-resolution IR transmitting CFBs with $> 1000 \times 1000$ or $>$ million cores to devise the first fiber-based curved IR focal plane. Rigorous theoretical analyses were done by using the FEM and coupled-mode theory to evaluate the performance of these fibers individually and when placed in close proximity to others [80]–[84]. Since the goal of making curved IR CFBs is to improve the FOV and VIE of imaging systems, additional care was taken to not impact the resolution. Two important design constraints considered from the very beginning were: a small core diameter of 7μm and a pitch (center-to-center spacing) of 10μm, as it can be seen in Figure 7, to match the CFB with high-resolution IR image-sensors. This ensures that the cores match the sizes of high-resolution IR camera pixels and that from the beginning of all analyses, the amount of potential crosstalk could be considered.

Step-index hybrid ChG with polymer fibers with small cores were developed and theoretically evaluated. $Ge_{30}As_{13}Se_{32}Te_{25}$ and As_2Se_3 were the glasses chosen for these fibers due to their similar and excellent transmission properties in the MWIR and LWIR range, their ability to be co-drawn with low-index polymers (fluorinated ethylene propylene and polyetherimide), their high refractive index, and a higher tolerance to crystallization during the drawing process due to their tellurium and selenium content, respectively [47]. Thus, enabling for the design of an excellent CFB for IR imaging applications. More details about considerations, expectations, designs, and results will be discussed more in detail in this thesis.

Chapter 2: Optical Waveguide Theory

Designing an IR CFB requires an extensive set of different mathematical methods and knowledge of electricity and magnetism. This chapter is dedicated to that. The complex subject of light propagation and coupling in optical waveguides will be broken down into its simpler parts and presented in an elegant and straightforward way. Meaning that many, but not all, steps will be given towards solving a specific problem so that the reader can follow along and understand where some of the equations come from. Plenty of references where longer and more in-depth derivations are carried out will be given so that the reader may learn more if needed. We begin this chapter by introducing Maxwell's equations, then diving into guided modes of slab waveguides and optical fibers, which then lead to coupled-mode theory, and a more "complete" way of looking at crosstalk in imaging bundles towards the end.

2.1 Maxwell's equations and boundary conditions

In the study of electricity and magnetism a set of coupled partial differential equations, known as Maxwell's equations, are often used as the starting point to many theoretical analyses. These equations provide a basic mathematical model for a plethora of fields in physics, and optics is no exception. Problems involving light propagation in free-space and the interaction of light with matter can all be well-understood by using these equations.

We begin by restricting the analysis presented in this text to the macroscopic domain since we are dealing with the large-scale behavior of matter. This section will closely follow what is detailed in [85] in addition to a boundary condition analysis that concentrates on assumptions used when working with dielectric optical waveguides. Without further ado, Maxwell's equations in derivative form are:

$$\nabla \times \vec{\mathrm{E}} = -\frac{\partial \vec{\mathrm{B}}}{\partial \mathrm{t}} \tag{2.1}$$

$$\nabla \times \vec{H} = \frac{\partial \vec{D}}{\partial t} + \vec{J} \tag{2.2}$$

$$\nabla \cdot \vec{D} = \rho \tag{2.3}$$

$$\nabla \cdot \vec{B} = 0 \tag{2.4}$$

and

$$\nabla \cdot \vec{J} = -\frac{\partial \rho}{\partial t}, \tag{2.5}$$

where $\vec{E}$, $\vec{H}$, $\vec{D}$, $\vec{B}$, $\vec{J}$, and ρ are the electric field, magnetic field, electric flux field, magnetic flux field, current density, and volume charge density, respectively. These equations are not all independent since if the divergence of equation (2.1) is taken,

$$\nabla \cdot \frac{\partial \vec{B}}{\partial t} = 0$$

is obtained. This occurs because the divergence of the curl of any vector is zero.

Examining these equations individually, one can find that equation (2.1) is the differential form of Faraday's law of induction, equation (2.2) is a generalization of Ampere's circuital law (or the Biot-Savart law), equation (2.3) is the differential form of Gauss' law, equation (2.4) expresses that the lines of magnetic flux form a system of closed loops that do not terminate on a magnetic "charge," and equation (2.5) is the conservation of charge. Equations (2.1)-(2.5) may also be expressed in integral form which makes them much more convenient to apply to certain problems. Applying Stokes theorem to equations (2.1) and (2.2) yields:

$$\iint_S \nabla \times \vec{E} \cdot dS = \oint_C \vec{E} \cdot dl = -\frac{\partial}{\partial t} \iint_S \vec{B} \cdot dS \tag{2.6}$$

and

$$\oint_C \vec{H} \cdot dl = \iint_S \left(\frac{\partial \vec{D}}{\partial t} + \vec{J} \right) \cdot dS . \tag{2.7}$$

Then, by using the divergence theorem, equations (2.3)-(2.5) become:

$$\oiint_S \vec{D} \cdot dS = \iiint_V \rho dV \tag{2.8}$$

$$\oiint_S \vec{B} \cdot dS = 0 \tag{2.9}$$

and

$$\oiint_S \vec{J} \cdot dS = -\frac{\partial}{\partial t} \iiint_V \rho dV . \tag{2.10}$$

Now the relationship between $\vec{E}$, $\vec{H}$, $\vec{D}$, and $\vec{B}$ must be given. In free-space, there is a simple proportional relationship

$$\vec{B} = \mu_0 \vec{H}$$

and

$$\vec{D} = \epsilon_0 \vec{E},$$

where, $\mu_0 \approx 4\pi \cdot 10^{-7} \frac{H}{m}$ is the free-space permeability and $\epsilon_0 \approx \frac{1}{36\pi} \cdot 10^{-9} \frac{F}{m}$ is the free-space permittivity. In material bodies, these constants are replaced by rank 2 tensors (also known as dyadics). In practice, however, ϵ and μ reduce to scalar quantities (complex with negative imaginary parts if material has finite losses) that are independent of field strength. Sometimes, the concept of relative permittivity, ϵ_r, or permeability, μ_r, comes up in practice where $\epsilon_r = \epsilon/\epsilon_0$ and $\mu_r = \mu/\mu_0$. These are the ratios of ϵ and μ in a

specific material to that of free space. Knowing the relation between $\vec{E}$, $\vec{H}$, $\vec{D}$, and $\vec{B}$ means that the divergence equations (2.3) and (2.4) can also be expressed as

$$\nabla \cdot \vec{E} = \frac{\rho}{\epsilon}$$

and

$$\nabla \cdot \vec{H} = 0,$$

respectively.

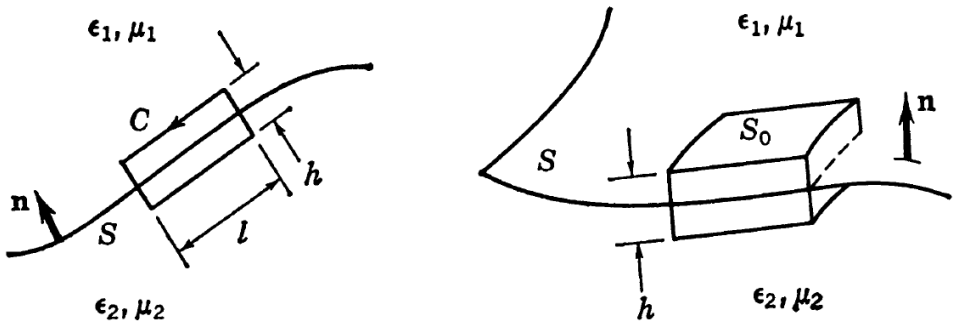

Figure 8: Contour C (left) and surface S_0 (right) used for deriving boundary conditions under different circumstances. Image obtained from [85].

A vector field is completely specified only when both the normal and tangential components are given and a necessary distinction between them must be mentioned. The normal component of a vector has no curl

$$\nabla \times \overrightarrow{A_\perp} \equiv 0$$

while the tangential component has no divergence,

$$\nabla \cdot \overrightarrow{A_\parallel} \equiv 0.$$

At a boundary, it is necessary to know the relationship between the field components on both sides, as shown in the two scenarios on Figure 8.

Beginning with the left side of Figure 8, a boundary surface S separates a material with ϵ_1 and μ_1 from another material with ϵ_2 and μ_2. The surface normal vector, $\hat{n}$, is assumed to be directed from medium 2 to medium 1, and a contour C is constructed parallel to the surface with an infinitesimally small side height h. According to equation (2.6), the line integral of the electric field around the C is equal to the partial derivative with respect to time of the magnetic flux through C. As the limit of h approaches zero, the total magnetic flux through C vanishes since it is a bounded function. This yields:

$$\lim_{h\to 0} \oint_C \vec{E} \cdot dl = (E_{1\parallel} - E_{2\parallel})l = 0,$$

where the above expression can be written as

$$E_{1\parallel} = E_{2\parallel}. \tag{2.11}$$

The subscript $\parallel$ signifies that the component of the electric field is tangential to the surface S and l is the length of the contour. Similarly, the line integral of the magnetic field around the same contour gives a similar result as long as the displacement field and current density are bounded functions. This means that:

$$H_{1\parallel} = H_{2\parallel}. \tag{2.12}$$

Equations (2.11) and (2.12) show that the tangential components of the electric and magnetic fields are continuous across a boundary where ϵ and μ are discontinuous. In contrast to how these equations were solved, the boundary conditions of the normal components will be solved according to what is shown on the right side of Figure 8. A small closed surface S_0 is constructed between the boundary between two media. Like before, $\hat{n}$ is assumed to be directed from medium 2 to medium 1. This setup consists of a "pillbox" with faces of equal area parallel to the surface S and an infinitesimal distance on either side.

Assuming there is no surface charge on S, applying equation (2.8) to the boundary yields:

$$\lim_{h\to 0} \oiint_S \vec{D} \cdot ds = (D_{1\perp} - D_{2\perp})S_0 = 0,$$

where the above expression can be summarized to

$$D_{1\perp} = D_{2\perp}. \tag{2.13}$$

Since equation (2.9) is of the same kind but with the magnetic flux density, it is easily found that

$$B_{1\perp} = B_{2\perp}. \tag{2.14}$$

The subscript $\perp$ signifies that the components of the electric and magnetic displacement field being evaluated are normal to the surface S. It can be seen that the normal components of the fields are also continuous across S. This is an idealization, however, because this assumes that the current density is bounded and that a surface charge density does not exist on the boundary S.

Because conducting boundaries will not be dealt with in this work, the current density will be neglected, but there are surface charges present in dielectrics. This means that equation (2.13) will slightly change when re-evaluating equation (2.8) with the presence of surface charges. This yields:

$$\hat{n} \cdot \left(\overrightarrow{D_{1\perp}} - \overrightarrow{D_{2\perp}}\right) = \rho_s, \tag{2.15}$$

which states that the normal component of the electric displacement field is discontinuous across a boundary, with the magnitude of the discontinuity being equal to the surface charge density ρ_s. Equation (2.15) can also be understood as the normal component of the electric field being discontinuous across dielectric media (because of the $\vec{D}$ and $\vec{E}$ relationship).

2.2 Modes in optical waveguides

From the equations shown in the previous section, an important parameter that often plays a significant role on describing how light propagates in mater is the refractive index, n. This dimensionless parameter comes up quite often when working with the equations shown in the previous section and is the ratio of the speed of in a vacuum, c_0, to the speed of light in a material, c,

$$n = \frac{c_0}{c} = \frac{\sqrt{\epsilon\mu}}{\sqrt{\epsilon_0\mu_0}} = \sqrt{\epsilon_r\mu_r}.$$

Interestingly, a phenomenon called total-internal reflection (TIR) occurs when light encounters a boundary going from a high-index medium, n_1, to a lower-index medium, n_0, at an angle with respect to a surface-normal line greater than the critical angle $\theta_c = \sin^{-1}\left(\frac{n_0}{n_1}\right)$, as seen in Figure 9. Waveguides are typically designed with this concept in mind. They are made with a central dielectric region, called "core," with index n_1 surrounded by a dielectric layer, called "cladding," with index n_0. For TIR to occur and confine light into the core, $n_1 > n_0$. Slab waveguides, like the one presented in Figure 10, are the simplest example of this.

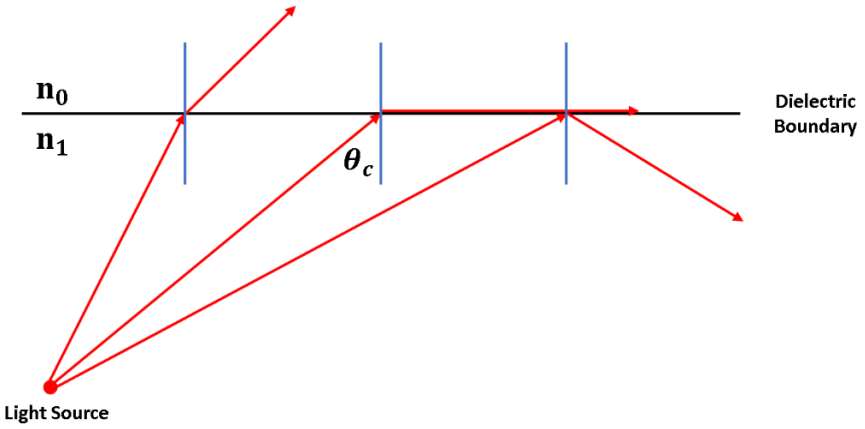

Figure 9: Demonstration of total internal reflection at a dielectric boundary occurring when the light-ray (red arrow) angle of incidence with respect to a surface-normal line (blue) is greater than θ_c. Note, this condition only occurs when the refractive index $n_1 > n_0$.

Guided modes are the result of how oscillating electromagnetic fields (also called plane-waves) within a waveguide constructively and destructively interfere with each other depending on their optical path length, which is determined by the core's size and angle of reflection at the core-cladding boundary. This generates a unique pattern of light that maintains its distribution at all locations along the waveguide axis and only occurs is if the condition of self-consistency is met [86]. This requires that as a plane-wave reflects twice from the core-cladding boundary, it reproduces itself. Meaning that only two distinct versions of the plane-wave are present and modes are discrete because not all plane-waves satisfy this condition.

In addition, compared to how light propagates in a homogenous medium, propagation within a waveguide can be thought of as the superposition of plane-waves that give rise to discrete propagation constants that depend on the boundary conditions imposed by the waveguide's geometry. This propagation constant, β, differs from k because

$$\beta = n_{eff}\frac{2\pi}{\lambda} \tag{2.16}$$

while

$$k = n\frac{2\pi}{\lambda}. \tag{2.17}$$

Which means that the refractive index experienced by the guided mode is different than that of light traveling through the bulk homogenous medium. In the next two subsections, it will be seen that n_{eff} lies between $n_0 \leq n_{eff} \leq n_1$ and can be obtained by solving the Helmholtz equation. With this process, the resulting pattern of light that corresponds to each discrete mode can also be found and will be shown in this work.

To give a more quantitative description of modes, a full vector solution of the fields will be obtained. Beginning with the assumption that light is traveling in a region without charges, equation (2.3) becomes

$$\nabla \cdot \vec{E} = 0$$

and there are no current densities present. Then, by curling both sides of equations (2.1) and (2.2) yields:

$$\left(\nabla^2 - \epsilon\mu\frac{\partial^2}{\partial t^2}\right)\vec{E} = 0, \tag{2.18}$$

for the electric field and

$$\left(\nabla^2 - \epsilon\mu\frac{\partial^2}{\partial t^2}\right)\vec{H} = 0 \tag{2.19}$$

for the magnetic field. Oscillatory solutions satisfy both of these equations, so a simple complex exponential ansatz will be used to proceed with the analysis in cartesian coordinates for slab waveguides and cylindrical coordinates for fibers.

2.2.1 The dielectric slab waveguide

The complex exponential representation of the electric and magnetic modes that propagate through a slab waveguide is

$$\vec{E} = \vec{E}(x, y)e^{j(\beta z - \omega t)} \tag{2.20}$$

and

$$\vec{H} = \vec{H}(x, y)e^{j(\beta z - \omega t)}, \tag{2.21}$$

respectively, with $\vec{E}(x, y)$ and $\vec{H}(x, y)$ being the characteristic pattern of light that corresponds to the mode and ω being the angular frequency. It is known that only the transverse electric (TE) and transverse magnetic (TM) modes are allowed to propagate in slab waveguides [87]. As the name implies, for TE modes there is no component of the electric field pointing in the direction of propagation ($E_x = E_z = H_y = 0$). Similarly, there is no component of the magnetic field pointing in the direction of propagation ($H_x = H_z = E_y = 0$) for TM modes. Both of these mode types are analogous to each other except for the components of the fields that exist for each and some discontinuities at the core-cladding boundary. For this reason, only TE modes will be solved for in the analysis of slab waveguides presented in this work.

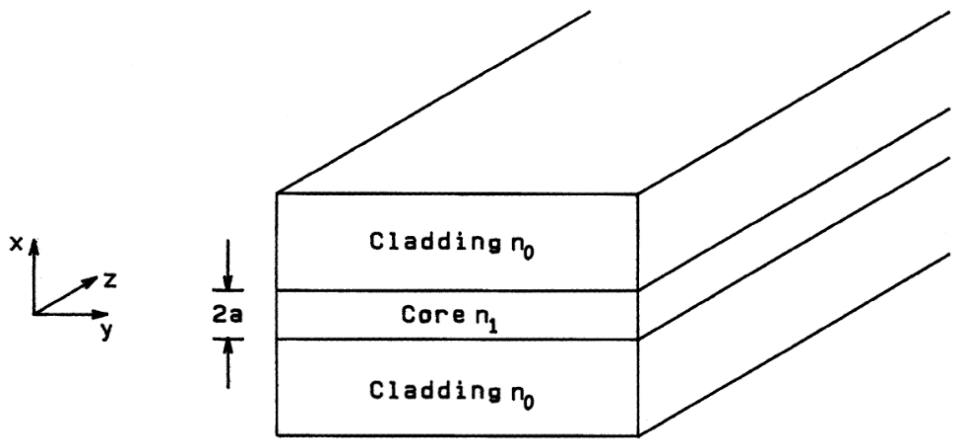

Figure 10: Representation of a slab waveguide. The central region of diameter $2a$ *is the high-refractive index (*n_1*) core and the regions that surround it are the lower-index (*n_0*) cladding. Image obtained from [88].*

Closely following the steps shown in [87], we will find solutions for the y-component of the modal profile $\vec{E}(x, y)$ and its respective n_{eff} for a slab waveguide with a core of width of $2a$. As seen in Figure 10, the waveguide is infinite in the y direction and light is propagating in the z direction which means that $\frac{\partial}{\partial y} = 0$ and $\frac{\partial}{\partial z} = j\beta$, respectively. For TE modes only the E_y component exists for the electric field, therefore by plugging equation (2.20) into equation (2.18), one obtains

$$\left(\frac{d^2}{dx^2} + (\omega^2\mu\epsilon - \beta^2)\right)E_y = 0, \tag{2.22}$$

where $\omega^2\epsilon\mu = \frac{\omega^2}{c^2} = k^2$ (note that k depends on the refractive index of the region being analyzed, as shown in equation (2.17)).

By inspection, it is evident that two solutions can be obtained from equation (2.22) depending on the region it is solved for. Solutions outside of the core are to be exponential while solutions within the core must be oscillatory. The two solutions obtainable in the core can be even (symmetric) or odd (anti-

symmetric), with the even fundamental mode always being the lowest in order followed by the first odd higher-order mode and so on alternating between even and odd. Since equation (2.22) is a second-order differential equation, solving it is a straightforward task. Its characteristic equation yields

$$k_x = \sqrt{k_1^2 - \beta^2} \tag{2.23}$$

for the core bounded by $-a \leq x \leq a$ and

$$\alpha = \sqrt{\beta^2 - k_0^2} \tag{2.24}$$

for the cladding in the regions $x > |a|$. Equation (2.23) is imaginary which means that the solutions in the core will be oscillatory and (2.24) is real which means that solutions in the cladding will be exponential as expected.

Therefore, the even solution for the modal profile is

$$E_y(x) = \begin{cases} C_0 e^{\alpha(x+a)}, & x < -a \\ C_1 \cos(k_x x), & -a \leq x \leq a \\ C_0 e^{-\alpha(x-a)}, & x > a \end{cases} \tag{2.25}$$

while the odd solution is

$$E_y(x) = \begin{cases} C_0 e^{\alpha(x+a)}, & x < -a \\ C_1 \sin(k_x x), & -a \leq x \leq a. \\ C_0 e^{-\alpha(x-a)}, & x > a \end{cases} \tag{2.26}$$

In the above equations, C_1 is the amplitude of the electric field in the core with units of V/m. On the other hand, C_0 depends on the amplitude of the oscillatory solution (of the core) at the boundary to ensure continuity. For the even mode $C_0 = C_1 \cos\big(k_x(-a)\big) = C_1 \cos\big(k_x(a)\big)$ on both sides of the boundary and for the odd mode $C_0 = C_1 \sin\big(k_x(-a)\big)$ for when $x = -a$ and $C_0 = C_1 \sin\big(k_x(a)\big)$ for when $x = a$.

In the boundary conditions section, it was shown that the tangential component of the electric and magnetic fields (in the absence of current densities) are continuous across a boundary. Using the equation for the tangential component of the magnetic field, $H_z = \left(\frac{1}{j\omega\mu}\right)\left(\frac{\partial E_y}{\partial x}\right)$, the boundary conditions for E_y and H_z at $x = -a$ and $x = a$ can be matched. Due to symmetry, the equations can be matched for either side. Therefore by using $x = a$ the process goes as follows:

$$\frac{E_{y,clad}}{H_{z,clad}} = \frac{E_{y,core}}{H_{z,core}},$$

substituting in the variables gives

$$\frac{C_0}{\frac{\alpha}{\mu_{0,clad}}C_0} = \frac{C_1\cos(k_x a)}{C_1\frac{k_x}{\mu_1}\sin(k_x a)},$$

which is

$$\alpha = \frac{\mu_{0,clad}}{\mu_1}k_x\tan(k_x a) \tag{2.27}$$

for the even mode. Repeating this process for the odd mode gives:

$$\alpha = -\frac{\mu_{0,clad}}{\mu_1}k_x\cot(k_x a). \tag{2.28}$$

For this example, $\mu_{0,clad}$ is the relative permeability of the cladding $\mu_{r,cladding} = \mu_{0,clad}$. This should not be confused with the free-space permeability, μ_0. At optical and near optical frequencies $\mu_1 = \mu_{0,clad} = 1$. Interestingly, if the exponential decay α for equations (2.27) and (2.28) outside of the core is infinitely large, E_y will tend to zero at the boundary and will follow the same rules as perfectly conducting metallic waveguides where the tangential component of the electric field vanishes at the boundary.

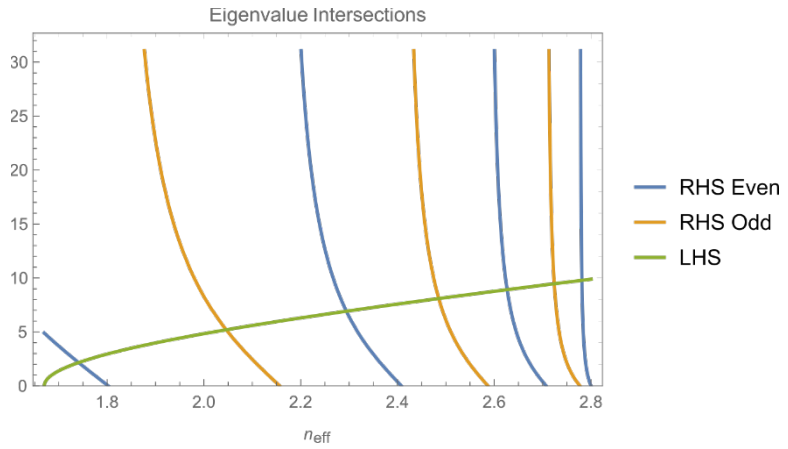

Figure 11: Graphical method for solving for n_{eff} by plotting the right-hand side (RHS) of equations (2.29) and (2.30) with the common left-hand side (LHS). The horizontal axis value of the intersection, increasing in order from left to right, corresponds to the mode's effective index n_{eff}. The waveguide was assumed to have $n_1 = 2.8$, $n_0 = 1.67$, $2a = 7\mu m$, and $\lambda = 5\mu m$.

The effective index can only be found graphically, as seen in Figure 11. Therefore, equations (2.27) and (2.28) are related by multiplying both sides by a:

$$\alpha(a) = \frac{\mu_{0,clad}}{\mu_1}(k_x a)\tan(k_x a) \tag{2.29}$$

and

$$\alpha(a) = -\frac{\mu_{0,clad}}{\mu_1}(k_x a)\cot(k_x(a)). \tag{2.30}$$

Equations (2.29) and (2.30) have equal left-hand sides and it is known that k_x and α are functions of n_{eff}. Therefore, their right- and left-hand sides can be plotted together with n_{eff} as the independent variable. The intersections of the resulting plot are the discrete eigenvalues of n_{eff} unique to a specific waveguide. For example, say we want to find the effective index and plot the mode profile of a chalcogenide glass-polymer waveguide. In the $3-5\mu m$ wavelength range, these have indices of ~ 2.8 and ~ 1.67, respectively. The

desired core diameter is 7μm and the wavelength that we will solve the modes for will be 5μm. As explained above, by looking at the intersections of the right-hand side of equations (2.29) and (2.30) with the left-hand side, the effective index can be found. Using equations (2.25) and (2.26) with the assumption that $C_1 = 1\frac{V}{m}$, the largest effective index corresponds to the fundamental mode and the next effective index is used to plot the first higher-order mode. These two mode profiles are the ones shown in Figure 12.

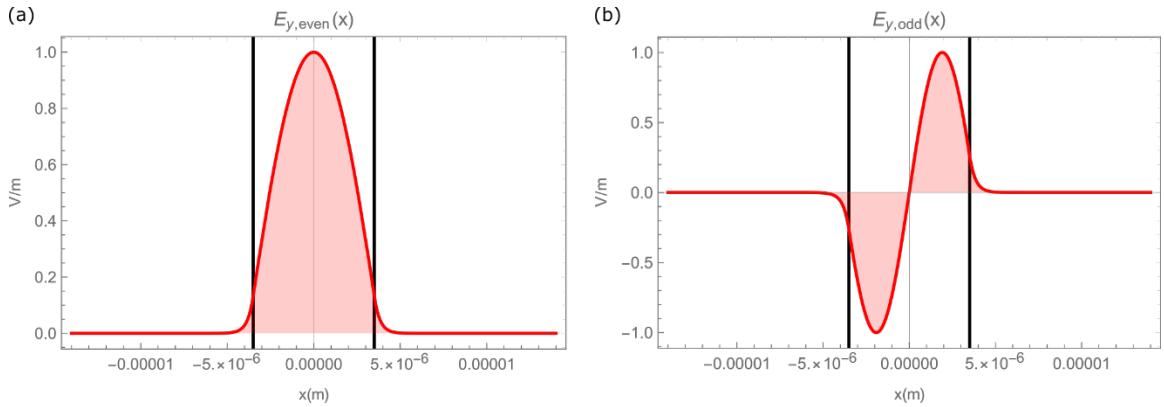

Figure 12: Fundamental mode (a) and first higher-order mode (b) of a $2a = 7\mu m$ *waveguide with core index of* 2.8 *and cladding index of* 1.67 *and with a* $\lambda = 5\mu m$ *wavelength being guided. Effective indices of this waveguide were graphically determined from Figure 11,* $n_{eff} = 2.7811645867351555$ *for the fundamental mode and* $n_{eff} = 2.7240311500168923$ *for the first higher-order mode.*

2.2.2 The optical fiber

In comparison to slab waveguides, fibers support transverse and hybrid modes. Hybrid modes result from having both electric and magnetic components pointing in the direction of propagation, which makes analyzing modes in optical fibers a more tedious process. However, the methods and rules used in the previous analysis still apply. This subsection will be based on solutions presented by [89] and derivations detailed in [88], [90]. Additionally, the weakly-guiding approximation will be avoided in this subsection, unlike in other texts, because the relative index contrast between the core and cladding of the fibers used for IR CFBs is much larger than unity.

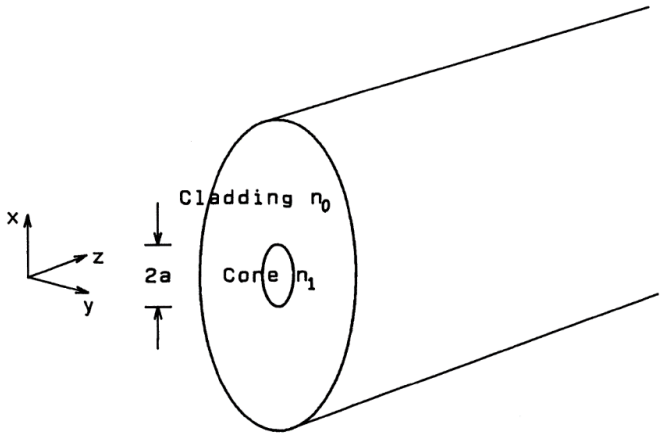

Figure 13: Step index optical fiber uniform in the z-direction, with a core of refractive of n_1, a cladding index of n_0, and diameter $2a$. Image from [88].

Another version of the complex exponential form of the fields that satisfy equations (2.18) and (2.19) must be used to accommodate for the cylindrical coordinate system (r, θ, z) used for finding modes in axially symmetric fibers like the one shown in Figure 13.

$$\vec{E} = \vec{E}(r, \theta, z)e^{-j(\beta z - \omega t)} \tag{2.31}$$

is used for the electric field and

$$\vec{H} = \vec{H}(r, \theta, z)e^{-j(\beta z - \omega t)} \tag{2.32}$$

for the magnetic field. Equations (2.31) and (2.32) are plugged into Maxwell's equations beginning with the assumption used for slab waveguides in the previous section where light is traveling in a region without charges. Equation (2.3) equals zero and there are no current densities present. When computing the curl of equations (2.1) and (2.2), knowing that the divergence of the flux fields is zero, and after tedious algebraic manipulation the following equations are obtained:

$$\left(\frac{\partial^2}{\partial r^2} + \frac{1}{r}\frac{\partial}{\partial r} + \frac{1}{r^2}\frac{\partial^2}{\partial \theta^2} + (\omega^2 \mu \epsilon - \beta^2)\right) E_z = 0 \tag{2.33}$$

and

$$\left(\frac{\partial^2}{\partial r^2}+\frac{1}{r}\frac{\partial}{\partial r}+\frac{1}{r^2}\frac{\partial^2}{\partial \theta^2}+(\omega^2\mu\epsilon-\beta^2)\right)H_z=0. \tag{2.34}$$

The components that correspond to the r and θ directions can be found in [88]–[90] and complete mode solutions for the electric field vector will be listed at the end of this subsection. Equation (2.33) is best solved using separation of variables. This process consists of using a product solution E_z or $H_z = R_z(r)\Theta_z(\theta)$ that is plugged in either equation (2.33) or (2.34) to produce two differential equations that are easy to solve. Doing so gives

$$\frac{\partial^2\Theta_z}{\partial\theta^2}+n^2\Theta_z=0$$

and

$$\frac{\partial^2 R_z}{\partial r^2}+\frac{1}{r}\frac{\partial R_z}{\partial r}+\left(\omega^2\mu\epsilon-\beta^2-\frac{n^2}{r^2}\right)R_z=0,$$

which produce:

$$\Theta_z(\theta)=\begin{cases}\cos(n\theta+\phi)\\ \sin(n\theta+\phi)\end{cases} \tag{2.35}$$

and

$$R_z(r)=\begin{cases}AJ_n\left(\frac{k_{x,1}r}{a}\right)+A'N_n\left(\frac{k_{x,1}r}{a}\right), & r\le a\\ BK_n\left(\frac{k_{x,0}r}{a}\right)+B'I_n\left(\frac{k_{x,0}r}{a}\right), & r>a\end{cases}, \tag{2.36}$$

where a is the radius of the fiber, n is an integer, ϕ is an arbitrary constant phase, J_n and N_n, respectively, are Bessel functions of the first and second kind of order n, and K_n and I_n, respectively, are modified Bessel

functions of the first and second kind of order n. The term $k_{x,l}$ is the transverse propagation constant of the core ($l = 1$) or cladding ($l = 0$). As it is customary to do, in the core it is expressed as u,

$$u^2 = k_{x,1}^2 = k_1^2 a^2 \left(n_1^2 - n_{eff}^2\right) \tag{2.37}$$

and in the cladding as w,

$$w^2 = k_{x,0}^2 = k_0^2 a^2 \left(n_{eff}^2 - n_0^2\right), \tag{2.38}$$

where the relations between the wavenumber k_0, the angular frequency ω, the inverse speed of light squared $\frac{1}{c^2} = \epsilon\mu$, the refractive index $n^2 = \epsilon_r \mu_r$, and effective mode index n_{eff} were briefly presented in the previous subsection. Adding equations (2.37) and (2.38) together gives:

$$u^2 + w^2 = V^2,$$

where

$$V = k_0 a \sqrt{n_1^2 - n_0^2}. \tag{2.39}$$

Equation (2.39), also called the normalized frequency or V-number, is of extreme importance. From it, one can find the total number of modes that a fiber supports by using $V^2/2$. The right-hand side of equation (2.39),

$$NA = \sqrt{n_1^2 - n_0^2} = \sin(\alpha), \tag{2.40}$$

is the numerical aperture (NA). Taking the inverse sine of the NA yields the light-acceptance half-angle, α, which states the steepest angle light can be incident onto the entrance of the core with respect to a line normal to the surface (similar to the normal-surface line concept of Figure 9 but at the entrance of the fiber's core). By examining the NA equation, one can see that the higher the index contrast between the core and

the cladding, the greater the angle of acceptance. Therefore, to design IR fibers for an imaging bundle, a higher the NA means that the fibers will be better at collecting light.

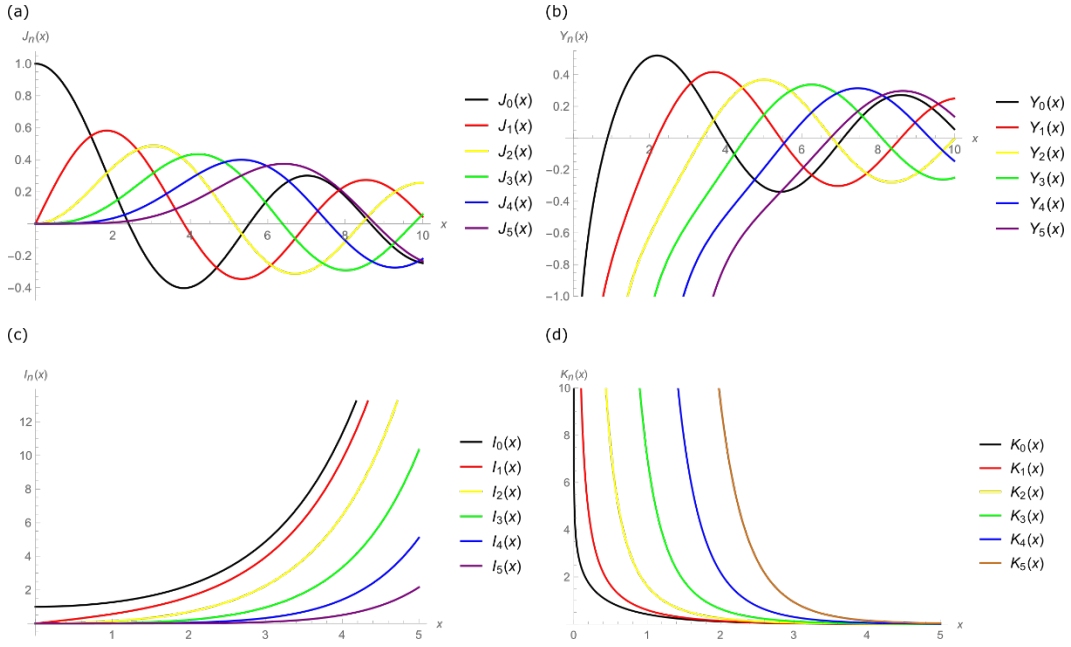

Figure 14: Bessel function of the first kind $J_n(x)$ (a), Bessel function of the second kind $N_n(x)$ (b), modified Bessel function of the first kind $I_n(x)$ (c), and modified Bessel function of the second kind $K_n(x)$ (d).

Resuming the derivation of fiber modes, since Bessel functions of the second kind diverge at $r = 0$ and modified Bessel functions of the second kind diverge at $r = \infty$ as seen in Figure 14, the coefficients B and D of those functions have to be zero. Therefore, equation (2.36) reduces to

$$R(r) = \begin{cases} AJ_n\left(\frac{ur}{a}\right) & \text{for } r \leq a \\ BK_n\left(\frac{wr}{a}\right) & \text{for } r > a \end{cases}. \tag{2.41}$$

Multiplying equation (2.35) with (2.41) yields the product solution:

$$E_z(r \leq a) = AJ_n\left(\frac{ur}{a}\right)\cos(n\theta + \phi) \tag{2.42}$$

and

$$H_z(r \le a) = AJ_n\left(\frac{ur}{a}\right)\sin(n\theta + \phi) \tag{2.43}$$

for the z-component of the electric and magnetic field in the core, in addition to

$$E_z(r > a) = Bk_n\left(\frac{wr}{a}\right)\cos(n\theta + \phi) \tag{2.44}$$

and

$$H_z(r > a) = Bk_n\left(\frac{wr}{a}\right)\sin(n\theta + \phi) \tag{2.45}$$

for the z-component of the electric and magnetic field in the cladding with the constant $B = A\frac{J_n(u)}{K_n(w)}$. The continuity condition at the boundary $r = a$ requires that the E_θ and H_θ be continuous across the boundary. Therefore, the following angular component solutions from [88] were obtained:

$$E_\theta(r \le a) = -\frac{ja^2}{u^2}\left[-A\beta\frac{n}{r}J_n\left(\frac{ur}{a}\right) - C\omega\mu_0\frac{u}{a}J_n'\left(\frac{ur}{a}\right)\right]\sin(n\theta + \phi), \tag{2.46}$$

$$H_\theta(r \le a) = -\frac{ja^2}{u^2}\left[A\omega\epsilon_0 n_1^2\frac{u}{a}J_n'\left(\frac{ur}{a}\right) + C\beta\frac{n}{r}J_n\left(\frac{ur}{a}\right)\right]\cos(n\theta + \phi), \tag{2.47}$$

for the core and

$$E_\theta(r > a) = \frac{ja^2}{w^2}\left[-A\beta\frac{n}{r}K_n\left(\frac{wr}{a}\right) - C\omega\mu_0\frac{w}{a}K_n'\left(\frac{wr}{a}\right)\right]\frac{J_n(u)}{K_n(w)}\sin(n\theta + \phi), \tag{2.48}$$

$$H_\theta(r > a) = \frac{ja^2}{w^2}\left[A\omega\epsilon_0 n_0^2\frac{w}{a}K_n'\left(\frac{wr}{a}\right) + C\beta\frac{n}{r}K_n\left(\frac{wr}{a}\right)\right]\frac{J_n(u)}{K_n(w)}\cos(n\theta + \phi), \tag{2.49}$$

for the cladding. Note that n with a subscript is the refractive index of the region where the solution is specified. By using equation (2.46) and (2.48) evaluated at $r = a$ to satisfy the continuity relation gives

$$nA\beta\left(\frac{1}{u^2}+\frac{1}{w^2}\right)=-C\omega\mu_0\left[\frac{J_n'(u)}{uJ_n(u)}+\frac{K_n'(w)}{wK_n(w)}\right], \tag{2.50}$$

and by using equations (2.47) and (2.49) at $r=a$ too gives

$$A\omega\epsilon_0\left[n_1^2\frac{J_n'(u)}{uJ_n(u)}+n_0^2\frac{K_n'(w)}{wK_n(w)}\right]=-nC\beta\left(\frac{1}{u^2}+\frac{1}{w^2}\right). \tag{2.51}$$

Using equation (2.50), the constant C used in equations (2.46)-(2.49) can be found. From equations (2.50) and (2.51), the dispersion relation

$$\left[\frac{J_n'(u)}{uJ_n(u)}+\frac{K_n'(w)}{wK_n(w)}\right]\left[n_1^2\frac{J_n'(u)}{uJ_n(u)}+n_0^2\frac{K_n'(w)}{wK_n(w)}\right]=\frac{\beta^2}{k^2}\left(\frac{1}{u^2}+\frac{1}{w^2}\right)^2 n^2 \tag{2.52}$$

is obtained. Simplifying further by combining it with

$$\frac{\beta^2}{k^2}\left(\frac{1}{u^2}+\frac{1}{w^2}\right)=\frac{n_1^2}{u^2}+\frac{n_0^2}{w^2}, \tag{2.53}$$

obtained from equations (2.37) and (2.38) yields:

$$\left[\frac{J_n'(u)}{uJ_n(u)}+\frac{K_n'(w)}{wK_n(w)}\right]\left[\frac{J_n'(u)}{uJ_n(u)}+\left(\frac{n_0}{n_1}\right)^2\frac{K_n'(w)}{wK_n(w)}\right]=n^2\left(\frac{1}{u^2}+\frac{1}{w^2}\right)\left[\frac{1}{u^2}+\left(\frac{n_0}{n_1}\right)^2\frac{1}{w^2}\right]. \tag{2.54}$$

Equation (2.54) is the characteristic equation for modes in a step-index fiber. Both sides are functions of on n_{eff}. This eigenvalue is discrete and lies between $n_0 \le n_{eff} \le n_1$, as in the case of slab waveguides. Therefore, solutions can be found by using a similar plotting method to the one used in the previous subsection. This is shown in Figure 15, but with u as the independent variable. When $n=0$, effective indices correspond to TE and TM modes. On the other hand, hybrid modes occur when $n \ge 1$ but the situation becomes more complex and numerical methods are needed to solve equation (2.54) exactly. Also, the primes on the Bessel functions signify differentiation with respect to the variable inside; u and w in this case. The derivative of the Bessel function of the first kind is given by

$$\frac{dJ_\nu(\zeta)}{d\zeta} = \frac{1}{2}[J_{n-1}(\zeta) - J_{n+1}(\zeta)]$$

and for the modified Bessel function of the second kind its

$$\frac{dK_\nu(\zeta)}{d\zeta} = -\frac{1}{2}[K_{n-1}(\zeta) + K_{n+1}(\zeta)].$$

Note, the decision to use u stems from the fact that n_{eff} may be found when u is known in addition to being able to use the V-number as a method of determining the order, n, of the Bessel functions that correspond to each mode. For example, the cutoffs of transverse modes are determined by the zeros of the 0^{th} -order Bessel function of the first kind while the cutoffs for some hybrid modes are determined by the zeros of the 1^{st} -order Bessel function of the first kind. All other mode cutoffs are beyond the scope of this work but the reader may refer to [89] to learn more about this.

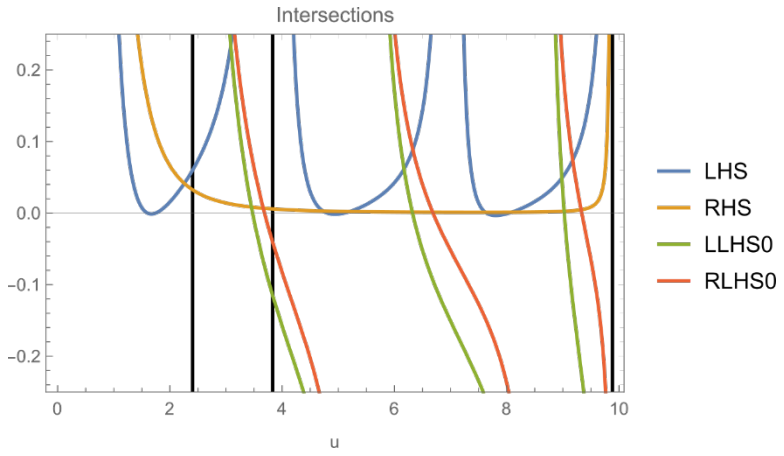

Figure 15: Graphical method for finding n_{eff} for a fiber with $n_1 = 2.8$, $n_0 = 1.67$, $a = 3.5\mu m$, and $\lambda = 5\mu m$. Left- and right-hand sides of the hybrid mode characteristic equation (2.54) plotted for $n = 0$ and $n = 1$ with u (which is a function of n_{eff}) as the independent variable. LHS is the left-hand side and RHS is the right-hand side of the characteristic equation. For TE and TM modes $RHS = 0$ because $n = 0$, therefore the left-hand side of the left yields (LLHS0) the TE mode eigenvalues and the right-hand side of the left side (RLHS0) yields the TM modes. Since the V-number is related to u, it can be used to illustrate some mode cutoff conditions (shown as black bars).

The remaining part after finding the effective index is being able to plot the modes to visualize them. Unlike in the previous subsection, modal field-pattern solutions in this subsection were given where it was most convenient to eventually arrive at the characteristic equation. For completeness, the individual components that make up the full-vector mode (2.31) are:

$$E_z = AJ_n\left(\frac{ur}{a}\right)\cos(n\theta + \phi), \tag{2.55}$$

$$E_\theta = jA\beta\frac{a}{u}\left[\frac{(1-s)}{2}J_{n-1}\left(\frac{ur}{a}\right) + \frac{(1+s)}{2}J_{n+1}\left(\frac{ur}{a}\right)\right]\sin(n\theta + \phi), \tag{2.56}$$

and

$$E_r = -jA\beta\frac{a}{u}\left[\frac{(1-s)}{2}J_{n-1}\left(\frac{ur}{a}\right) - \frac{(1+s)}{2}J_{n+1}\left(\frac{ur}{a}\right)\right]\cos(n\theta + \phi) \tag{2.57}$$

for the core at $r \leq a$, and

$$E_z = A\frac{J_n(u)}{K_n(w)}K_n\left(\frac{wr}{a}\right)\cos(n\theta + \phi), \tag{2.58}$$

$$E_\theta = jA\beta\frac{aJ_n(u)}{wK_n(w)}\left[\frac{(1-s)}{2}K_{n-1}\left(\frac{wr}{a}\right) - \frac{(1+s)}{2}K_{n+1}\left(\frac{wr}{a}\right)\right]\sin(n\theta + \phi), \tag{2.59}$$

$$E_r = -jA\beta\frac{aJ_n(u)}{wK_n(w)}\left[\frac{(1-s)}{2}K_{n-1}\left(\frac{wr}{a}\right) + \frac{(1+s)}{2}K_{n+1}\left(\frac{wr}{a}\right)\right]\cos(n\theta + \phi) \tag{2.60}$$

for the cladding at $r > a$. In equations (2.55)-(2.60),

$$s = \frac{n\left(\frac{1}{u^2} + \frac{1}{w^2}\right)}{\left[\frac{J_n'(u)}{uJ_n(u)} + \frac{K_n'(w)}{wK_n(w)}\right]}.$$

Using the above modal equations and concentrating mostly on the core since the cladding is just exponentially decreasing, four mode profiles are presented in Figure 16: the two degenerate states of the fundamental mode, TE, and TM modes.

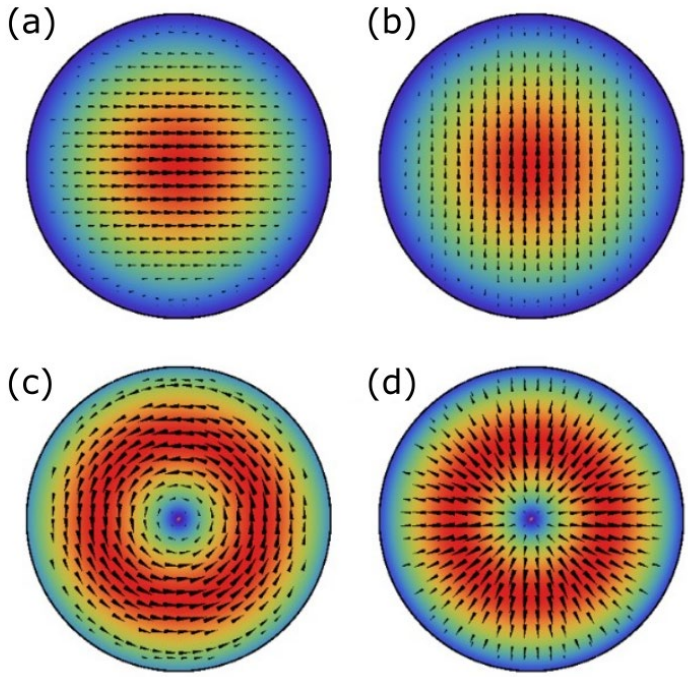

Figure 16: Intensity profiles for the full-vector degenerate fundamental hybrid modes polarized in the x (a) and y direction (b), TE mode (c), and TM mode (d). With the parameters given in Figure 15, $n_{eff} =$ 2.7525865829904914 for the fundamental modes, $n_{eff} = 2.687710283694779$ for the TE mode, and $n_{eff} =$ 2.6732787595634804 for the TM mode. The arrows represent the direction of the electric field.

2.3 Mode coupling and analysis of crosstalk

So far, we have touched on the modal properties of two different kinds of waveguides, the slab and the cylindrical fiber. Although different geometrically, the rules and equations that govern how light is guided in them are the same. Typically, when performing the analyses shown in the previous section, it is assumed that the waveguides are in complete isolation, which means that there are no other high-index

regions nearby where light can be guided. In CFBs however, there may be hundreds, if not, thousands of other cores in close proximity.

We showed in the previous section that light is not entirely confined within the core, what exists in the cladding region (coming from the core) is a fraction of the light that exponentially decreases rapidly. Let us suppose we have two cores near each other and they share the same common cladding as in Figure 17. If light were to be launched into the left core, the exponentially decreasing part of the mode confined within that core will excite a mode in the adjacent core. Due to conservation of energy, that new excited mode will take the power from the original waveguide until its exponentially decreasing field excites the original waveguide again and the process repeats itself over and over, with this power oscillating from core to core in a sinusoidal fashion along the direction of propagation. This "leaking" or "beating" of light as it travels along the waveguide is known as mode-coupling, or as we call it for imaging bundles: crosstalk.

Different methods exist to describe this phenomenon, but one of the most widely used is the perturbation analysis method called coupled-mode theory (CMT) [83], [87], [88], [91], [92]. Although this method gives a good explanation of what occurs in a system where more than one core or waveguide is nearby, it is an approximation and its applicability has been a topic of much debate [83], [93]–[96]. Something to keep in mind when using CMT is that, as mentioned before, modes for individual cores are solved for as if they were in isolation and coupling integrals are solved to find out how coupled they actually are. There are three versions of this method: orthogonal, non-orthogonal, and vectorial [83], [92], [97]. Another more rigorous method, which we will briefly touch on in this section, is what we call "supermode theory." This method considers the whole system as a composite waveguide, taking into account all boundary conditions that yield modal solutions to Maxwell's equations (called supermodes) for the overall structure [88], [91], [98]. Note, another name given to these modes are (vector) normal modes [91], [99]. Similar to [84], we will use CMT despite its limitations because it has its advantages. Assumptions used will be clearly stated and the limits to its applicability for imaging bundles will be discussed once more,

this time looking at a fiber bundle made of high-index chalcogenide glass cores placed in a low-index polymer common cladding. Also this section we will be mostly concentrating on the orthogonal-CMT to understand how coupling between waveguides works and how it can be inhibited.

2.3.1 Coupled-mode theory

The derivations in this subsection follow what is detailed in [88], and we will use the assumptions used in orthogonal-CMT. All information provided in this subsection and onwards will be presented in a more summarized manner to follow through and not get too deep in the math. Afterwards, an example scenario will be analyzed with CMT to understand the coupling between a pair of slab waveguides which are analogous to optical fibers. For optical fibers, the analysis will be presented in appendix 1, where results obtained with the CMT are compared with the FEM for different core separations and as the refractive index contrast between the core and cladding is increased beyond what is typically thought of a strongly-guiding conditions.

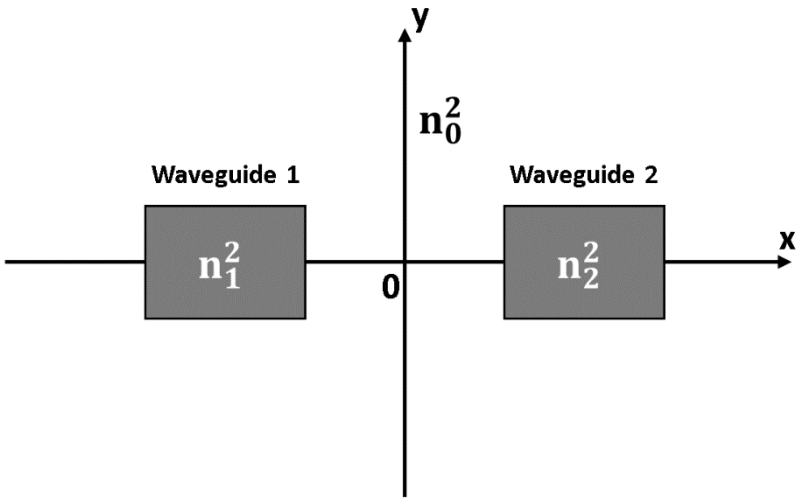

Figure 17: Coupled-waveguide system used to explain and derive the coupled-mode equations. In CMT, the modes for both waveguides are solved for independently and then solutions are substituted in the coupling coefficients (c_{pq}, χ_p, and κ_{pq}) to see how coupled the waveguides are.

Proceeding with the brief derivation and analysis of CMT, we consider the simple case of the two identical (or almost identical) waveguides in close proximity to each other, as seen in Figure 17. These waveguides are to be treated as if they were in isolation, where their $\overrightarrow{E_p}$ and $\overrightarrow{H_p}$ modes satisfy Maxwell's equations and $p = 1, 2$ represents the left and right waveguides, respectively. It is assumed that the electromagnetic fields of the coupled waveguide structure can be expressed as a linear combination of modes in each waveguide:

$$\vec{E} = A(z)\overrightarrow{E_1} + B(z)\overrightarrow{E_2}, \tag{2.61}$$

and

$$\vec{H} = A(z)\overrightarrow{H_1} + B(z)\overrightarrow{H_2}. \tag{2.62}$$

Then, equations (2.61) and (2.62) are plugged into equations (2.1),

$$\nabla \times \vec{E} = -j\omega\mu_0\vec{H},$$

and (2.2),

$$\nabla \times \vec{H} = j\omega\epsilon_0 N^2\vec{E},$$

to compute their curls with N^2 being the refractive index distribution of the coupled-waveguide system and the time rate of change $\frac{\partial}{\partial t} = j\omega$. This process yields a set of relations [88] that eventually leads to the following set of coupled differential equations:

$$\frac{dA}{dz} + c_{12}\frac{dB}{dz}e^{-j2\delta z} + j\chi_1 A + j\kappa_{12}Be^{-j2\delta z} = 0 \tag{2.63}$$

and

$$\frac{dB}{dz} + c_{21}\frac{dA}{dz}e^{j2\delta z} + j\chi_2 B + j\kappa_{21}Ae^{j2\delta z} = 0. \tag{2.64}$$

Also, note that $\overrightarrow{E_p}$ and $\overrightarrow{H_p}$ in equations (2.61) and (2.62) are the complete modal expressions of the form

$$\overrightarrow{E_p} = \overrightarrow{E_p}(x, y, z)e^{-j\beta_p z}$$

and

$$\overrightarrow{H_p} = \overrightarrow{H_p}(x, y, z)e^{-j\beta_p z}.$$

From equations (2.63) and (2.64), the following coefficients are of great importance to CMT:

$$C_{pq} = \frac{\int_{A_\infty} \left(\overrightarrow{E_p}^* \times \overrightarrow{H_q} + \overrightarrow{E_q} \times \overrightarrow{H_p}^*\right) \cdot \hat{n_z} dA}{\int_{A_\infty} \left(\overrightarrow{E_p}^* \times \overrightarrow{H_p} + \overrightarrow{E_p} \times \overrightarrow{H_p}^*\right) \cdot \hat{n_z} dA}, \tag{2.65}$$

$$\chi_p = \frac{\omega\epsilon_0(n_q - n_0) \int_{A_{co,q}} \overrightarrow{E_p}^* \cdot \overrightarrow{E_p} dA}{\int_{A_\infty} \left(\overrightarrow{E_p}^* \times \overrightarrow{H_p} + \overrightarrow{E_p} \times \overrightarrow{H_p}^*\right) \cdot \hat{n_z} dA}, \tag{2.66}$$

and

$$\kappa_{pq} = \frac{\omega\epsilon_0(n_p - n_0) \int_{A_{co,p}} \overrightarrow{E_p}^* \cdot \overrightarrow{E_q} dA}{\int_{A_\infty} \left(\overrightarrow{E_p}^* \times \overrightarrow{H_p} + \overrightarrow{E_p} \times \overrightarrow{H_p}^*\right) \cdot \hat{n_z} dA}, \tag{2.67}$$

where $p, q = 1, 2$ (or $2, 1$), n_0 is the cladding index, A_∞ is the coupled-waveguide system's entire area, and $A_{co,p}$ (or $A_{co,q}$) is the area of core p (or q). The first coefficient, c_{pq} is the butt-coupling coefficient and for all of our analyses it will be neglected. As the name implies, butt-coupling occurs when waveguides are longitudinally offset from each other and the output of one is coupled to the input of another, which does not occur in the fiber bundles being analyzed in this work. The next term is the self-coupling coefficient, χ_p. This term describes how well light is confined within the core of a waveguide by looking at how much leaks into the adjacent; the area integral is taken for core q while the field inner product and power terms are from waveguide p's mode. Finally, the coupling coefficient, κ_{pq} (arguably the most important of the

three) describes how coupled the waveguides are. This term looks at the overlap between the mode of waveguide p and the mode of waveguide q inside of waveguide p.

Conventionally $c_{pq} = \chi_p = 0$, so we will neglect them in the analyses presented here. Note, χ_p does matter depending on how well confined light within a core is and how close together the waveguides are but in our analyses this factor was ~0. Therefore, equations (2.63) and (2.64) become:

$$\frac{dA}{dz} + j\kappa B e^{-j2\delta z} = 0, \tag{2.68}$$

and

$$\frac{dB}{dz} + j\kappa A e^{j2\delta z} = 0, \tag{2.69}$$

keeping in mind the reciprocity relation of the coupling coefficients $\kappa = \kappa_{12} = \kappa_{21}$ (assuming that κ_{pq} is real). The δ seen in the equations above is the difference in propagation constants, defined as:

$$\delta = \frac{\beta_2 - \beta_1}{2}. \tag{2.70}$$

Before we present the solutions for equations (2.68) and (2.69), we must first discuss the power carried by each mode. In waveguide p ($p = 1, 2$), the power carried by the mode is given by:

$$P_p = \int_{A_\infty} \left(\overrightarrow{E_p^*} \times \overrightarrow{H_p}\right) \cdot \hat{n_z} dA. \tag{2.71}$$

The denominators of equations (2.65)-(2.67) are, therefore, normalized to satisfy the following condition:

$$\int_{A_\infty} \left(\overrightarrow{E_p^*} \times \overrightarrow{H_p} + \overrightarrow{E_p} \times \overrightarrow{H_p^*}\right) \cdot \hat{n_z} dA = 4P_p = 1. \tag{2.72}$$

The optical power carried by the entire coupled waveguide is given by:

$$P = \frac{1}{2}\int_{A_\infty} \left(\vec{E} \times \overrightarrow{H^*}\right) \cdot \widehat{n_z} dA = \frac{1}{2}\left[|A|^2 + |B|^2 + A^* B c_{12} e^{-j2\delta z} + B^* A c_{21} e^{j2\delta z}\right]. \quad (2.73)$$

and the system is assumed to be lossless. Note that all analyses that will be presented onwards will assume that losses are negligible and so are their effects on crosstalk [100].

Solutions to equations (2.68) and (2.69) are obtained by the following ansatz:

$$A(z) = \left(a_1 e^{jqz} + a_2 e^{-jqz}\right) e^{-j\delta z},$$

and

$$B(z) = \left(b_1 e^{jqz} + b_2 e^{-jqz}\right) e^{j\delta z}.$$

Then, constants a_1, a_2, b_1, and b_2 should satisfy the initial conditions:

$$a_1 + a_2 = A(0),$$

and

$$b_1 + b_2 = B(0).$$

With this in mind, the actual solutions of (2.68) and (2.69) are:

$$A(z) = \left[\left(\cos(qz) + j\frac{\delta}{q}\sin(qz)\right)A_0 - j\frac{\kappa}{q}\sin(qz)B(0)\right] e^{-j\delta z}, \quad (2.74)$$

and

$$B(z) = \left[-j\frac{\kappa}{q}\sin(qz)A_0 + \left(\cos(qz) - j\frac{\delta}{q}\sin(qz)\right)B(0)\right] e^{j\delta z}, \quad (2.75)$$

where $q = \sqrt{\kappa^2 + \delta^2}$.

The most intuitive case is when only one of the waveguides is excited with normalized power. Setting the initial light launching conditions to $A(0) = A_0$ and $B(0) = 0$, yields:

$$P_a(z) = \frac{|A(z)|^2}{|A_0|^2} = 1 - F\sin(qz)^2, \tag{2.76}$$

and

$$P_b(z) = \frac{|B(z)|^2}{|A_0|^2} = F\sin(qz)^2, \tag{2.77}$$

where the coupling efficiency is given by

$$F = \left(\frac{\kappa}{q}\right)^2 = \frac{1}{1 + (\delta/\kappa)^2}. \tag{2.78}$$

A very important characteristic from these equations is the coupling length:

$$L_c = \frac{\pi}{2q} = \frac{\pi}{2\sqrt{\kappa^2 + \delta^2}}, \tag{2.79}$$

which is when all of the power of the originally illuminated waveguide is completely transferred to the secondary waveguide. Note, when the propagation constants are equal, the coupling efficiency is maximum and the coupling length is simply given by:

$$L_c = \frac{\pi}{2\kappa}. \tag{2.80}$$

Interestingly, a good way of comparing the accuracy of the CMT to actual solutions of the coupled waveguide system is by looking at L_c [101].

2.3.2 Discussion of supermodes

Unlike the previous subsection, the discussion of supermodes will be rather short since the mathematical methods involved in actually solving them go beyond the scope of this text. However, it is

important to discuss this phenomenon because supermodes are modal solutions that arise from the actual boundary conditions of the composite multi-core waveguide. In comparison to CMT, cores are no longer treated as if they were alone and these modes are simultaneously excited when light is launched into one of them.

Assuming that we have a system of two identical fiber cores, exciting one of them generates an even and an odd supermode simultaneously, as seen in Figure 18. The propagation constant of isolated modes (β_i) lies in between the propagation constant of the even and the odd supermode, usually with $\beta_e > \beta_i > \beta_o$ (not in some cases, however [102]). Because the even and the odd modes have slightly different propagation constants, they interfere with each other over a distance:

$$L_c = \frac{\pi}{\beta_e - \beta_o}, \tag{2.81}$$

where β_e (β_o) is the propagation constant of the even (odd) mode [84], [88], [91], [102]. Interestingly, the beating of the supermodes gives the appearance of an isolated mode of one fiber interchanging its power with the other fiber in a sinusoidal fashion.

Under the conditions where CMT is still accurate enough, the superposition of isolated fiber modes can be used to compute the field profiles of supermodes. The coupling coefficient, κ, used in CMT may be used to calculate the even and odd supermode propagation constants and vice-versa by using [103]:

$$\beta_{e,o} = \frac{1}{2}(\beta_p + \beta_q \pm \delta\beta), \tag{2.82}$$

where $\delta\beta = \sqrt{\Delta\beta^2 + |2\kappa|^2}$ with $\Delta\beta = \beta_p - \beta_q$. It has been demonstrated that CMT depends on the V-number, the core-cladding index contrast (which is contained within the V-number as shown in (2.39)), and center-to-center separation between cores, all in the case of a multi-core fiber system [104], [105]. To our knowledge, however, none of those analyses (in the case of optical fibers) have gone beyond a refractive

index contrast ($n_{co} - n_{clad}$) of ~0.54 [97], [101]. Vectorial CMT was not used in this work, but results obtained for when $V > 2$ were indistinguishable from those obtained with the scalar theory [104]. Still, care must be taken for the kind of analysis that should be used and most have been done considering silica glass, not extremely strongly guiding hybrid ChG- polymer fibers. Therefore, CMT and the method presented in other works for approximating the supermode field profiles, propagation constants, and coupling lengths may no longer work for the fibers analyzed in this text, where $n_{co} - n_{clad} \gg 1$, because they are no longer weakly-guiding [98], [103]. Additionally, supermodes obtained this way are not solutions to Maxwell's equations, but are good approximations to what the actual modal solutions are [98].

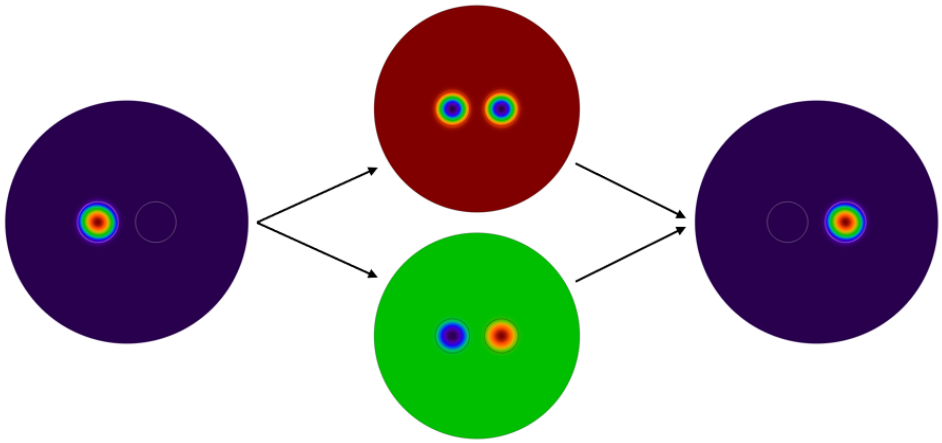

Figure 18: When two identical fiber cores are placed near each other, launching light into one of them simultaneously excites an even and an odd supermode. The superposition of both supermodes generates a beating pattern along the direction of propagation that varies sinusoidally as in (2.76) and (2.77), and power will be fully transferred to the adjacent core after L_c. Modal profiles for the top image were calculated numerically using the finite-element method (FEM).

In case κ no longer holds (which is when CMT is no longer a good approximation), the analysis of composite waveguides becomes extremely tedious and actual analytical solutions to Maxwell's equations must be found for a given system. Fortunately, numerical methods are well suited for solving these

problems and the FEM was used in this work. Throughout the years, analytical solutions to vector normal modes have been presented [99], [106]–[112]. In summary, three main methods may be used for solving for vector normal modes in multi-core strongly-guiding fiber bundles. These are: the point-matching method [108], the Rayleigh method [112], and the circular harmonics expansion method (also known as Wijngaard's method) [106]. The multipole method has been previously applied to the analysis of imaging fiber bundles [84] and it branches off from the Rayleigh method [109].

Another important takeaway about supermodes is how the can be used to qualitatively determine the state of how coupled cores are in a multi-core fiber system. In [88], it is shown that when considering two waveguides, placing them away from each other yields a "breakdown" in the supermode propagation constants. Meaning that if two identical fibers are considered, increasing their center-to-center spacing will eventually decouple them and the propagation constants of the supermodes will be that of the isolated fibers. Interestingly, the same occurs when introducing a core-size mismatch, as seen in Figure 19.

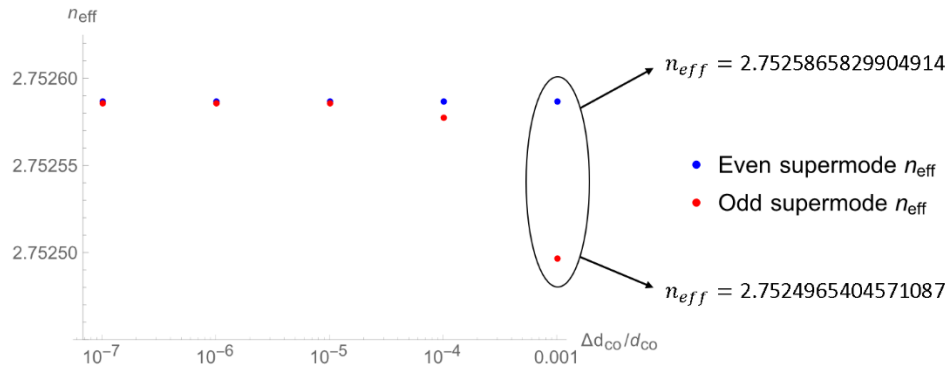

Figure 19: Fundamental supermode effective index, n_{eff}, versus core size mismatch, where d_{co} is the core diameter and Δd_{co} is the difference in core diameter. A system of two identical fiber cores as in Figure 18 is considered, where both have a $7\mu m$ diameter and a $10\mu m$ center-to-center spacing. The supermode "symmetry" breaks when a significant core-size mismatch is introduced. This makes it so that the n_{eff} of the even and odd supermodes that

exist eventually become those of the isolated cores. Which means that they are no longer coupled. Also, for the entire waveguide system, $n_{co} = 2.8$ *and* $n_{clad} = 1.67$.

An additional detail about Figure 19 is that the right-hand core was reduced in diameter while the left-hand core was unchanged. Hence, why the red mark was the most severely shifted. The n_{eff} values of the supermodes were calculated using the FEM for the two-core system and the n_{eff} of the decoupled cores was calculated analytically using equation (2.54) since after a large enough core-size mismatch the cores of the two-core system may be treated independently (these values matched the FEM almost exactly, as well). The effects of varying the core sizes will be further investigated in the following subsection.

2.3.3 CMT example: slab waveguides

With CMT introduced, the purpose of this subsection is to compute and examine the coupling between two waveguides to apply these concepts to the optical fibers that will make up our CFB to better understand how to reduce crosstalk. To begin, we consider a pair of high-index slab waveguides surrounded by a lower-index medium, as seen in Figure 20. Four different cases are shown to demonstrate how coupling is affected by changes and imperfections in the system. In the first case, both slabs are identical in diameter ($7\mu m$), but their center-to-center spacing is $12\mu m$. The second case considers slabs of the same dimension but they are brought closer together to have a center-to-center spacing of $10\mu m$ (the same spacing that we aim to have in our fiber bundle). The third case considers the same $10\mu m$ center-to-center spacing but the diameter of core 2 is reduced by a factor of 0.9999. Lastly, the fourth case considers identical waveguides of $7\mu m$ in diameter and a center-to-center spacing of $10\mu m$, but it looks at cross-mode coupling.

Using $n_1 = n_2 = 2.8$ and $n_0 = 1.67$ as in the slab waveguide analysis section, we know that the fundamental TE mode for both identical $7\mu m$ slabs has an effective index of $n_{eff} = 2.7811645867351555$ in isolation. Then, by plugging in E_y and $H_x = -(\beta/\omega\mu_0)E_y$ into (2.67) we obtain:

$$\kappa = \frac{\omega\epsilon_0(n_1^2 - n_0^2)\int_{A_{co,1}} E_{1,y}^* \cdot E_{2,y}dx}{\frac{2\beta_1}{\omega\mu_0}\int_{A_\infty}\left|E_{1,y}\right|^2 dx}, \tag{2.83}$$

where waveguide 1 is the one located at $x = 0$. Note, $\kappa = \kappa_{12} = \kappa_{21}$ (again, assuming that κ_{pq} is real) because only minuscule changes will be made to the position and diameter of the waveguides. With equation (2.83), κ is computed to then be plugged into (2.78) to plot equations (2.76) and (2.77) for the four cases seen on Figure 20.

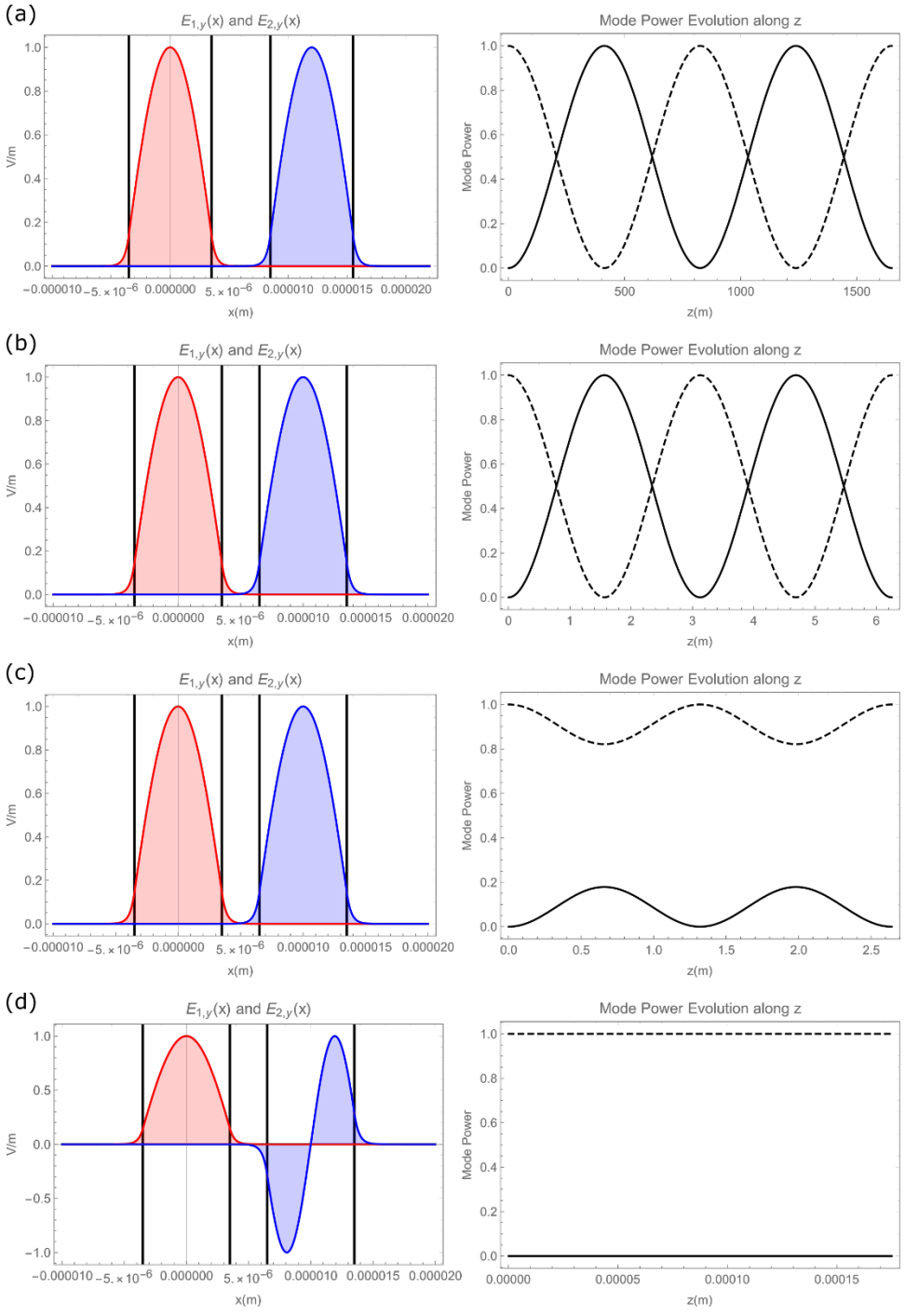

Figure 20: Demonstration of CMT for the four different cases described in the text.

A lot of information can be extracted by examining the four cases presented in Figure 20. To best understand the information, waveguide 1 (on the left and centered at $x = 0$) is illuminated and its power eventually makes its way into waveguide 2 (right), which is unilluminated. Beginning with the first and second cases, located at the top of Figure 20, the coupling efficiency was at 100% for both, but the rate at which light went from the illuminated to the unilluminated waveguide and back increased when the center-to-center spacing was reduced from $12\mu m$ to $10\mu m$. The rate at which power oscillates between waveguides is known as the coupling strength. Strongly-coupled waveguides exchange power rapidly along the direction of propagation, while weakly-coupled waveguides exchange power slowly. For the third case, the rate of power transfer is much higher but the slight difference in core sizes affected the coupling efficiency, reducing it to 17.8484%. In the fourth case, the amount of power that was transferred was negligible. This was expected because modes of unequal propagation constants may be treated as them being orthogonal or their effective phase velocities being too different for them to significantly couple along the direction of propagation. The best way to understand the fourth case is by thinking of light rays that reflect at a slightly different angle when leaking into an adjacent waveguide and exciting another mode. This, of course, is not a common occurrence and in many cases may be neglected.

In conclusion, placing waveguides closer to each other increases the rate of coupling, but the introduction of a slight error in core size is enough to decouple the waveguides. It is important to note, however, that the error (or difference) in core size needed to decouple the waveguides depends strongly on the refractive index contrast between the core and the cladding. The higher the contrast (as in our case) the smaller the change needed to inhibit coupling.

As mentioned in the introduction to this section, there are two versions of CMT. One is the orthogonal and the other is the non-orthogonal CMT. The difference between the two was closely looked at by [92] and they concluded that, despite their differences, both gave similar results and either could be used. Results obtained in this section were double-checked with FEM simulations and all results agreed

very well. To clarify, orthogonal CMT is being used in this work. This version of the CMT assumes orthogonality between modes and tends to neglect the self-coupling coefficient χ_p, which we did in the analyses presented in this subsection. Note, our χ_p was in the order of 10^{-4}.

2.4 Analysis of crosstalk and disorder induced isolation of multimode fibers

As it is probably evident at this point, due to the core-cladding index contrast and the larger 7μm core diameter used, one can easily deduce that we are working with extremely multimoded fibers. This is a good quality to have since these kinds of fibers can collect a lot of light, making them ideal for imaging bundles. However, there are hundreds of other fibers around them, which means that we must consider the overall coupling between all of the modes and fiber launching conditions from a lens to begin to analyze crosstalk. The analysis presented in this section can be thought of as a simplification of CMT tailored to extremely multimoded fibers, which makes it readily applicable and good for analyzing crosstalk in fiber bundles. As this subsection progresses, we will analyze the crosstalk evaluation method presented by [100] and briefly mentioned in [98]. This method was later expanded on by [48] for evaluating the performance of fiber bundles for endoscopes.

First of all, like in the previous section, analyses will be kept to two cores only. Since there will be hundreds of thousands of fibers in our CFB, understanding the coupling mechanism between two gives a very good and general idea of what occurs when more are present, as noted by [113]. The next most common analysis is the seven-core array, where one-seventh of the power oscillates from the central core to the surrounding cores and back (when all cores are identical) [84]. And just as in the two-core case, changing the size of one or more cores decouples them from the rest; thus, making all power stay confined within the originally illuminated waveguide or those identical to it. Second, an equilibrium condition is reached after an incredibly long distance in multimoded fibers [100]. At this equilibrium condition, all of the modes that are excited beat between cores until all of the power is distributed among all cores.

To begin, we concentrate on the analyses presented in [100]. It is assumed that the core diameter is large enough to hold many modes and the index contrast between the core and cladding is small. In our case, we have the opposite. Our aim is to fabricate cores with diameters of 7μm and with a refractive index contrast greater than unity. A good compromise, however, between Snyder's method and ours is the fiber's V-number. As shown in equation (2.39), the V number is directly proportional to the NA and the fiber's core radius. This means that, although the assumption used by Snyder cannot be used with our fibers, they can still be applied because of the large V-number. For example, we may have a fiber with a V-number of 10 because of a high index contrast and a not-so-large core radius or because of the opposite. Additionally, light-ray methods may be used too since the fibers are multimoded [98], and the methods presented in this section take advantage of that for launching conditions, as shown in Figure 21.

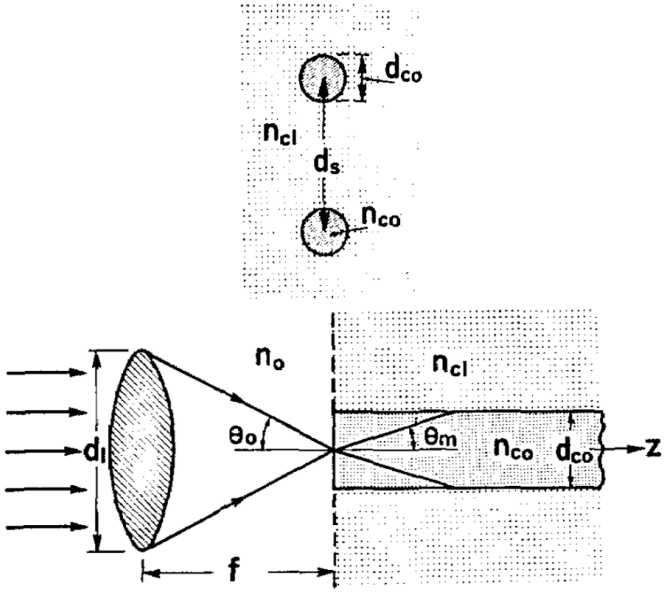

Figure 21: Front view of a two-core fiber system with both cores sharing a common cladding (top) and a side view of that same system, but with light launching conditions (bottom). Image obtained from [100].

At 100% coupling efficiency and using the same light-launching conditions as before, core 1 is excited while core 2 is not. After light propagates some length, it leaks into core 2 and then it leaks back to

core 1 in a sinusoidal fashion as described by equations (2.76) and (2.77). Even though orthogonal CMT shown in the previous subsection is not enough to describe cross-mode coupling because mode orthogonality is assumed, it has been shown that only coupling between like-modes is significant [91]. This means that to describe the coupling of multimode fibers, cross-mode coupling may be neglected while the summation over all like-modes (modes with almost identical propagation constants) needs to be considered. It was shown in [100] that when $V \gg 1$ and for all hybrid (HE_{1m}) modes

$$C_q = \frac{2\theta_c}{d_{co}} \cdot \frac{U_q^2}{V_2^5} \cdot \frac{e^{-2V(D-1)}}{(\pi D)^{1/2}}, \tag{2.93}$$

where C_q is the coupling coefficient between qth modes, $\theta_c = \sqrt{1 - n_{clad}^2/n_{co}^2}$ is the complementary critical angle,

$$V = \frac{\pi d_{co} n_{co} \theta_c}{\lambda} \tag{2.94}$$

is the fiber parameter, U_q represents the zeros of the Bessel functions of the first kind of zeroth order (i.e., $J_0(U_q) = 0$), and $D = d_s/d_{co}$ is the ratio between the center-to-center spacing between cores (d_s) and the fiber's core diameter (d_{co}). Note that unlike how we define the V-number in equation (2.39), (2.94) is used for the analyses done in this section.

Then, it follows that the total power that leaks into the unilluminated core from the excited core can be expressed as:

$$P_2 = \sum_{q=1}^{m} P_{in}^q \sin(C_q z)^2, \tag{2.95}$$

where P_{in}^{q} is the input power of the qth mode in the illuminated fiber and m corresponds to the maximum number of hybrid HE_{1m} modes that the fiber can support. Also, the total input power of the illuminated fiber is:

$$P_{in} = \sum_{q=1}^{m} P_{in}^{q}. \tag{2.96}$$

From these few equations, it can already be seen that the total crosstalk in multimoded fibers is treated as the summation of the coupling between all HE_{1m} modes. By converting the summations into integral expressions, as detailed in [100], the following expression for an ideal optical system was derived:

$$\frac{P_2}{P_{in}} = \frac{1}{2}\left(1 - \frac{\sin(L)}{L}\right), \tag{2.97}$$

where L is a dimensionless length given by:

$$\frac{4\theta_c z}{d_{co}}\left(\frac{\theta_m}{\theta_c}\right)^2 \cdot \frac{e^{-2V(D-1)}}{(\pi V D)^{1/2}}, \tag{2.98}$$

with $\theta_m = n_{air} d_l / 2 n_{co} f$ (where d_l is the diameter of the lens used to launch light into the fiber and f its focal length). By plotting equation (2.97) in Figure 22, it can be seen that after some distance, an equilibrium condition is reached when fibers carry equal powers. Note, the length where this equilibrium condition is enormous unless fibers are very close together [98].

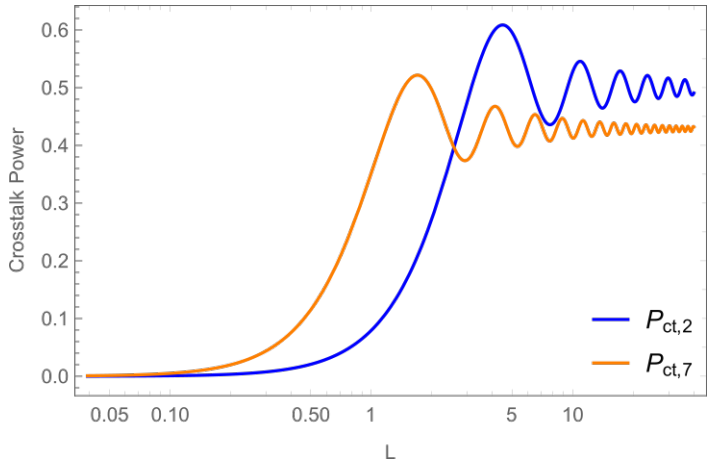

Figure 22: Crosstalk power (P_{ct}) that leaks into the unilluminated fiber after some dimensionless length L. Blue trace is for two identical fiber cores placed next to each other separated by some center-to-center distance d_s. The orange trace describes a similar scenario but with six cores surrounding a central one. As described in the text, after some long distance, the power eventually reaches equilibrium and is distributed among all cores.

For the seven-core fiber array case, or if a core-size mismatch is introduced (affecting F) equation (2.97) may be multiplied by $6/7$ or F, and L replaced by $\sqrt{7}$L or L/$\sqrt{\text{F}}$, respectively.

In the CMT subsection, it was seen that not having identical cores reduces F and the power transfer between them can be reduced; hence, reducing crosstalk in the system. The same occurs in optical fibers. Fortunately, when dealing with fibers with large V-numbers, the core-size imperfection needed to fully decouple them is much less than a tenth of a percent ($\ll 0.1\%$). Similar to equation (2.78), for multimoded optical fibers it can be found by using:

$$\text{F} = \frac{1}{1+\text{X}^2}, \tag{2.99}$$

where

$$\text{X} = \frac{1}{2}(\pi \text{DV}^3)^{1/2}\left(\frac{\Delta \text{d}_{\text{co}}}{\text{d}_{\text{co}}}\right)\text{e}^{2\text{V}(\text{D}-1)}. \tag{2.100}$$

We decided to examine two cases, which correspond to two material combinations that we considered for the fiber bundle. Both core glasses have indices of ~2.8 in the MWIR but one can be drawn with a fluoropolymer with a refractive index of ~1.3 and the other with a polymer of index ~1.67 (both in the MWIR). Assuming $d_{co} = 7\mu m$ for both and a $d_s = 10\mu m$ gave what is presented in Figure 23.

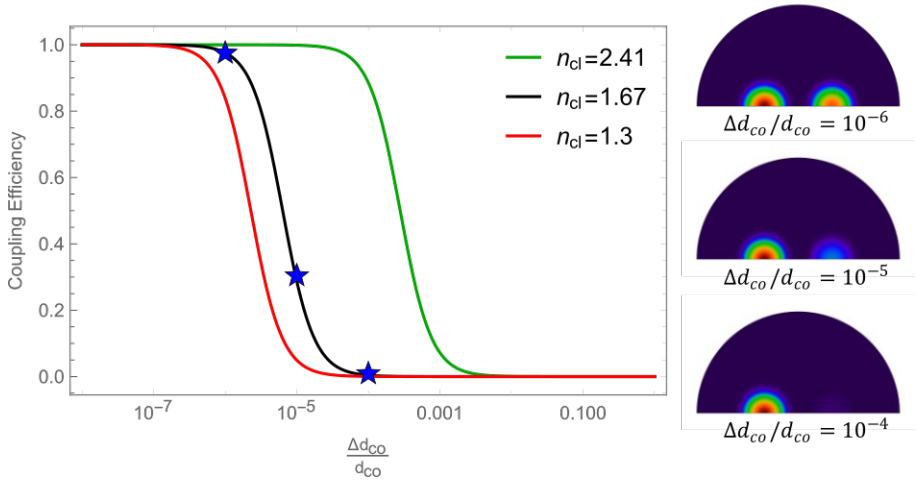

Figure 23: Core size mismatch ($\Delta d_{co}/d_{co}$) versus coupling efficiency in a coupled two-core multimode fiber system. Black and red traces correspond to refractive indices of polymers used as cladding materials, ~1.67 and ~1.3, respectively. The green trace corresponds to a lower-index ChG that many be used as a cladding material instead with an index of ~2.41. Supermode profiles on the right correspond to the $n_{cl} = 1.67$ case, where the diameter between the two cores is mismatched by a factor of 10 (blue stars) by shrinking the core on the right, the supermodes break down as shown in Figure 19.

As expected, the core-size mismatch needed to fully decouple the cores of materials that we are considering is extremely small. The coupling efficiency obtained for each of the supermode cases was $F = 0.98$ for $\Delta d_{co}/d_{co} = 10^{-6}$, $F = 0.29$ for $\Delta d_{co}/d_{co} = 10^{-5}$, and $F = 0.004$ for $\Delta d_{co}/d_{co} = 10^{-4}$. This means that slight core-size errors that occur during the fabrication process alone will be more than enough to decouple the fibers in the CFB and inhibit most, if not almost all, crosstalk.

One last takeaway from the analyses done in this section is the actual length needed for the crosstalk power to reach the equilibrium condition. Another way of visualizing this result is by replacing the dimensionless length L in equation (2.97) by the fiber's direction of propagation, z. Assuming that we use an F/1 ($d_l = f = 1\text{cm}$) lens to couple light into the two-core fiber system, with equations (2.97) and (2.98), we obtain Figure 24. The additional curve in Figure 24 represents the crosstalk power for when there is a core-size mismatch of $\Delta d_{co}/d_{co} = 10^{-5}$.

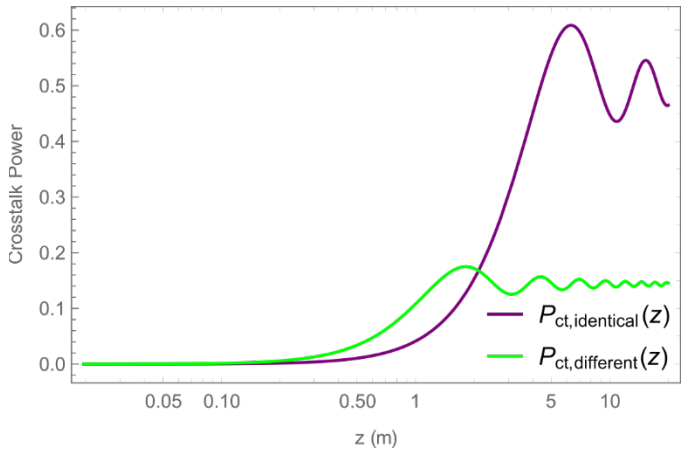

Figure 24: Total crosstalk power (P_{ct}) that leaks into the unilluminated core along the direction of propagation when cores are identical (purple) and different by $\Delta d_{co}/d_{co} = 10^{-5}$ (green).

As it can be seen in Figure 24, the crosstalk power equilibrium condition will not be reached within the maximum length of our bundle, $\sim 5\text{cm}$, with $n_{co} \approx 2.8$ and $n_{cl} \approx 1.67$. Interestingly, for the identical cores case, the equilibrium condition begins at a distance similar to the coupling length ($\sim 4\text{m}$) of the fundamental supermodes. When the fibers are unidentical, the equilibrium condition occurs before (similar to what was seen in the CMT for slab waveguides section where the coupling length of dissimilar waveguides was shorter) but the total crosstalk power is lower, which means that most of the power will remain in the illuminated core. Introducing a larger $\Delta d_{co}/d_{co}$ will completely decouple the cores and inhibit

almost all crosstalk power. As a visual example of how crosstalk and the equilibrium condition looks like, observations made in [113] are shown in Figure 25.

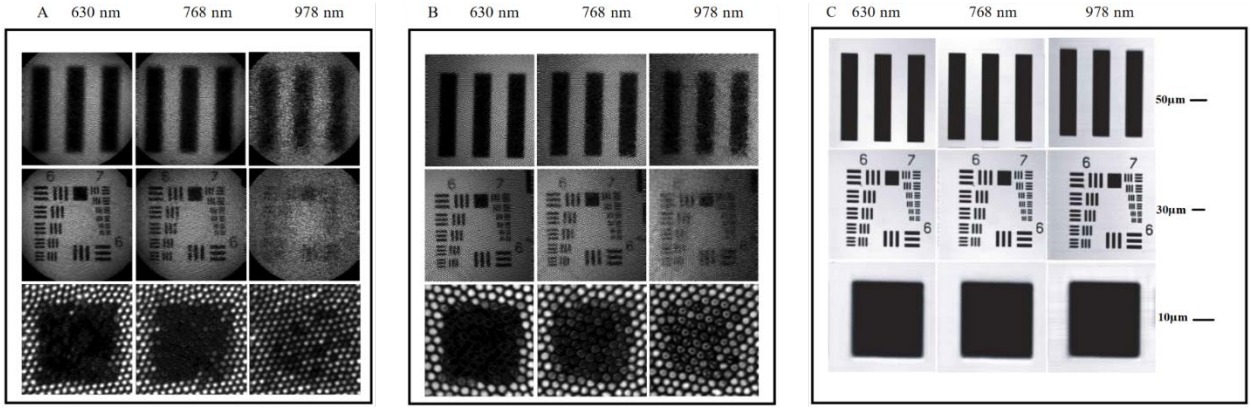

Figure 25: Fiber bundle performance at three different wavelengths for the Fujikura 350S (A) and Fujikura 500N (B). Test target used for testing (C). The smudging or "spread" of the image in the bundle, which leads to a loss of resolution, is due to coupling effects and the equilibrium condition from all of the different modes coupling and interacting together. Although harder to visualize at longer wavelengths, the image is not just a smudge because of unavoidable core-size imperfections throughout the entire bundle. Image obtained from [113].

Chapter 3: Materials Selection for MWIR Coherent Fiber Bundles

Choosing the appropriate materials for the IR CFB that we are designing is critical for it to have good performance and relay images in the MWIR (and possibly the LWIR given the right core dimensions and separations). This chapter delves into the materials we selected for the application and each section is dedicated to a different consideration. The first section will delve into glasses that could be used for the application and explains why we decided to use chalcogenide glasses. Polymers that are thermally matched to the glasses presented in the first section will be discussed in the second section. The third section is more unique, in that it discusses losses (absorption and Fresnel reflections) and the imaginary part of some of the polymers chosen was measured and presented. Finally, the rheology section discusses and shows the viscosity curves for the glasses and the polymer that we plan to draw our fibers with.

3.1 Materials selection for the application

Silica glass (SiO_2) is the most used material in the making of optical fibers because of its optical purity, low losses (up to a wavelength of $\sim 1.6\mu m$), and mechanical properties. This glass possesses a high transition temperature of $1175°C$, a thermal expansion coefficient of $0.55 \cdot 10^{-6}/°C$, and a Young's modulus of 70GPa [47]. Unfortunately, applications further in the MWIR and LWIR are not as common, so research and development of glasses and optical fibers that operate in that region has not been as in-depth as with silica. In fact, one of the challenges that exists today is to find a glass with properties similar to silica, but capable of transmitting light with low losses at the emission wavelength of CO_2 lasers ($\sim 10\mu m$) [47]. Two glasses that transmit in the IR exceptionally well and are currently gaining popularity are chalcogenide (ChG) and fluoride glasses (FGs). Of these two, ChGs were chosen for our application and the reasons why will be discussed in the following subsections.

3.1.1 Fluoride glasses

In the mid-1970s, Poulain and Lucas accidentally discovered FGs [114], [115]. Interestingly, some of these glasses possess some improved optical properties over silica glass. The most significant of these is the loss, as seen in Figure 25. Also, FGs have a much broader transmission that spans from the visual to the MWIR and LWIR spectrum depending on the composition [116].

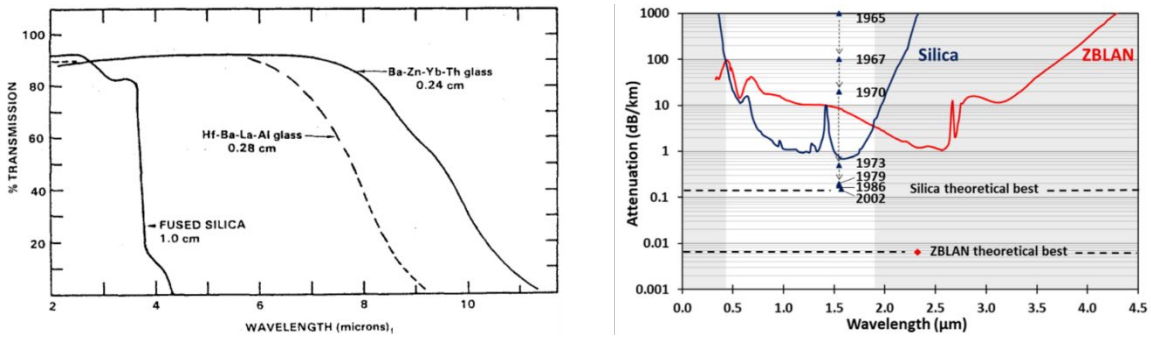

Figure 26: Transmission spectrum of some fluoride glass fibers (left) and the improved loss of silica fibers over the years compared to Le Verre Floure's current ZBLAN fiber and its lower theoretical loss (right). Images obtained from [116], [117].

Now, all of these reasons may imply that FGs should have replaced silica since its inception, especially given its broad transmission and theoretical low losses. However, what these glasses lack and makes them undesirable for some applications are their mechanical and thermal properties [47]. Plus, not all FGs can be drawn into optical fibers. The most common types of FGs for this are fluoroaluminate ($AlF_3 - ZrF_4 - BaF_2 - CaF_2 - YF_3$), fluorozirconate (ZBLAN, $ZrF_4 - BaF_2 - LaF_3 - AlF_3 - NaF$), and fluoroindate (IFG, $InF_3 - ZnF_2 - SrF_2 - BaF_2$) glasses, where ZBLAN and IFG are readily available commercially [118].

Despite all of the information presented, the following question must be asked: how would an IR CFB for imaging applications made of these fibers perform? When considering fibers made of these glasses, it is important to know that they have a refractive index close to that of silica, which is in the range of $n \approx$

$1.45 - 1.6$ [116]. That property combined with lower transition temperatures ($\sim 265℃$ for ZBLAN, for example [47]) makes it hard to match FG fibers with a polymer or glass with a lower refractive index. Even if it were possible to have the cores suspended with an air cladding, the index contrast between the core and the cladding would only be of about ~ 0.6, which is not as good as the next type of glass that we will analyze. This property is important because the larger the contrast, the larger the amount of light that these fibers will be able to collect, as described by the NA. In summary, FG fibers possess a big potential for applications in the IR. But, unless their refractive index were to somehow be increased past n $\approx$1.6, they are not the best candidates for making IR CFBS for thermal imaging.

3.1.2 Chalcogenide glasses

ChGs are starting to become the go-to glass in the area of IR fiber optics because of their optical characteristics, stability, durability, chemical resistance, moisture resistance, and they do not need as many elements to make as FGs. Like FGs, ChGs possess similar thermal properties and lack of mechanical robustness. ChGs actually have a quite detrimental potential to crystallize when drawn into fibers, which is something that must be considered before drawing them at higher temperatures. However, what really sets these glasses apart is their broad transmission deep into the IR and their higher-than-normal refractive index as seen in Figure 27 and figure 28, respectively.

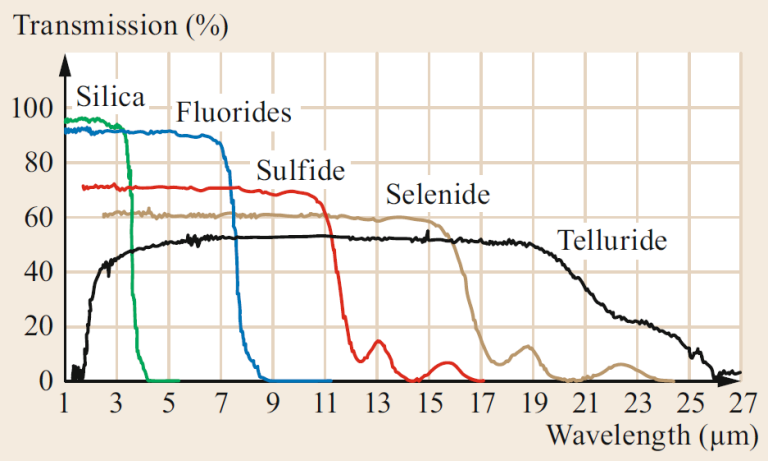

Figure 27: Transmission spectrum of silica, fluoride, and chalcogenide glasses. Image obtained from [58].

In the introductory chapter of this work, a brief explanation of the history and typical elements that are used to make these glasses was given. Although many combinations are possible, not all may be used to make infrared fibers. Those that can, however, have stood the test of time and are slowly but surely becoming the industry standard. Some of the most popular compositions (which are also available commercially [119]–[122]) are As_2S_3, As_2Se_3, $Ge-Se-Te$, and $Ge-As-Se-Te$.

These glasses possess a number of favorable characteristics, the most important being their higher refractive indices. Those chosen for this work and listed in Table 1 have indices higher than > 2.7 in the MWIR. Another good characteristic is their tailorable chemistry, which gives the ability to control their refractive indices and transition temperatures. For example, adding more Se or Te increases the index of refraction more due to these elements being more polarizable while glasses with higher Te content have been shown to have lower transition temperatures [47]. In addition, these glasses have the unique ability to be co-drawn with robust low-index polymers because of their lower transition temperatures [74].

For this reason, we chose ChGs to make our bundle. By being able to draw ChGs with robust low-index polymers, we have three key advantages not possible with conventional fiber optics in the visible spectrum. These are: (1) tight confinement of light within the fiber's core, which significantly lowers the

cladding-induced absorption losses, (2) extremely large NA for improving collection of light and making it possible to couple with fast lenses, and (3) crosstalk may be easily inhibited with nanometer-sized imperfections that occur during the drawing process or are made to occur by design.

Glass	Refractive Index at $\lambda = 4\mu m$	Transition Temperature (T_g)	Young's Modulus	Modulus of Rupture
As_2Se_3	~2.8	185°C	18.3GPa	17MPa
$Ge_{30}As_{13}Se_{32}Te_{25}$	~2.8	275°C	22.0GPa	18MPa
$Ge_{20}As_{15}Se_{25}Te_{40}$	~3.4	212°C	N/A	N/A
$Ge_{10}As_{10}Se_{10}Te_{60}$	~3.65	174°C	N/A	N/A

Table 1

We have made it our goal to achieve these three key advantages, and to do so we chose the ChGs listed in Table 1. The first two glasses, As_2Se_3 (Vitron-IG6) and $Ge_{30}As_{13}Se_{32}Te_{25}$ (Vitron-IG3), are commercially available and their information was obtained from the manufacturer [123]. The other two glasses, Te_{40} and Te_{60}, were first reported in the 1980s [124], but are not commercially available. Despite this, Te_{40} and Te_{60} would be great to use in IR CFBs as long as they can be ordered from a vendor or manufactured in-house.

All of these ChGs have been drawn into fibers, and were chosen because of their lower transition temperatures ($< 300°C$), higher refractive indices (>2.7), low dispersion (Figure 28), and good transmission (Figure 28) [56], [124], [125]. Another common ChG used in infrared fibers is As_2S_3. This glass, however, has a refractive index of ~ 2.41 at $\lambda = 5\mu m$ [126], which is acceptable but having other readily available glasses (IG3 and IG6) with much higher indices and similar properties makes them more suitable for making IR CFBs.

A final and very important property of ChGs is the coefficient of thermal expansion (CTE), which is crucial in the design and implementation of IR CFBs. For IG6 and IG3, the CTE is $207 \cdot 10^{-7}/°C$ and

$134 \cdot 10^{-7}/°C$, respectively [127]. For Te_{40} and the Te_{60} it is $160 \cdot 10^{-7}/°C$ and $165 \cdot 10^{-7}/°C$, respectively [124].

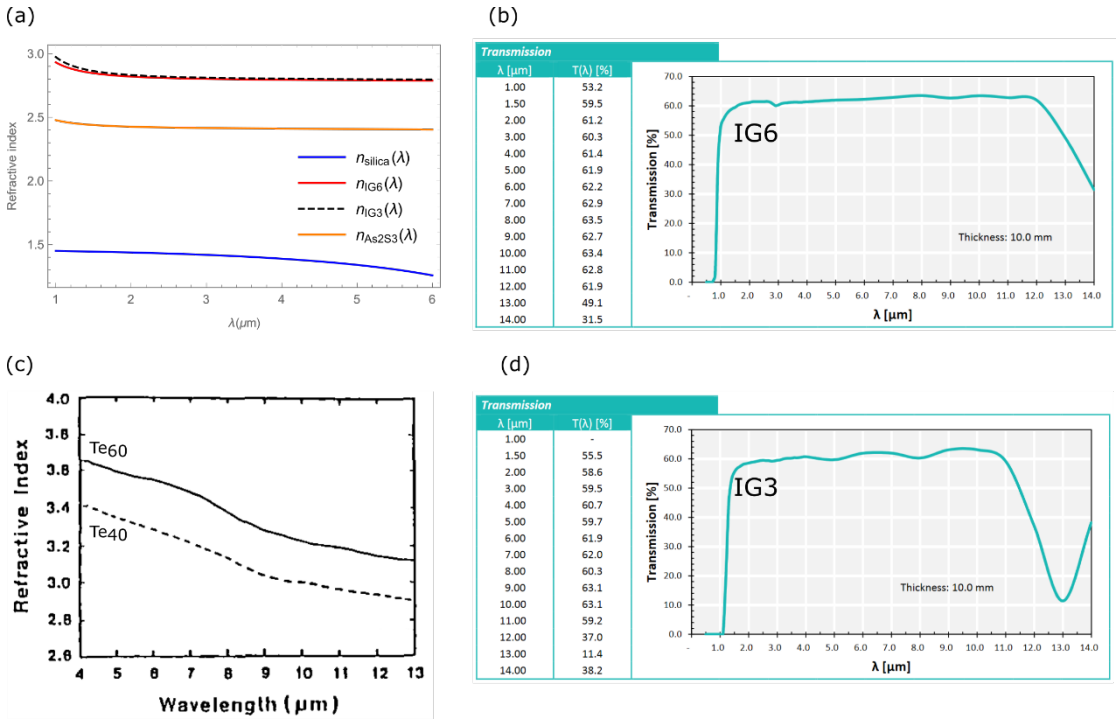

Figure 28: Dispersion curves of various common chalcogenide glasses (ChGs) and silica (a) in addition to Te_{40} and Te_{60} from [124] (c). Transmission curves of Vitron-IG6 (As_2Se_3) (b) and Vitron-IG3 ($Ge_{30}As_{13}Se_{32}Te_{25}$) (d) from [123]. Note that the transmission of Te_{40} and Te_{60} is very similar to IG3's in (d).

3.1.3 Polymers

The world of polymers is vast and complicated. There is always a new polymer to discover due to constantly evolving applications that require the most cutting-edge materials. Because of this, the development of great plastics for a myriad of applications became a possibility. Without diving into specifics, this subsection will detail the selection of polymers that are best thermally suited to make up the common cladding of the IR CFB we are designing in this work.

Thermoplastic polymers, as the name implies, are materials that become moldable (rubbery) at elevated temperatures and solidify when cooled down again. We considered many polymers but after choosing the four ChG candidates (shown in Table 1), we narrowed it down to three as seen in Table 2.

Polymer	Refractive Index	T_g or Melting Temperature (T_m)	Young's Modulus	Modulus of Rupture
PEI	$\sim 1.6 \ @ \ \lambda = 4\mu m$	$T_g = 216°C$	3.04GPa	159MPa
PES	$\sim 1.641 \ @ \ \lambda = 0.6563\mu m$	$T_g = 225°C$	2.7GPa	162MPa
FEP	$\sim 1.3 \ @ \ \lambda = 4\mu m$	$T_m = 260°C$	0.35GPa	586MPa

Table 2

The information presented in Table 2 was primarily obtained directly from manufacturer specifications since all of the polymers are available commercially. Data on PEI was obtained from [128]–[132], for PES it was obtained from [133]–[136], and for FEP it was obtained from [56], [137], [138]. Note that it is strongly recommended to contact a polymer's supplier to verify exactly all optical, mechanical, and thermal properties since they tend to vary between manufacturers. That being said, values presented in Table 2 should be used as reference or for modeling purposes only.

The mechanical, thermal, and optical properties of the polymers presented in Table 2 make them ideal to be co-drawn with ChGs to make infrared fibers. Starting with polyetherimide (PEI), it is a robust amber-colored amorphous thermoplastic used to make containers and chemical lab equipment due to its heat and chemical resistance [139]. Polyethersulfone (PES or PESU) is primarily used in aircraft interiors, automotive parts, electrical components, and medical equipment [140]. Like PEI, PES is amorphous, rigid, tough, and stable over a wide range of temperatures; plus it has a high resistance to chemicals. A little different from PEI and PES is fluorinated ethylene propylene (FEP). FEP is a fluoropolymer, meaning that

this polymer belongs to a "family" of polymers characterized by their high resistance to solvents, acids, and bases [141]. Also, FEP is stable over a wide range of temperatures, but it differs from PEI and PES in that it is actually a semi-crystalline polymer [141]. This means that, unlike amorphous polymers, it has a glass transition temperature T_g and a melting temperature T_m, thus making it a bit more challenging to draw with ChG [142].

As in the previous section, it is important to mention that all of these polymers have relatively low thermal expansion coefficients, FEP being the one that expands the most. For PEI it is $56 \cdot 10^{-6}/°C$ [143], for PES it is $55 \cdot 10^{-6}/°C$ [144], and it is $83 - 104 \cdot 10^{-6}/°C$ for FEP [145]. This parameter is crucial depending on the application since the thermal expansion and contraction of materials in a bundle might cause fractures on the glass or other undesired effects to occur.

Despite the myriad of applications where these polymers are used, little information exists about their optical properties in the IR. Some findings have been reported recently on the refractive index of some common polymers, including PEI [146]. In a publication where an IR CFB was developed with IG3, FEP was used for the cladding and was characterized by using Fourier Transform infrared (FTIR) spectroscopy [56]. To better model the performance of the IR CFB that we are developing, we measured the transmission of PEI and PES films used in our fiber fabrication process with an attenuated total reflectance FTIR (ATR-FTIR) spectrometer. This tool uses an evanescent wave, resulting from total internal reflection, that leaks into a sample. Because the evanescent wave extends to about $0.5 - 2\mu m$, depending on the wavelength, this tool can be used to measure the transmittance of thin-films such as those we are using to make our fibers [147]. After careful cleaning and preparation of the $120\mu m$ thick films of PEI and PES, the results that we obtained from ATR-FTIR are shown in Figure 29.

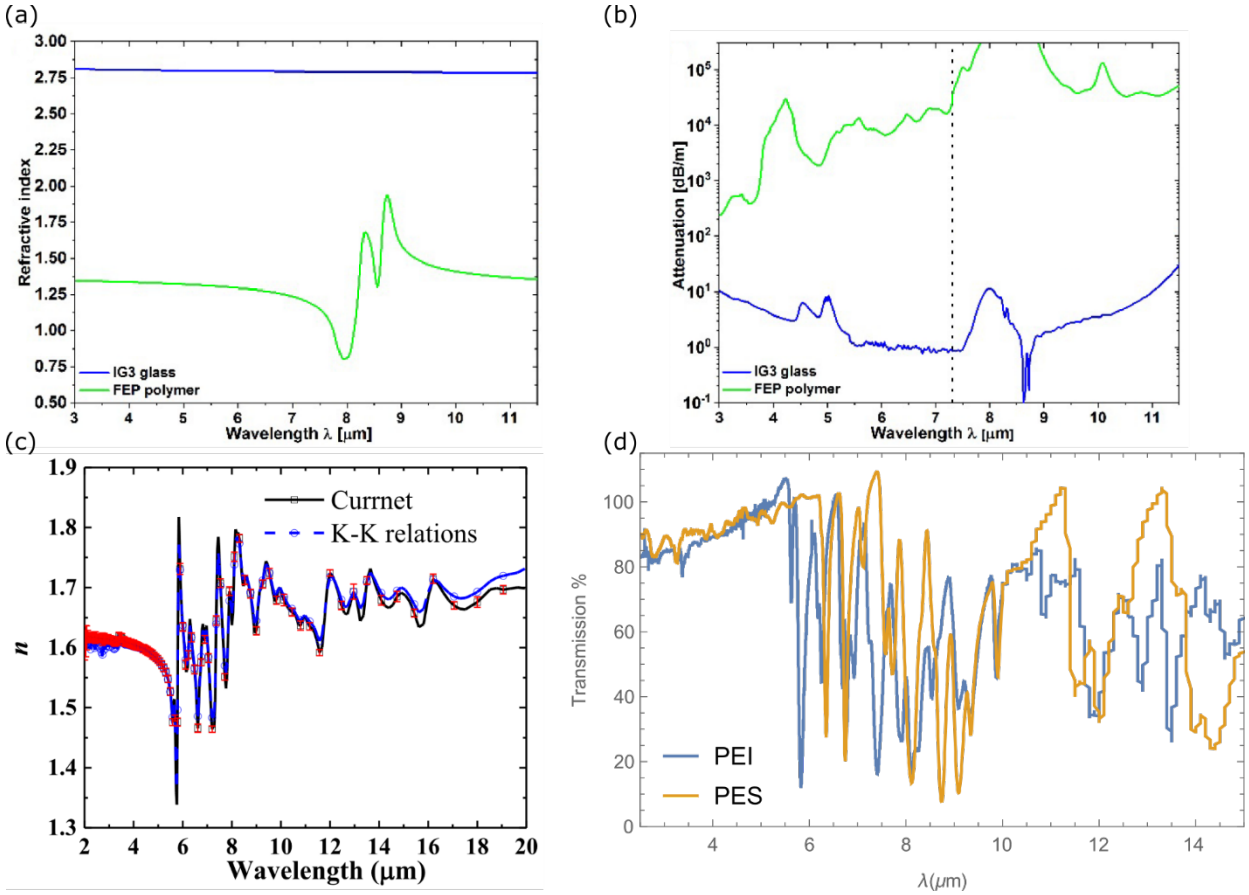

Figure 29: Dispersion curves of FEP (with IG3) from [56] (a) and PEI from [146] (c). Transmission data of an 0.86mm ($3-7.3\mu m$) and 0.05mm thick FEP ($7.3-11.5\mu m$) sample with transmission data of a core-only IG3 fiber with a $240\mu m$ diameter from [56] (b). Measured transmission of $120\mu m$ thick thin-films of PEI and FEP. Note that transmission exceeds 100% at some points due to instrument error but is closer to 100% at those points [148].

Because of its good transmission and favorable dispersion in the MWIR, we chose to use PEI to draw our fibers with IG3 and IG6 glass. PEI is thermally compatible to IG6 but its transition temperature is too low for drawing IG3 with it. We originally considered using FEP to draw with IG3, but because of the fumes that it might release while thermally preparing it and its semi-crystalline nature would conflict with the way in which we are drawing the fibers. More is discussed in the next chapter.

3.2 Computation of losses

Although we previously ignored them, losses are unavoidable. Two of our greatest concerns while using high-index glasses for the core and lossy polymers for the cladding were Fresnel reflections and absorption losses, respectively. Both effects will be looked at in the following subsections and methods on how to avoid them will be detailed.

3.2.1 Fresnel reflections

When light is incident onto a boundary between two materials, there is some amount of it that is reflected while the rest is transmitted. This can be expressed as a function of angle of incidence and tied to the angle of transmission by Snell's law. To quantify this loss, it is necessary to compute the reflectance, which depends on the polarization of light, and is given by [149]:

$$R_{\perp} = \left| \frac{n_1 \cos\theta_1 - n_2 \cos\theta_2}{n_1 \cos\theta_1 + n_2 \cos\theta_2} \right|^2 \tag{3.1}$$

and

$$R_{\parallel} = \left| \frac{n_1 \cos\theta_2 - n_2 \cos\theta_1}{n_1 \cos\theta_2 + n_2 \cos\theta_1} \right|^2, \tag{3.2}$$

where n_1 is the refractive index of the medium where light is, n_2 is the refractive index of the medium where light is going into, θ_1 is the angle of incidence with respect to a surface normal line, and θ_2 is the angle light makes when going into the next medium with respect to a surface normal line and related to the incidence angle by Snell's law, $n_1 \sin\theta_1 = n_2 \sin\theta_2$. As it was done in the previous chapter, assuming that the refractive index of air is ~ 1 and the refractive index of the fiber's core glass is ~ 2.8, the amount of light reflected at an interface as a function of angle of incidence is plotted in Figure 30.

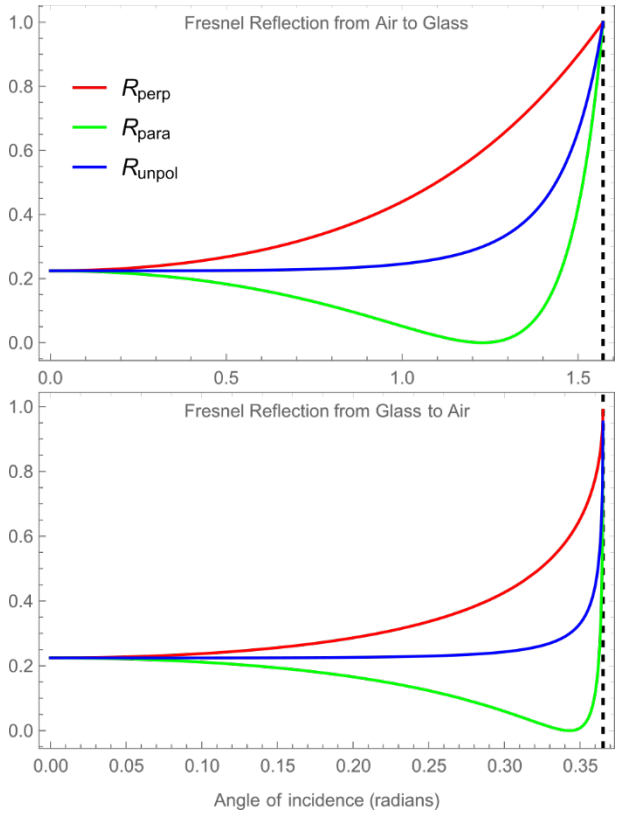

Figure 30: Fresnel reflectance for perpendicularly polarized (red), parallel polarized (green), and unpolarized (blue) light from air to glass (top) and glass to air (bottom) assuming $n_{air} = 1$ *and* $n_{glass} = 2.8$*. Dotted line represents an angle of* $90°$ *(top) and the critical angle where total-internal reflection occurs (bottom).*

It is usually a good approximation to assume that light will have normal incidence to the surface of the entrance and exit of the fiber ($\theta_1 = 0$). By examining the results shown in Figure 30, it is evident that the total loss (from air to glass entering the fiber plus the contribution of glass to air exiting the fiber) caused by Fresnel reflections is of a whopping ~44% because of the massive refractive index difference between air and glass.

A way to reduce the impact of these losses is by using antireflection coatings. We propose using the method and materials detailed in [150]. Starting with a $\lambda/4$ thick alternating films of YF_3 ($n_a \approx 1.41$) and ZnS ($n_b = 2.24$) placed on the input surface of the bundle would reduce the effect of Fresnel reflection

to less than 10% in the MWIR after proper optimization, as shown in Figure 31. Note that this was optimized for the central wavelength of (4μm) of the MWIR and shows great tolerance for a wide range of incidence angles.

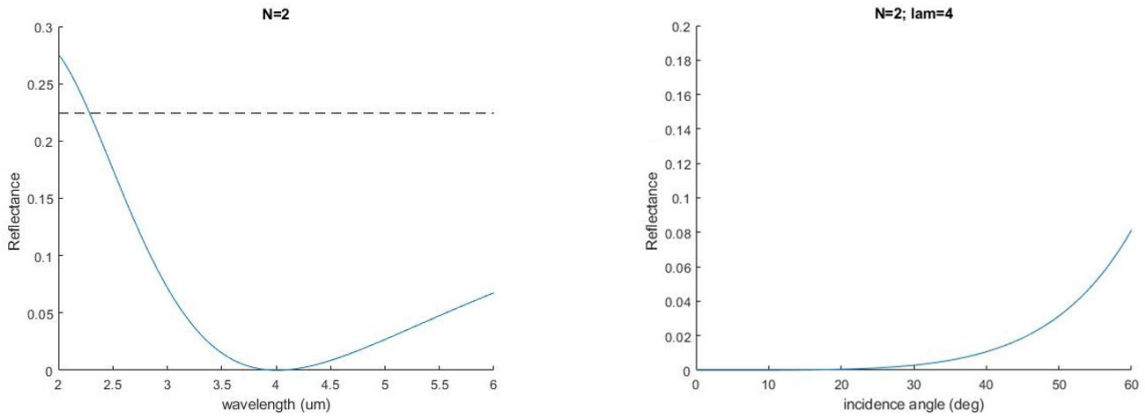

Figure 31: Antireflection coating for inhibiting Fresnel reflections at the air-glass interface of the bundle. N is the number of layers, and after optimization two layers (one of each material) are enough to lower the reflectance to <15% in the MWIR to where there is virtually no back-reflection (left) at a wavelength of 4μm for a wide range of angles (right). The black dashed horizontal line represented the Fresnel reflectance at normal incidence (left).

3.2.2 Material absorption and imaginary part of the refractive index

Aside from Fresnel reflections that can be corrected with antireflection coatings, there is still the problem of having absorption losses as light propagates through the fiber. Fortunately, the absorption caused by the core glass and its impurities can be neglected in the order of centimeters. Therefore what we care about the most is that the polymers we use have absorptions low enough to let at least 75% of the light pass through the fiber. The amount of light absorbed by the cladding is proportional to the amount of power outside of the fiber's core. For this reason, we analyzed the loss experience by a ChG-polymer fiber of three different core sizes. The first being our target 7μm diameter and the other two being 10.5μm and 14μm. With the FEM, we assumed that the core glass was lossless, specified a range of imaginary refractive indices, set the wavelength to 5μm, and results are shown in Figure 32.

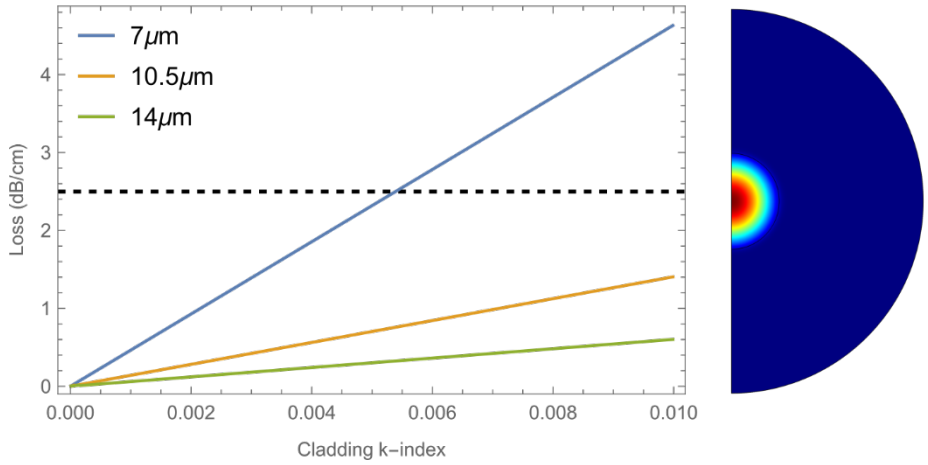

Figure 32: Attenuation in hybrid ChG-polymer fibers in dB/cm at $\lambda = 5\mu m$ as a function of the imaginary part of the cladding's refractive index (k-index) for three core diameters, $7\mu m$, $10.5\mu m$, and $14\mu m$. The horizontal dashed line represents where the absorption loss is 75% per centimeter.

For the calculation presented in Figure 32, the real part of the refractive index of the core was ~ 2.8 and the real part of the refractive index of the cladding was a very general ~ 1.67. The k-index is the imaginary part of the refractive index of the cladding, where $N = n - jK$ is the complex refractive index, which is related to the absorption coefficient of the material by

$$\alpha = \frac{4\pi K}{\lambda}, \tag{3.3}$$

where α is the absorption coefficient, K is the imaginary part of the refractive index, and λ is the wavelength of light. The absorption coefficient can be calculated by knowing the percent transmission through a sample of known thickness and using the $\frac{I}{I_0} = e^{-\alpha x}$ relation, where $\frac{I}{I_0}$ is the transmission and x is the distance light traveled (thickness of the sample) [132].

As expected, the fiber transmission decreased as the k-index (or material loss) increased, but it was worse for the 7μm core case. For the 7μm core case, 0.31% of the mode was in the cladding while 0.1%

and 0.04% was in the cladding for the $10.5\mu m$ and $14\mu m$ cases, respectively. In the previous section, we discussed different cladding polymers and presented some of their transmission spectra and dispersion curves in Figure 29. Based on results obtained, if our bundle were to have cores of $7\mu m$ in diameter, the k-index should be < 0.005. With our ATR-FTIR measurements and data for FEP reported in [56], we calculated the imaginary part of the refractive index using equation (3.3) for PEI, PES, and FEP for the MWIR and LWIR ($2.5 - 15\mu m$ wavelength range) and our results are shown in Figure 33.

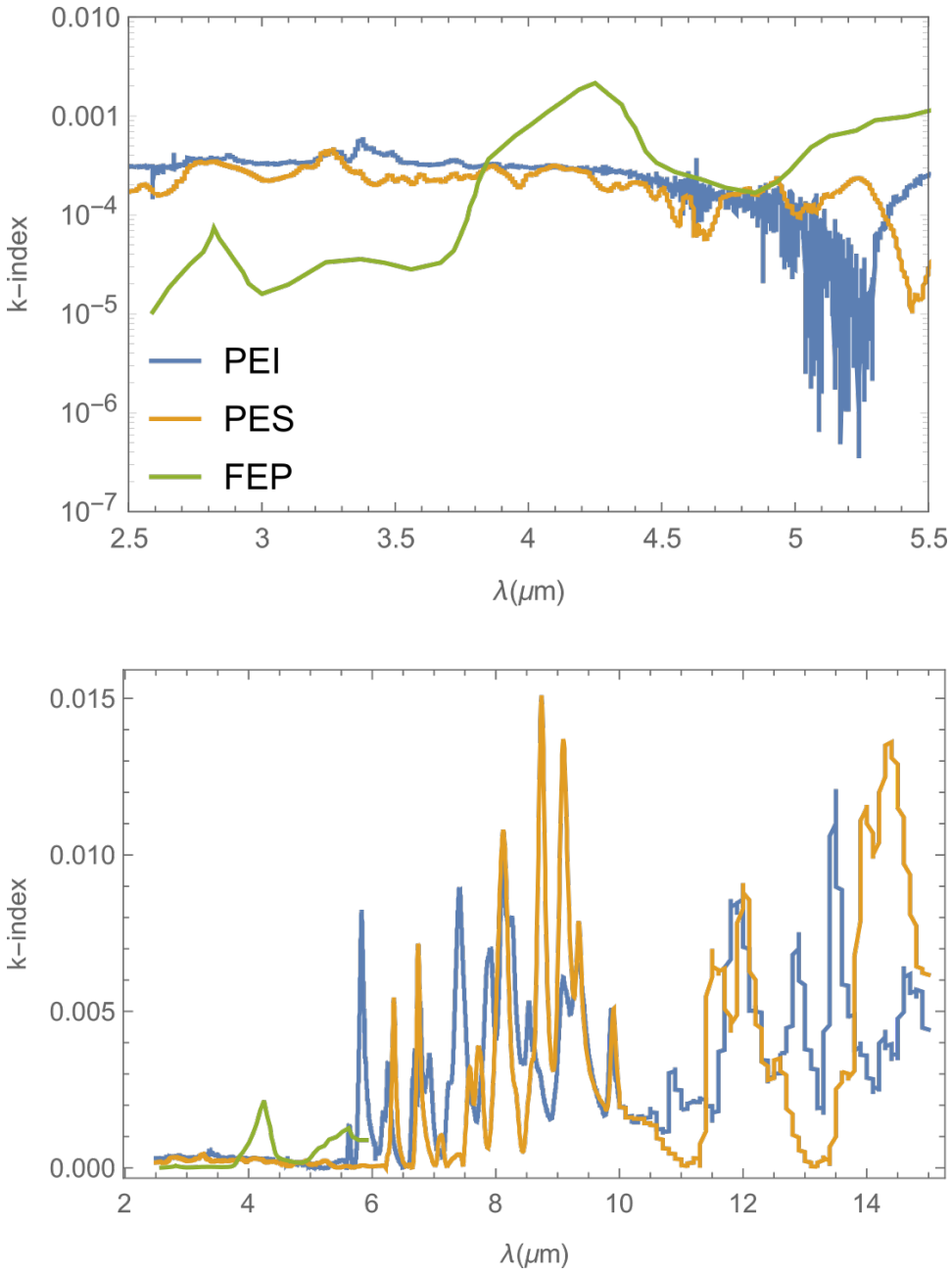

Figure 33: Imaginary part of the refractive index in the MWIR (top) and LWIR (bottom) of PEI, PES, and FEP calculated from the transmission data shown in Figure 29 (b) and (d). Note that beyond a wavelength of 10μm*, instrument accuracy begins to decrease. Also, the low k-index of PEI slightly after the* 5μm *wavelength is caused by the instrument error (mentioned in Figure 29's caption).*

Based on these results, the polymers presented in Table 2 and Figure 33 have a relatively low k-index in the MWIR and begins to spike up in the LWIR. PEI and PES have similar k-indices and FEP is from a different class of polymers, so its spectrum is quite different. From the calculated k-index and with 7μm cores, our fibers should be able to transmit about 94.8% (loss of 0.46dB) of the light over a length of 5cm at a wavelength of 4μm with a PEI cladding. As mentioned before, we did all of our fiber draws with PEI, so we expect our fibers to transmit light properly in the order of a few centimeters.

3.3 Glass and polymer rheology

As the name of this section implies, we will briefly dive into the rheology of glasses listed in Table 1 and PEI from Table 2. Rheology is the study of the deformation and flow of matter. When drawing optical fibers, it is easiest to draw similar materials that have been carefully designed or doped to have the necessary refractive index "step" at the core cladding boundary and make sure they can be drawn together at similar temperatures to avoid problems.

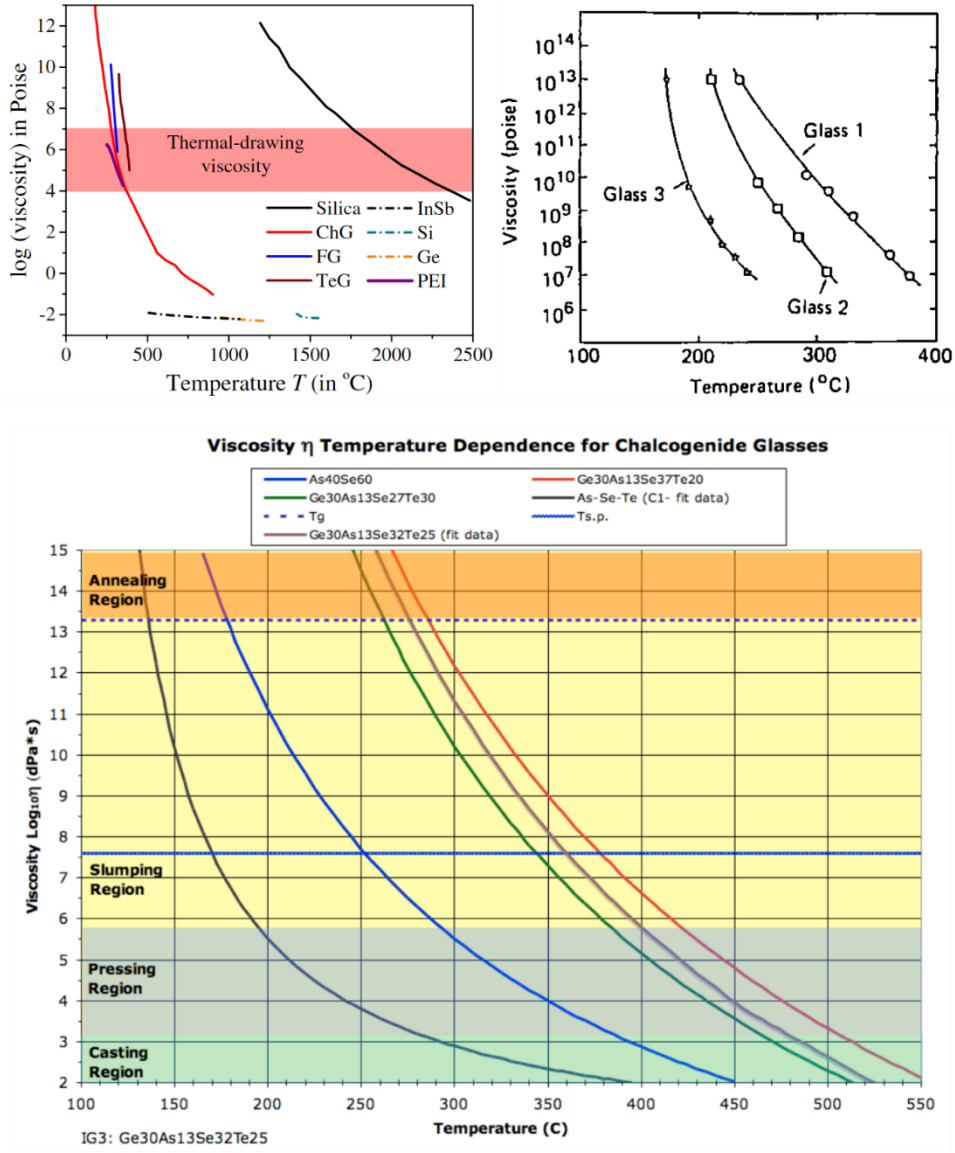

Figure 34: Rheology of all chalcogenide glasses presented in Table 1 with the addition of PEI in the top-left plot. When choosing materials to draw optical fibers, the material viscosity must match or at least be close by a few degrees, otherwise material flow problems will occur while drawing. Images from [124], [151], [152].

Multimaterial fibers such as those we are working with are made by using two different materials: one being a glass and the other a polymer. To ensure that they can be drawn together, it is necessary to look at their viscosity curves. The curves for IG3, IG6, As_2S_3 and PEI are shown in Figure 34, where it can be

seen that ChG and PEI are well thermally matched. To be specific, the ChG on the left-hand plot refers to As_2S_3 [153]. However, because IG6 can and has been drawn with As_2Se_3 [154], their viscosity curves must be similar. In the right-hand plot of Figure 34, the thermal differences between $As_{40}Se_{60}$ (IG6) and $Ge_{30}As_{13}Se_{32}Te_{25}$ (IG3) can be seen. The thermal properties between both glasses are so different that attempting to draw IG3 with PEI results in many problems during the fiber draw, despite PEI's outstanding thermal properties. More consequences of drawing thermally mismatched materials will be discussed in the next chapter.

Chapter 4: Infrared Fiber Bundle Fabrication

The process of making hybrid ChG-polymer fibers and how we drew them into a multi-core bundle will be detailed in this chapter. As stated throughout this work, our ultimate goal is to make small diameter cores of 7µm with a center-to-center spacing of 10µm.

The optical fiber fabrication process can be summarized into two simple steps: preform fabrication and fiber drawing. In the first step, all materials are appropriately processed and assembled. For infrared fibers, a common way of doing this is via the rod-in-tube method, stack-and-draw, and thin-film rolling [151], as seen in Figure 35. The following sections will detail how we fabricated our IR CFBs with the thin-film rolling method and used stack-and-draw to increase the core count. Also, a discussion on observations, problems, and results will be given.

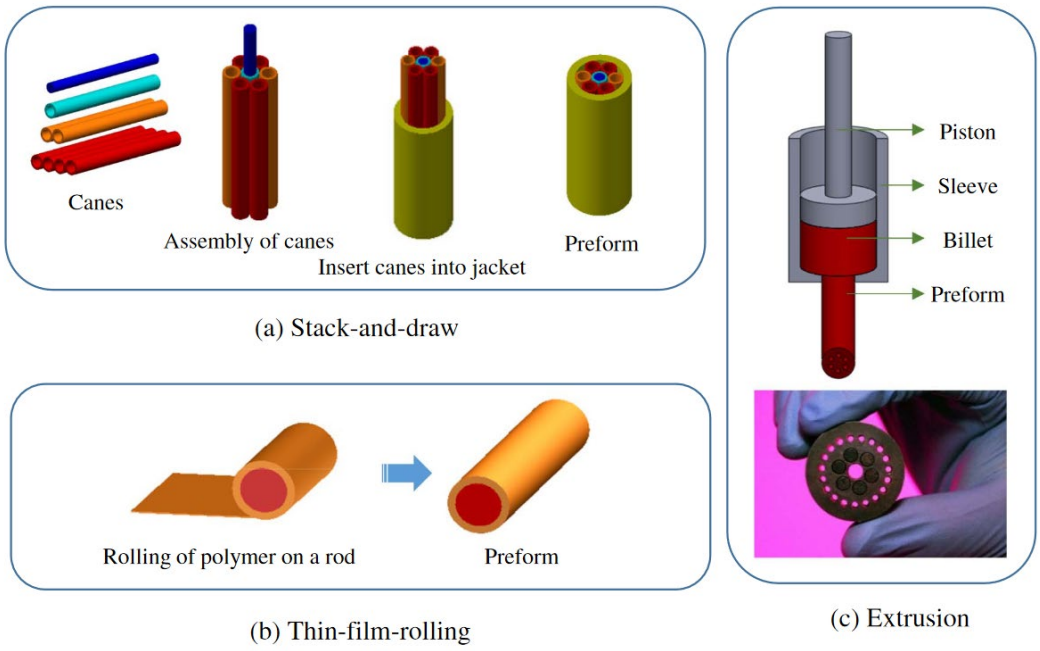

Figure 35: Diagram of infrared fiber fabrication methods. Because of the lower temperatures required to draw these glasses, a preform of different materials that are thermally compatible is best drawn with the methods detailed

in this figure. In our case, we used thin-film rolling (b) to make single fibers. Then stack-and-draw (a) to make the multi-cored bundle. Figure obtained from [151].

4.1 Preform fabrication

Of the four glasses listed in chapter 3, we decided to draw our fibers with IG3 and IG6 because of their commercial availability and compatibility with FEP and PEI, respectively. Two rods 150mm in length and 10mm in diameter were obtained of each glass, as shown in Figure 36. $Ge_{30}As_{13}Se_{32}Te_{25}$ (IG3) was obtained from Cybel-LLC and $As_{40}Se_{60}$ (IG6) was obtained from Vitron.

Figure 36: $Ge_{30}As_{13}Se_{32}Te_{25}$ (left) and $As_{40}Se_{60}$ (right) rods, both were 10mm in diameter and 150mm in length. The rod on the left was slightly longer by a few millimeters. Although $As_{40}Se_{60}$ rods were unpolished blanks, the glass surface became smooth when drawing.

Since the glasses are thermally matched to the polymer, testing polymer tubes is a good way to get the right temperatures for consolidating a preform. Blank PEI tubes were made by wrapping the film around a Teflon rod. Then, they were placed in a vacuum oven with a pressure of -0.1MPa at 285°C, 280°C, and 275°C. After consolidating both sides of the polymer tubes for ~12 minutes each, they were examined and are shown in Figure 37.

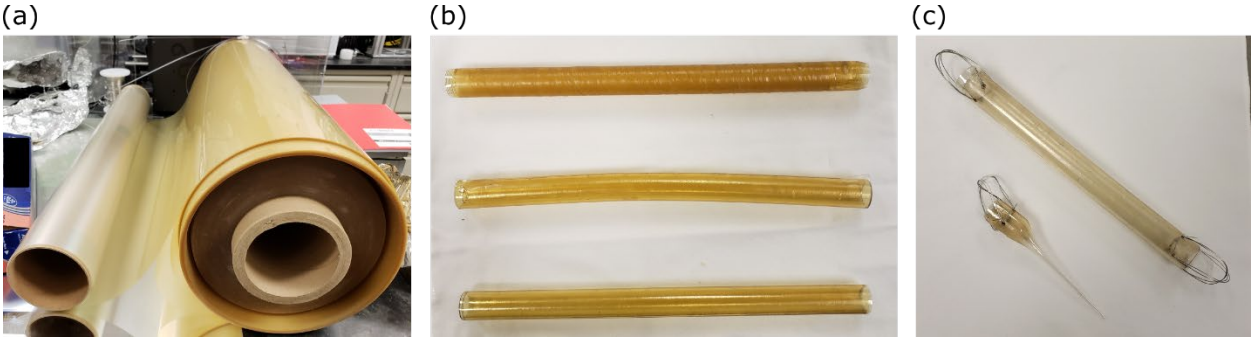

Figure 37: PES (left) and PEI (right) film rolls (a). Consolidated test wraps of PEI at $285°C$ *(top),* $280°C$ *(middle), and* $275°C$ *(bottom) (b). Pre- and post- draws of consolidated PES tubes for testing tower temperatures (c).*

From these results, it was evident that $285°C$ and $280°C$ temperatures were too high and caused the polymer to thermally degrade (Figure 37 (b), top and middle PEI tubes). $275°C$, on the other hand, was the right temperature and was used for the full preforms.

All preform materials, glasses and polymers, were first placed overnight in a vacuum oven with a pressure of -0.1MPa and a temperature of $125°C$ to get rid of any moisture that could hinder the performance of the fibers. Glass rods were tightly wrapped with the polymer thin-films until a preform with a 12mm outer diameter was obtained. Note that instead of using the planned FEP film on $Ge_{30}As_{13}Se_{32}Te_{25}$, we decided to use PEI because of difficulty we would have had controlling the flow of FEP if the incorrect temperature was used and because of the lack of an exhaust vent in case the polymer released dangerous fumes when drawn with our current fiber tower setup. Then, they were placed in the oven again at -0.1MPa for consolidation. A $275°C$ temperature was used with 12 to 15 minutes of "baking" per side. Soon after, the preforms were ready to be drawn into IR fibers. A finished preform of $As_{40}Se_{60}$-PEI is shown in Figure 38.

Figure 38: Finished $As_{40}Se_{60}$ fiber preform with pressure crack in the center before being taken to the benchtop fiber draw tower.

4.2 Fiber drawing

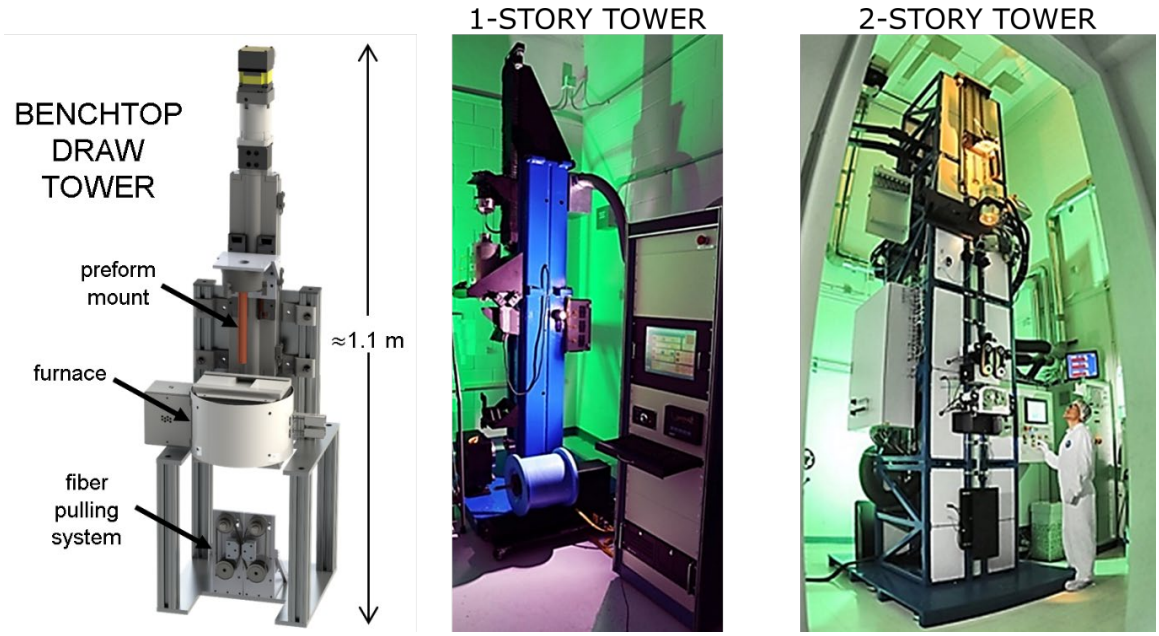

Figure 39: Optical fiber drawing towers at the University of Central Florida's College of Optics and Photonics (CREOL). 2-story tower is typically used for drawing silica fibers but may be adjusted for drawing soft glass fibers. Our bundle was drawn in the benchtop draw tower, which was made to draw soft glass fibers, because of its compact size and our fibers not being more than a few meters long. 1-story tower is like the benchtop tower but provides more control.

We had three options for drawing optical fibers, a 2-story, 1-story, and a tabletop tower, as seen in Figure 39. We decided to go with the tabletop tower since our fiber lengths were not more than a few meters and it was specifically made for drawing soft glasses, such as ChGs. After consolidating the preforms, the fiber tower was pre-heated while small holes were drilled in the upper part of the preform to hang it on the tower's furnace, similar to those seen in Figure 37 (c). When the temperature on the tower read $430°C$ for $As_{40}Se_{60}$ (and about $480 - 500°C$ for $Ge_{30}As_{13}Se_{32}Te_{25}$), the preform was placed in the holder and began to be drawn. The two zones used to control the draw speed are the preform mount (slowly lowers the preform) and the pulling system (slowly pulls the fiber). The mount was being moved down at about 2mm/min and the belts at the bottom were pulling the melting fiber at 200mm/minute. This factor of 100 ratio between the speeds ensures that the fiber coming out is about a factor of 10 smaller in diameter than the preform. Figure 40 shows the preform being inserted into the furnace and $As_{40}Se_{60}$ fiber coming out from the bottom of the drawing tower.

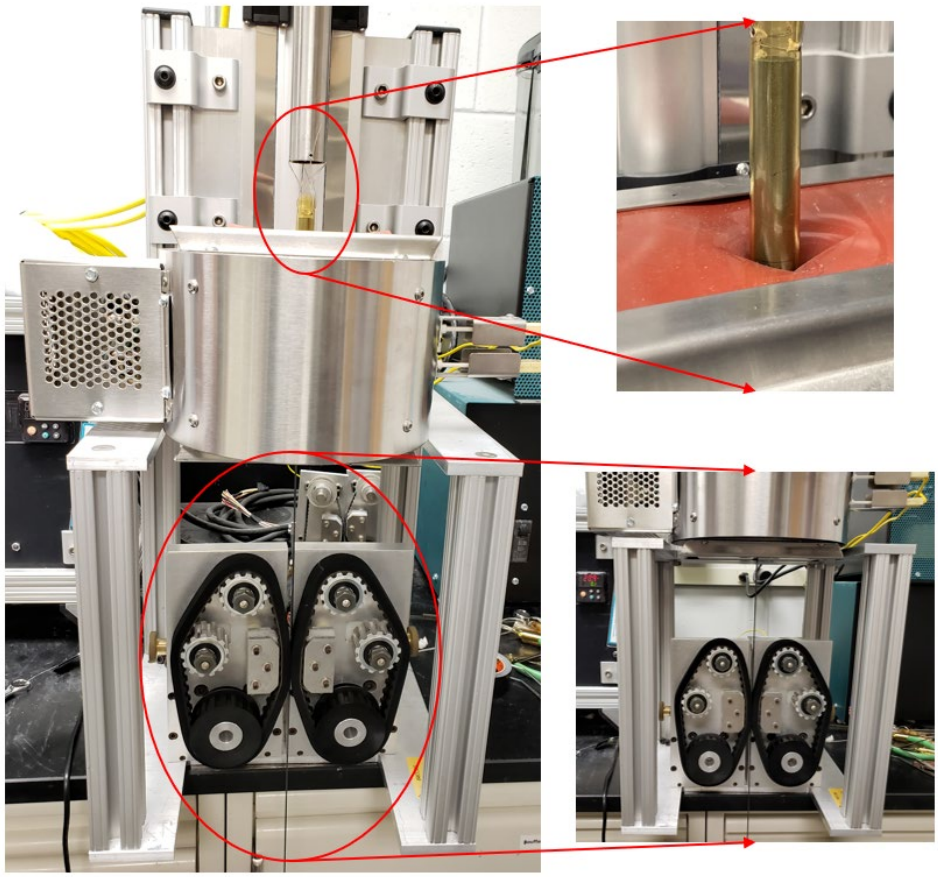

Figure 40: $As_{40}Se_{60}$-PEI fiber being drawn in the benchtop tower. The fiber is the "wire" coming out from the bottom (bottom-right) while the preform is being slowly pulled down at the top of the tower (top-right).

After the first draw, the dimensions of the larger fiber were measured with a scanning electron microscope, as shown in Figure 41. Then, they were stacked inside of another polymer tube and drawn down into canes of 60 and 81 cores for $Ge_{30}As_{13}Se_{32}Te_{25}$ and $As_{40}Se_{60}$, respectively. That was then drawn down again in the fiber tower with the same temperatures, and another stacking was made to increase the number of cores in the final bundle.

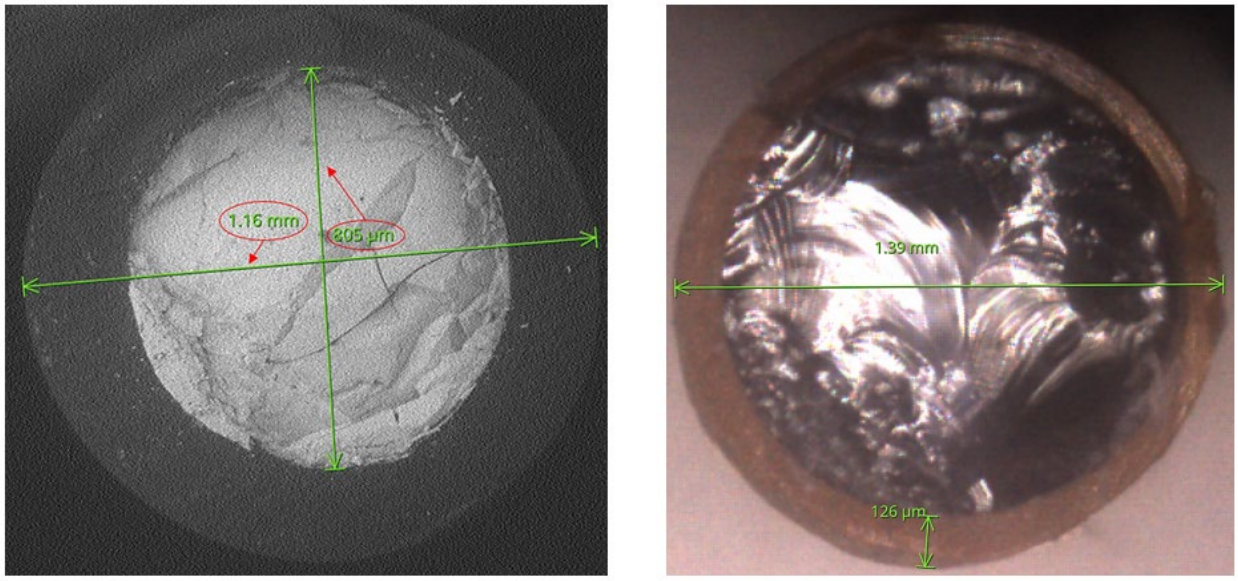

Figure 41: Scanning electron microscope images of the larger fibers that result from drawing the cross-sectional area of the preforms down by an order of magnitude. $Ge_{30}As_{13}Se_{32}Te_{25}$-PEI (left) and $As_{40}Se_{60}$-PEI (right). Note that imperfections on the surface are caused by the cleave to insert fibers into the microscope.

After the first draw with $Ge_{30}As_{13}Se_{32}Te_{25}$ and PEI, the end result was a bundle of about ~1105 cores and several meters in length, as seen in Figure 42. This did not occur without many difficulties, however. Some of which were thermal, mechanical, and structural in the material side of things.

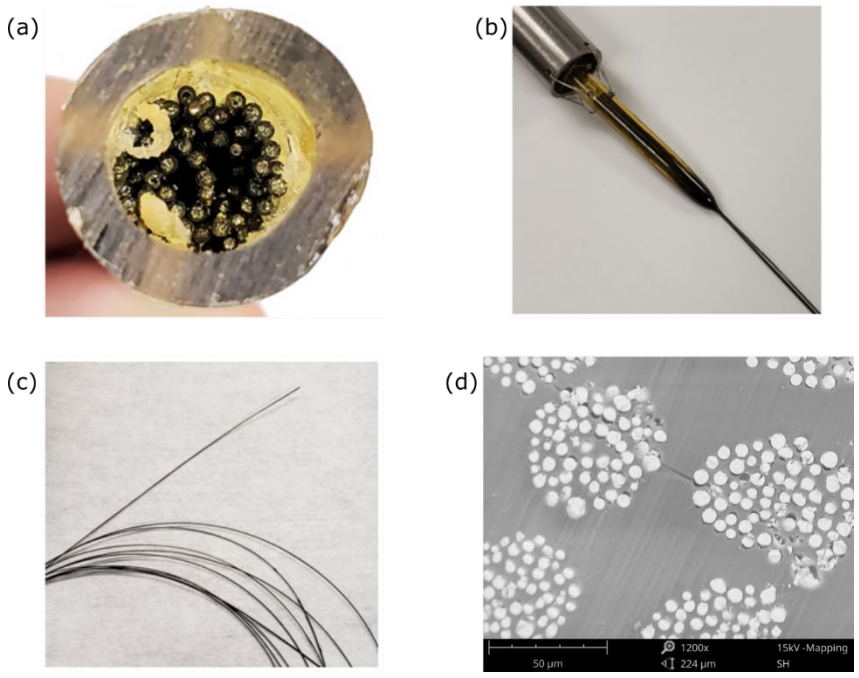

Figure 42: Stack-and-draw of $Ge_{30}As_{13}Se_{32}Te_{25}$ fiber bundle (a) and (b). Finalized preliminary fiber bundle of ~1105 cores (c). Scanning electron microscope image of fiber bundle surface (d). Note that issues seen in the microscope image occurred because of the rough cleaving method we used. Despite thermal matching issues, cores came out to be more or less the right diameter of $7\mu m$ but with a disordered center-to-center and cluster spacing.

Fiber draws with $As_{40}Se_{60}$ have been nothing but successful. Both, the glass and PEI, were correctly thermally matched and flowed well together. Figure 43 shows a cane of 81 cores being drawn in the tower. Next, the 81-core fibers were stacked and drawn again to make up a bundle of ~7000 cores.

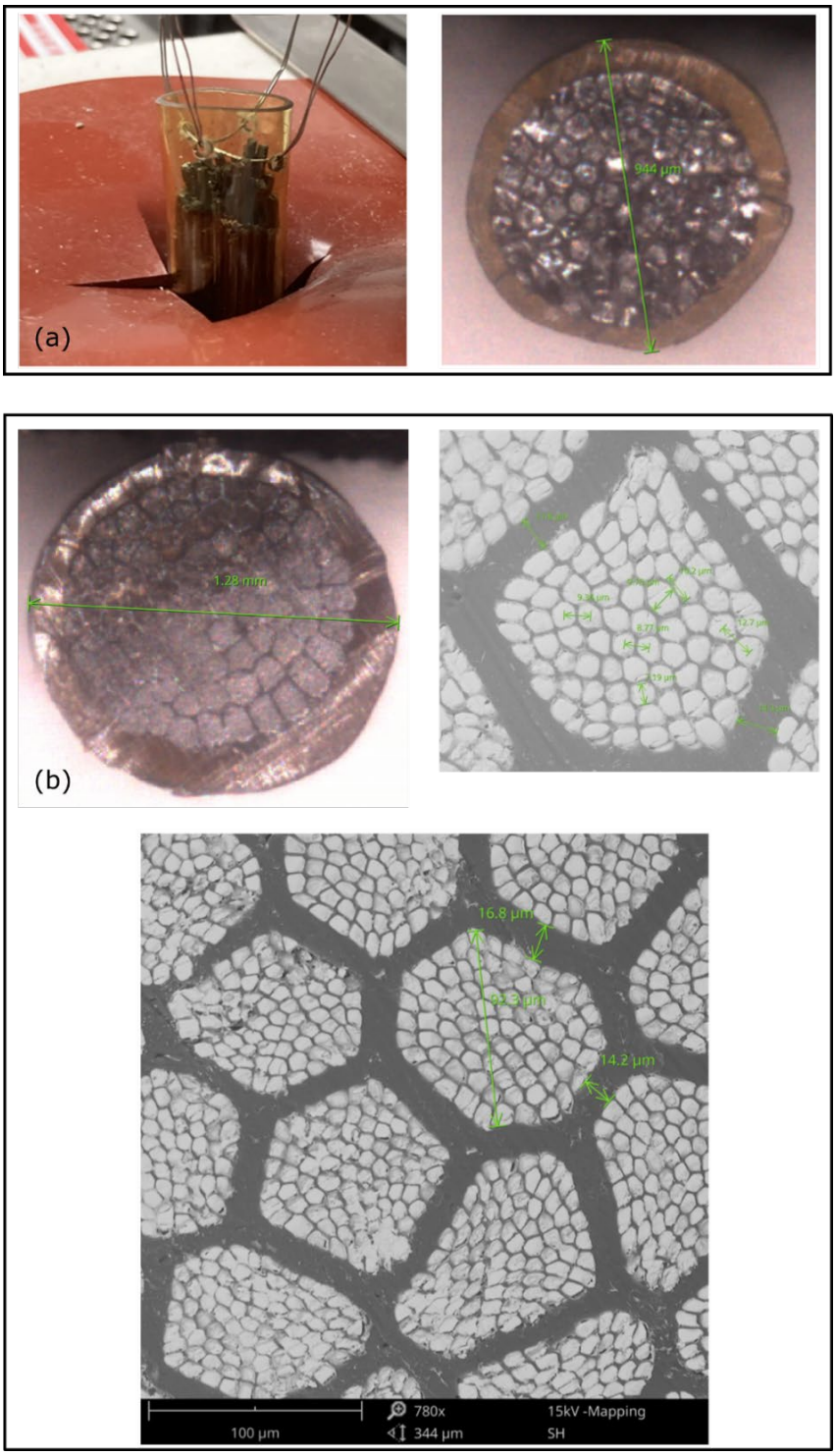

Figure 43: $As_{40}Se_{60}$ fiber bundle of 81 cores being drawn in the table-top tower (a). Resulting in a ~944µm outer diameter 81-core fiber bundle that was stacked with itself again to make a bundle of ~7000 cores (b). The finalized

bundle was ~1.28mm in outer diameter and core sizes ranging from $\sim 7 - 10\mu m$ *with center-to-center spacings of* $\sim 9 - 13\mu m$ *depending on core size.*

4.3 Discussion of fiber draw issues and results

Starting with the first hybrid material combination, $Ge_{30}As_{13}Se_{32}Te_{25}$ with PEI, the fiber draw end result came out a lot better than we expected. However, many issues occurred during the preform fabrication and fiber draw. First of all, the rods had millimeter-sized imperfections, grooves, and dents possibly caused by germanium content of the glass (but currently not known why). The way the glass was made or the glass itself was very brittle and cracked while it was slowly being pulled down the fiber tower into the furnace, as shown in Figure 44. Also, the glass had a much higher working temperature than PEI, which resulted in PEI drawing by itself without glass (Figure 44 (d)). PEI was pushed to its thermal limits and at some points began to thermally degrade too. The cracks and dents on the glass did not go away during the drawing because the glass flowed less than the polymer due to the drawing temperature (we had to find a "safe" spot to not thermally degrade the polymer). This resulted in a bundle with noticeable nonuniformities center-to-center spacing (Figure 42 (d)).

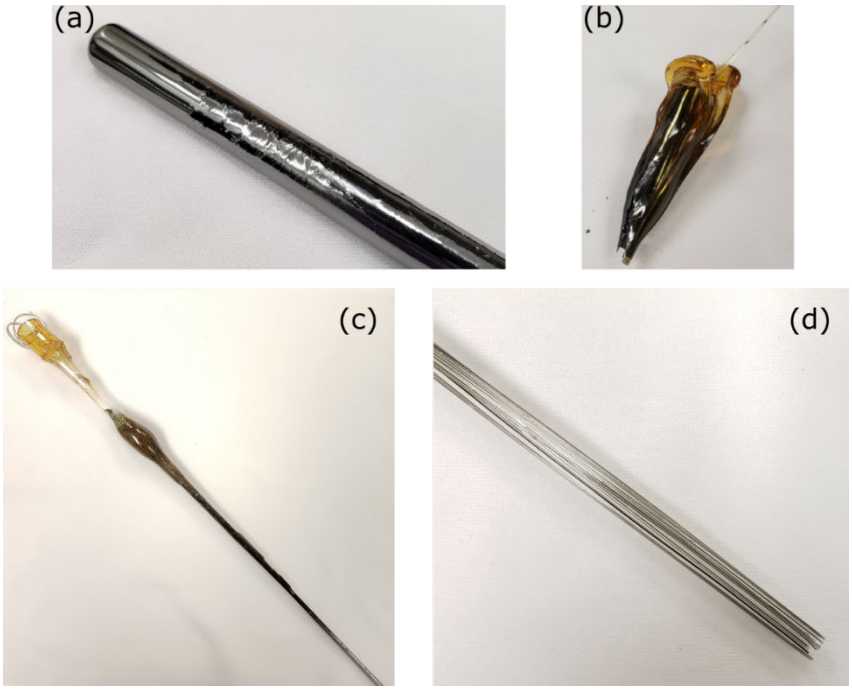

Figure 44: Issues that occurred during the $Ge_{30}As_{13}Se_{32}Te_{25}$ fiber draw. Significant rod surface roughness (a), preform breaking while being pulled into the furnace (b), uneven heat distribution and material-related thermal mismatching caused polymer to bunch up (c) draw alone without glass (d).

With $As_{40}Se_{60}$ and PEI on the other hand, not that many problems occurred. The rods received from the manufacturer were unpolished blanks. Interestingly, it was not necessary to polish them because the surface roughness was very small and uniform throughout. This draw was well within the working range of PEI and the glass, so the temperature alone was enough to soften the small imperfections that were not visible with the naked eye. An issue that occurred unexpectedly (as with any issues, really) was that the rod cracked while being wrapped by PEI and it cracked while hanging from the tower. The cracks were not as severe as with the previous glass, but we believe that the cracks were due to sudden temperature changes from $125°C$ to room temperature and back to $> 300°C$ in the tower's furnace and the glass being brittle because of how it was manufactured.

Fiber draws with both glasses went well all things considered. Despite the thermal mismatch of $Ge_{30}As_{13}Se_{32}Te_{25}$ with PEI, a bundle of a few meters with ~1105 cores was made. The cores had diameters around $\sim 7\mu m$, but thermal issues mostly affected their center-to-center spacing which made them be much further apart than expected and without much order. Also, there was significant surface roughness along the length of the bundle because of the deep grooves that the glass rod had and could not be softened enough during the draw because it would have thermally degraded PEI due to the high temperatures needed. Nevertheless, drawing two thermally mismatched materials was a lesson that should be shared and serves as a warning for future reference. In the case of $As_{40}Se_{60}$, a bundle of around ~7000 cores with an outer diameter of 1.28mm has been drawn. Unlike the thermally mismatched bundle, core sizes ranged from ~7-10μm with center-to-center spacings of ~9-13μm depending on core size. There was no noticeable surface roughness along the length of the bundle and although there are blind spots of PEI in between 81-core clusters, it is expected to not hinder imaging performance in the grand scheme of things.

Chapter 5: Conclusions and Future Work

Wide-angle imagers that operate in the MWIR and LWIR spectrum are essential in defense, agricultural, and space applications to name a few. Most direct uses, however, are military-related such as target acquisition, aerial navigation, and surveillance. During the DARPA SCENICC program, J. Ford, et al., were the first to demonstrate that fiber bundles could be tapered, curved, and coupled to a fast monocentric lens to make a compact wide-angle imager. This discovery proved to be a more practical and provides a volumetric imaging efficiency 100x higher than that of conventional bulk optics with a 100x smaller volume (while resolution is held constant).

Ford's work was best suited for the visible and NIR spectrum. This work aims to be the first, to our knowledge, to try to extend the curved coherent fiber bundle concept to the infrared by having $> 1000 \times 1000$ or $>$ million cores to couple into high-resolution image sensors. For this reason, we have developed hybrid fiber bundles, with cores of $7\mu m$ in diameter with a center-to-center spacing of $10\mu m$, for the MWIR (with potential to be used in the LWIR) that provide tight step-index confinement of light by taking advantage of the core glass's high refractive index and polymer cladding's lower refractive index. The high index contrast of the core and cladding yields a large fiber numerical aperture to optimize coupling into the bundle with a fast lens, minimizes the absorption losses caused by the cladding polymer, and inhibits crosstalk while making it possible to easily reduce it further by introducing a core-size mismatch.

After analyzing the possible materials that could be used, chalcogenide glasses proved to be the best for the core. Depending on how they are fabricated, impurities can be reduced to have a uniform transmission in the desired wavelength range. Many of these glasses can effectively transmit light from the NIR to the LWIR, have refractive indices >2 in the IR, and possess transition temperatures close to those of robust thermoplastic polymers. These properties and their suitable rheology makes it ideal for them to be drawn into hybrid infrared fibers. Of course, not all chalcogenide glasses may be drawn into fibers. We

narrowed down our choices to four glasses and decided to try to make fibers with $Ge_{30}As_{13}Se_{32}Te_{25}$ and As_2Se_3 glass, both commercially available. PEI was chosen for the cladding due to it being previously used for making IR fibers, it has lower losses, is very robust, and has suitable thermal properties. Note that it was thermally matched to As_2Se_3 and not to $Ge_{30}As_{13}Se_{32}Te_{25}$, hence why problems during the drawing process occurred with the latter glass.

Preforms consisted of a central glass rod of 10mm diameter and 150mm length for the core with thin-film polymer wraps until an outer diameter of 12mm was achieved. After thermally consolidating the preforms in a vacuum oven, they were taken to the table-top tower and drawn into fibers. Those fibers were then stacked together and drawn again. The process was repeated again and again until there was not enough fiber to stack or it was considered "complete" for characterization and testing.

While using $Ge_{30}As_{13}Se_{32}Te_{25}$ glass, the major difficulty that we had was its surface roughness, its brittleness, and its thermal mismatch to PEI. We decided not to use FEP because of potentially dangerous fume problems it could have caused with our current fiber drawing setup and its flow being different when drawn due to it being semi-crystalline. Some of the issues we encountered were deep glass rod roughness that persisted when drawn into fiber, preform cracking while hanging in the tower, polymer thermal degradation (pushing to its upper temperature limits), and uneven heat distribution while drawing multi-core fiber cane which gave uneven finalized core diameters and center-to-center spacing. Interestingly, there were instances where not enough glass flowed through the polymer and it resulted in empty holes in the cladding where glass should have been.

Taking the lessons learned from the previously mentioned draw, As_2Se_3 was drawn with PEI. Both materials had been successfully drawn before and are thermally compatible. All fibers that came out from this material combination were a success. Fibers were smooth, uniform in size, and minor problems that occurred were caused by the glass rod breaking with temperature shifts (oven to room to drawing

temperature). Most broken pieces of preform were salvaged while drawing the fiber by pulling the materials slowly and the temperatures being able to soften the glass enough to flow well and reduce surface roughness and imperfections. In the end, a bundle of about ~7000 cores, with an outer diameter of 1.28mm has been drawn. Unlike the thermally mismatched bundle, core sizes ranged from ~7-10μm with center-to-center spacings of ~9-13μm depending on core size. Cores were tightly packed and were uniform in shape for the most part (slight deformations occurred towards the edge of the 81-core clusters).

The As_2Se_3-PEI bundle is ready to be optically characterized and it is expected that it will perform well. Some blind spots (spaces between 81-core clusters) might slightly hinder performance but might be negligible in the grand scheme of things. Unfortunately, the pandemic that struck the world in 2020 put the project on pause for about seven months and set us back. For this unfortunate reason, a full-scale bundle of hundreds of thousands of cores was not included in this text. Therefore, the next steps are to be able to carefully cleave the bundle with specialty tools because of how robust it is and to ensure that the core glass is uniformly cut and not broken in the input or output side. Then, it will be coupled with fast IR lenses to be able to transmit small images through it and test its performance. Crosstalk will be measured by exciting a core with a laser and seeing how much of the light leaks into other nearby cores by looking at intensity profiles. If all is successful, the next step is to scale the current bundle to the megapixel range (hundreds of thousands of cores) by consolidating 5cm-long pieces together to make a thicker bundle or draw another new bundle but with clusters of more cores to increase count and uniformity. Finally, the end goal will be to taper, cut a curved input side, and polish the final bundle to be able to couple it to fast wide-angle imaging lenses and test its performance in comparison to state-of-the-art conventional bulk optics in the IR.

Appendix

A.1

As mentioned in section 2.3, CMT is an approximation and under certain circumstances some assumptions or methods must be carefully revised. Although other exact analytical methods and versions of CMT have been discussed, this subsection will look at the coupling between HE_{11} modes following what was detailed in [88]. Looking at strongly-guiding optical fibers with $n_1 = n_2 = 2.8$ and $n_0 = 1.67$ (as in the case of the slab waveguides) we concentrate on the like-mode coupling as detailed in [88] and using the same notation as in the fiber-mode derivation section:

$$E_x = CJ_0\left(\frac{ur}{a}\right)\cos(\phi), \tag{2.84}$$

$$E_y = -CJ_0\left(\frac{ur}{a}\right)\sin(\phi), \tag{2.85}$$

and

$$E_z = j\frac{u}{\beta a}CJ_1\left(\frac{ur}{a}\right)\cos(\theta + \phi), \tag{2.86}$$

In the core region $0 \leq r \leq a$ and

$$E_x = C\frac{J_0(u)}{K_0(w)}K_0\left(\frac{wr}{a}\right)\cos(\phi), \tag{2.87}$$

$$E_y = -C\frac{J_0(u)}{K_0(w)}K_0\left(\frac{wr}{a}\right)\sin(\phi), \tag{2.88}$$

And

$$E_z = j\frac{u}{\beta a}C\frac{J_1(u)}{K_1(w)}K_1\left(\frac{wr}{a}\right)\cos(\theta + \phi), \tag{2.89}$$

In the cladding region $r > a$. Information on the magnetic fields may be found in [88], but are not needed to solve the numerator of κ. The constant C is related to power, P, by:

$$|C| = \frac{w}{aVJ_1(u)}\sqrt{\frac{2P\sqrt{\mu_0/\epsilon_0}}{\pi n_1}}. \tag{2.90}$$

Then, the denominator of κ is normalized by:

$$\int_{A_\infty}\left(\overrightarrow{E_1}^* \times \overrightarrow{H_1} + \overrightarrow{E_1} \times \overrightarrow{H_1}^*\right)\cdot \hat{n_z} dA = 4P_1. \tag{2.91}$$

Therefore, the coupling coefficient for optical fibers is given by:

$$\kappa = \frac{\omega\epsilon_o(n_1^2 - n_0^2)\int_{A_{co,1}} \overrightarrow{E_1}^* \cdot \overrightarrow{E_2} dA}{4}, \tag{2.92}$$

where P is assumed to be unity. The numerator of κ is found by taking the dot product between the mode of core 1 and the mode of core 2. Since the integral is over core 1 only, the numerator may be expressed as [88]:

$$\omega\epsilon_0(n_1^2 - n_0^2)\int_{A_{co,1}} |C|^2 \frac{J_0(u)}{K_0(w)} J_0\left(\frac{ur}{a}\right) K_0\left(\frac{wR}{a}\right) dA, \tag{2.93}$$

where, when $D \gg r$ holds, $R = \sqrt{D^2 + r^2 - 2D\cos(\theta)}$ is a "coordinate system" having the origin at the center of core 2 (not to be confused with the actual coordinate system's origin, $r = 0$, located at the center of core 1) with D being the center-to-center spacing between cores.

Using equation (2.92), to compute the coupling coefficient and get the coupling lengths from (2.80) gave some interesting results. The imaging bundle that we are proposing consists of cores with $2a = 7\mu m$ and a center-to-center spacing of $10\mu m$. First, varying the center-to-center spacing yields the results listed in Table 3.

Core center-to-center spacing (μm)	L_c from CMT (m)	L_c from FEM (m)
8	0.027	0.015
10	7.724	4.122
12	2207.205	1105.549

Table 3

Then, the center-to-center spacing was held constant (10μm) but the relative refractive index difference between the core and the cladding was reduced from unity until close agreement was found, as shown in Table 4.

Relative index difference $(n_{co} - n_{clad})$	L_c from CMT (m)	L_c from FEM (m)
1	4.589	2.612
0.8	1.734	1.139
0.6	0.533	0.405
0.4	0.120	0.106
0.2	0.0152	0.0156

Table 4

As previously mentioned, L_c was used as the method of comparing results obtained via CMT and the FEM. Concentrating Table 4, results show decreasing agreement as the index contrast increases. Interestingly, somewhere after an index contrast of 0.6 is where issues start to occur until reaching unity; where it is evident that the CMT presented here is off by almost a factor of two.

Based on the results shown here, the scalar CMT cannot be used to compute the correct coupling lengths between our fibers. Although the full-vector CMT presented in [97] is more robust, it is strongly recommended to use numerical methods or the analytical methods mentioned in section 2.3.2, when $n_{co} - n_{clad} \geq 0.5$. Especially since CMT for optical fibers is better suited for lower V-numbers that primarily support the fundamental HE_{11} mode.

References

[1] “Herschel and the Puzzle of Infrared,” American Scientist, Feb. 06, 2017. https://www.americanscientist.org/article/herschel-and-the-puzzle-of-infrared (accessed Nov. 14, 2020).

[2] E. C. Sutton, Observational astronomy: techniques and instrumentation. Cambridge University Press, 2011.

[3] M. Rowan-Robinson, Night Vision: Exploring the Infrared Universe. Cambridge: Cambridge University Press, 2013.

[4] “Kalman Tihanyi (1897 - 1947) - Television Pioneer.” http://www.ctie.monash.edu.au/hargrave/tihanyi.html (accessed Nov. 09, 2020).

[5] J. Byrnes, Unexploded Ordnance Detection and Mitigation. Springer Science & Business Media, 2008.

[6] M. Z. Tidrow and W. R. Dyer, “Infrared sensors for ballistic missile defense,” Infrared Phys. Technol., vol. 42, no. 3, pp. 333–336, Jun. 2001, doi: 10.1016/S1350-4495(01)00092-5.

[7] F. Parker, Applications of Infrared Spectroscopy in Biochemistry, Biology, and Medicine. Springer Science & Business Media, 2012.

[8] E. F. J. Ring and K. Ammer, “Infrared thermal imaging in medicine,” Physiol. Meas., vol. 33, no. 3, pp. R33–R46, Feb. 2012, doi: 10.1088/0967-3334/33/3/R33.

[9] C. A. T. dos Santos, M. Lopo, R. N. M. J. Páscoa, and J. A. Lopes, “A Review on the Applications of Portable Near-Infrared Spectrometers in the Agro-Food Industry,” Appl. Spectrosc., vol. 67, no. 11, pp. 1215–1233, Nov. 2013.

[10] “Infrared radiation.” http://eilv.cie.co.at/term/580 (accessed Nov. 13, 2020).

[11] L. Werner and J. Hartmann, “Calibration and interpolation of the spectral responsivity of silicon photodiode-based detectors,” Sens. Actuators Phys., vol. 156, no. 1, pp. 185–190, Nov. 2009, doi: 10.1016/j.sna.2009.05.002.

[12] J. Vincent, “OnePlus 8 Pro has an accidental X-ray vision filter that sees through plastic and clothes,” The Verge, May 15, 2020. https://www.theverge.com/2020/5/15/21259723/oneplus-8-pro-x-ray-vision-infrared-filter-see-through-plastic (accessed Jan. 27, 2021).

[13] G. Keiser, Optical Fiber Communications. McGraw-Hill Education, 2010.

[14] G. A. Rao and S. P. Mahulikar, “Effect of atmospheric transmission and radiance on aircraft infared signatures,” J. Aircr., vol. 42, no. 4, pp. 1046–1054, 2005.

[15] J. M. Lloyd, Thermal Imaging Systems. Springer Science & Business Media, 2013.

[16] M. T. Eismann, “Imaging System Design and Analysis,” pp. 243–313, Apr. 2012, doi: 10.1117/3.899758.ch6.

[17] H. Kim, J. Jung, and J. Paik, “Fisheye lens camera based surveillance system for wide field of view monitoring,” Optik, vol. 127, no. 14, pp. 5636–5646, Jul. 2016, doi: 10.1016/j.ijleo.2016.03.069.

[18] Y. Kuniyoshi, N. Kita, K. Sugimoto, S. Nakamura, and T. Suehiro, “A foveated wide angle lens for active vision,” in Proceedings of 1995 IEEE International Conference on Robotics and Automation, May 1995, vol. 3, pp. 2982–2988 vol.3, doi: 10.1109/ROBOT.1995.525707.

[19] J. J. Kumler and M. L. Bauer, “Fish-eye lens designs and their relative performance,” in Current Developments in Lens Design and Optical Systems Engineering, Oct. 2000, vol. 4093, pp. 360–369, doi: 10.1117/12.405226.

[20] D. H. Cha, H.-J. Kim, Y. Hwang, J. C. Jeong, and J.-H. Kim, “Fabrication of molded chalcogenide-glass lens for thermal imaging applications,” Appl. Opt., vol. 51, no. 23, pp. 5649–5656, Aug. 2012, doi: 10.1364/AO.51.005649.

[21] M. O. Lidwell, “Achromatism Of Lenses For Thermal IR,” in Optical Systems Engineering IV, Jan. 1985, vol. 0518, pp. 73–80, doi: 10.1117/12.945181.

[22] S. Bayya et al., “New multiband IR imaging optics,” in Infrared Technology and Applications XXXIX, Jun. 2013, vol. 8704, p. 870428, doi: 10.1117/12.2016332.

[23] T. S. Kleine et al., “100th Anniversary of Macromolecular Science Viewpoint: High Refractive Index Polymers from Elemental Sulfur for Infrared Thermal Imaging and Optics,” ACS Macro Lett., vol. 9, no. 2, pp. 245–259, Feb. 2020, doi: 10.1021/acsmacrolett.9b00948.

[24] W. T. Welford, Aberrations of Optical Systems. CRC Press, 1986.

[25] M. J. Riedl, Optical Design Fundamentals for Infrared Systems. SPIE Press, 2001.

[26] N. Mansurov, “What is Field Curvature?,” Photography Life, Jan. 17, 2013. https://photographylife.com/what-is-field-curvature (accessed Nov. 13, 2020).

[27] T.-Y. Lim, Y.-S. Kim, and S.-C. Park, “Achromatic and Athermal Design of an Optical System with Corrected Petzval Curvature on a Three-dimensional Glass Chart,” Curr. Opt. Photonics, vol. 1, no. 4, pp. 378–388, Aug. 2017.

[28] R. Kingslake, A History of the Photographic Lens. Academic Press, 1989.

[29] Z. Ma, C. Lopez-Zelaya, and C. K. Renshaw, “Low Volume Imaging with Metasurfaces,” in 2019 IEEE Research and Applications of Photonics in Defense Conference (RAPID), Aug. 2019, pp. 1–4, doi: 10.1109/RAPID.2019.8864314.

[30] Z. Ma, K.-H. Shih, C. Lopez-Zelaya, C. K. Renshaw, and C. K. Renshaw, “Volumetric imaging efficiency: the fundamental limit to compactness of imaging systems,” Opt. Express, vol. 29, no. 3, pp. 3173–3192, Feb. 2021, doi: 10.1364/OE.415016.

[31] S.-B. Rim, P. B. Catrysse, R. Dinyari, K. Huang, and P. Peumans, “The optical advantages of curved focal plane arrays,” Opt. Express, vol. 16, no. 7, pp. 4965–4971, 2008.

[32] J. E. Ford, I. Agurok, and I. Stamenov, “Monocentric lens designs and associated imaging systems having wide field of view and high resolution,” US9860443B2, Jan. 02, 2018.

[33] F. Mrozek, M. Yu, and D. J. Henry, “Wide field of view monocentric lens system for infrared aerial reconnaissance camera systems,” US9329365B2, May 03, 2016.

[34] “Soldier Centric Imaging via Computational Cameras.” https://www.darpa.mil/program/soldier-centric-imaging-via-computational-cameras (accessed Jan. 28, 2021).

[35] “Advanced Wide FOV Architectures for Image Reconstruction and Exploitation.” https://www.darpa.mil/program/advanced-wide-fov-architectures-for-image-reconstruction-and-exploitation (accessed Jan. 28, 2021).

[36] “Extending Field of View in Advanced Imaging Systems.” https://www.darpa.mil/news-events/2019-08-09 (accessed Jan. 28, 2021).

[37] “Hemispherical Array Detectors for Imaging (HARDI) - Federal Grant.” https://www.federalgrants.com/Hemispherical-Array-Detectors-for-Imaging-HARDI-8352.html (accessed Jan. 28, 2021).

[38] Z. Gan, Y. Cao, R. A. Evans, and M. Gu, “Three-dimensional deep sub-diffraction optical beam lithography with 9 nm feature size,” Nat. Commun., vol. 4, no. 1, Art. no. 1, Jun. 2013, doi: 10.1038/ncomms3061.

[39] H.-C. Jin, J. R. Abelson, M. K. Erhardt, and R. G. Nuzzo, “Soft lithographic fabrication of an image sensor array on a curved substrate,” J. Vac. Sci. Technol. B Microelectron. Nanometer Struct. Process. Meas. Phenom., vol. 22, no. 5, pp. 2548–2551, Sep. 2004, doi: 10.1116/1.1795249.

[40] T. Wu, S. S. Hamann, A. Ceballos, O. Solgaard, and R. T. Howe, “Design and fabrication of curved silicon image planes for miniature monocentric imagers,” in 2015 Transducers - 2015 18th International Conference on Solid-State Sensors, Actuators and Microsystems (TRANSDUCERS), Jun. 2015, pp. 2073–2076, doi: 10.1109/TRANSDUCERS.2015.7181365.

[41] I. Jung, G. Shin, V. Malyarchuk, J. S. Ha, and J. A. Rogers, “Paraboloid electronic eye cameras using deformable arrays of photodetectors in hexagonal mesh layouts,” Appl. Phys. Lett., vol. 96, no. 2, p. 021110, Jan. 2010, doi: 10.1063/1.3290244.

[42] B. Guenter et al., “Highly curved image sensors: a practical approach for improved optical performance,” Opt. Express, vol. 25, no. 12, pp. 13010–13023, Jun. 2017, doi: 10.1364/OE.25.013010.

[43] J. E. Ford et al., “Fiber-coupled monocentric lens imaging,” in Imaging and Applied Optics (2013), paper CW4C.2, Jun. 2013, p. CW4C.2, doi: 10.1364/COSI.2013.CW4C.2.

[44] S. J. Olivas et al., “Image processing for cameras with fiber bundle image relay,” Appl. Opt., vol. 54, no. 5, pp. 1124–1137, Feb. 2015, doi: 10.1364/AO.54.001124.

[45] “Photonic Systems Integration (PSI) Laboratory | University of California San Diego.” http://psilab.ucsd.edu/research/Imaging%20Fiber%20Bundles/main.html (accessed Mar. 30, 2021).

[46] “Panoramic full-frame imaging with monocentric lenses and curved fiber.” https://spie.org/news/6666-panoramic-full-frame-imaging-with-monocentric-lenses-and-curved-fiber-bundles (accessed Mar. 30, 2021).

[47] J. A. Harrington, Infrared Fibers and Their Applications. SPIE Press, 2004.

[48] N. Ortega-Quijano, F. Fanjul-Vélez, and J. L. Arce-Diego, “Optical crosstalk influence in fiber imaging endoscopes design,” Opt. Commun., vol. 283, no. 4, pp. 633–638, Feb. 2010, doi: 10.1016/j.optcom.2009.10.075.

[49] I. Stamenov et al., “Panoramic monocentric imaging using fiber-coupled focal planes,” Opt. Express, vol. 22, no. 26, pp. 31708–31721, Dec. 2014, doi: 10.1364/OE.22.031708.

[50] Y. Lavi, A. Millo, and A. Katzir, “Flexible ordered bundles of infrared transmitting silver-halide fibers: design, fabrication, and optical measurements,” Appl. Opt., vol. 45, no. 23, pp. 5808–5814, Aug. 2006, doi: 10.1364/AO.45.005808.

[51] E. Rave, L. Nagli, and A. Katzir, “Ordered bundles of infrared-transmitting AgClBr fibers: optical characterization of individual fibers,” Opt. Lett., vol. 25, no. 17, pp. 1237–1239, Sep. 2000, doi: 10.1364/ol.25.001237.

[52] M. Saito, M. Takizawa, S. Sakuragi, and F. Tanei, “Infrared image guide with bundled As–S glass fibers,” Appl. Opt., vol. 24, no. 15, pp. 2304–2308, Aug. 1985, doi: 10.1364/AO.24.002304.

[53] F. Chenard, O. Alvarez, D. Gibson, L. B. Shaw, and J. Sanghera, “Mid-infrared imaging fiber bundle,” in Advanced Optics for Defense Applications: UV through LWIR II, May 2017, vol. 10181, p. 101810V, doi: 10.1117/12.2269076.

[54] B. Zhang et al., “High-resolution chalcogenide fiber bundles for infrared imaging,” Opt. Lett., vol. 40, no. 19, pp. 4384–4387, Oct. 2015, doi: 10.1364/OL.40.004384.

[55] J. Nishii, T. Yamashita, T. Yamagishi, C. Tanaka, and H. Sone, “Coherent infrared fiber image bundle,” Appl. Phys. Lett., vol. 59, no. 21, pp. 2639–2641, Nov. 1991, doi: 10.1063/1.105923.

[56] A. Ventura et al., “Flexible Mid-IR fiber bundle for thermal imaging of inaccessible areas,” Opt. Express, vol. 27, no. 15, pp. 20259–20272, Jul. 2019, doi: 10.1364/OE.27.020259.

[57] S. Qi et al., “High-resolution chalcogenide fiber bundles for longwave infrared imaging,” Opt. Express, vol. 25, no. 21, pp. 26160–26165, Oct. 2017, doi: 10.1364/OE.25.026160.

[58] J. D. Musgraves, J. Hu, and L. Calvez, Springer Handbook of Glass. Springer Nature, 2019.

[59] J. A. Harrington, “A Review of IR Transmitting, Hollow Waveguides,” Fiber Integr. Opt., vol. 19, no. 3, pp. 211–227, Jul. 2000, doi: 10.1080/01468030050058794.

[60] U. Gal, J. Harrington, M. Ben-David, C. Bledt, N. Syzonenko, and I. Gannot, “Coherent hollow-core waveguide bundles for thermal imaging,” Appl. Opt., vol. 49, no. 25, pp. 4700–4709, Sep. 2010, doi: 10.1364/AO.49.004700.

[61] J. M. Kriesel, G. M. Hagglund, N. Gat, V. Spagnolo, and P. Patimisco, “Spatial mode filtering of mid-infrared (mid-IR) laser beams with hollow core fiber optics,” in Quantum Sensing and Nanophotonic Devices XI, Jan. 2014, vol. 8993, p. 89930V, doi: 10.1117/12.2040018.

[62] C. M. Smith et al., “Low-loss hollow-core silica/air photonic bandgap fibre,” Nature, vol. 424, no. 6949, Art. no. 6949, Aug. 2003, doi: 10.1038/nature01849.

[63] M. S. Habib, J. E. Antonio-Lopez, C. Markos, A. Schülzgen, and R. Amezcua-Correa, “Single-mode, low loss hollow-core anti-resonant fiber designs,” Opt. Express, vol. 27, no. 4, pp. 3824–3836, Feb. 2019, doi: 10.1364/OE.27.003824.

[64] R. F. Cregan et al., “Single-Mode Photonic Band Gap Guidance of Light in Air,” Science, vol. 285, no. 5433, pp. 1537–1539, Sep. 1999, doi: 10.1126/science.285.5433.1537.

[65] M. A. Duguay, Y. Kokubun, T. L. Koch, and L. Pfeiffer, “Antiresonant reflecting optical waveguides in SiO2-Si multilayer structures,” Appl. Phys. Lett., vol. 49, no. 1, pp. 13–15, Jul. 1986, doi: 10.1063/1.97085.

[66] A. N. Kolyadin, A. F. Kosolapov, A. D. Pryamikov, A. S. Biriukov, V. G. Plotnichenko, and E. M. Dianov, “Light transmission in negative curvature hollow core fiber in extremely high material loss region,” Opt. Express, vol. 21, no. 8, pp. 9514–9519, Apr. 2013, doi: 10.1364/OE.21.009514.

[67] C. Wei, R. J. Weiblen, C. R. Menyuk, and J. Hu, “Negative curvature fibers,” Adv. Opt. Photonics, vol. 9, no. 3, pp. 504–561, Sep. 2017, doi: 10.1364/AOP.9.000504.

[68] F. Yu and J. C. Knight, “Spectral attenuation limits of silica hollow core negative curvature fiber,” Opt. Express, vol. 21, no. 18, pp. 21466–21471, Sep. 2013, doi: 10.1364/OE.21.021466.

[69] T. Kobayashi, T. Katagiri, and Y. Matsuura, “Multi-element hollow-core anti-resonant fiber for infrared thermal imaging,” Opt. Express, vol. 24, no. 23, pp. 26565–26574, Nov. 2016, doi: 10.1364/OE.24.026565.

[70] W. Belardi, “Design and Properties of Hollow Antiresonant Fibers for the Visible and Near Infrared Spectral Range,” J. Light. Technol., vol. 33, no. 21, pp. 4497–4503, Nov. 2015, doi: 10.1109/JLT.2015.2477775.

[71] L. Vincetti, “Empirical formulas for calculating loss in hollow core tube lattice fibers,” Opt. Express, vol. 24, no. 10, pp. 10313–10325, May 2016, doi: 10.1364/OE.24.010313.

[72] N. S. Kapany and R. J. Simms, “Recent developments in infrared fiber optics∗,” Infrared Phys., vol. 5, no. 2, pp. 69–80, Jun. 1965, doi: 10.1016/0020-0891(65)90009-6.

[73] J. Nishii, S. Morimoto, I. Inagawa, R. Iizuka, T. Yamashita, and T. Yamagishi, “Recent advances and trends in chalcogenide glass fiber technology: a review,” J. Non-Cryst. Solids, vol. 140, pp. 199–208, Jan. 1992, doi: 10.1016/S0022-3093(05)80767-7.

[74] G. Tao, S. Shabahang, E.-H. Banaei, J. J. Kaufman, and A. F. Abouraddy, “Multimaterial preform coextrusion for robust chalcogenide optical fibers and tapers,” Opt. Lett., vol. 37, no. 13, pp. 2751–2753, Jul. 2012, doi: 10.1364/OL.37.002751.

[75] G. Tao, S. Shabahang, S. Dai, and A. F. Abouraddy, “Multimaterial disc-to-fiber approach to efficiently produce robust infrared fibers,” Opt. Mater. Express, vol. 4, no. 10, pp. 2143–2149, Oct. 2014, doi: 10.1364/OME.4.002143.

[76] G. Tao et al., “Robust multimaterial tellurium-based chalcogenide glass fibers for mid-wave and long-wave infrared transmission,” Opt. Lett., vol. 39, no. 13, pp. 4009–4012, Jul. 2014, doi: 10.1364/OL.39.004009.

[77] T. M. Monro, Y. D. West, D. W. Hewak, N. G. R. Broderick, and D. J. Richardson, “Chalcogenide holey fibres,” Electron. Lett., vol. 36, no. 24, pp. 1998–2000, Nov. 2000, doi: 10.1049/el:20001394.

[78] B. Bureau, S. Maurugeon, F. Charpentier, J.-L. Adam, C. Boussard-Plédel, and X.-H. Zhang, “Chalcogenide Glass Fibers for Infrared Sensing and Space Optics,” Fiber Integr. Opt., vol. 28, no. 1, pp. 65–80, Jan. 2009, doi: 10.1080/01468030802272542.

[79] A. F. Kosolapov et al., “Demonstration of CO_2-laser power delivery through chalcogenide-glass fiber with negative-curvature hollow core,” Opt. Express, vol. 19, no. 25, pp. 25723–25728, Dec. 2011, doi: 10.1364/OE.19.025723.

[80] B. M. A. Rahman, F. A. Fernandez, and J. B. Davies, “Review of finite element methods for microwave and optical waveguides,” Proc. IEEE, vol. 79, no. 10, pp. 1442–1448, Oct. 1991, doi: 10.1109/5.104219.

[81] “Detailed Explanation of the Finite Element Method (FEM).” https://www.comsol.com/multiphysics/finite-element-method (accessed Nov. 13, 2020).

[82] A. Yariv, “Coupled-mode theory for guided-wave optics,” IEEE J. Quantum Electron., vol. 9, no. 9, pp. 919–933, Sep. 1973, doi: 10.1109/JQE.1973.1077767.

[83] W.-P. Huang, “Coupled-mode theory for optical waveguides: an overview,” JOSA A, vol. 11, no. 3, pp. 963–983, Mar. 1994, doi: 10.1364/JOSAA.11.000963.

[84] K. L. Reichenbach and C. Xu, “Numerical analysis of light propagation in image fibers or coherent fiber bundles,” Opt. Express, vol. 15, no. 5, pp. 2151–2165, Mar. 2007, doi: 10.1364/OE.15.002151.

[85] R. E. Collin, Field Theory of Guided Waves. IEEE Press, 1990.

[86] B. E. A. Saleh and M. C. Teich, Fundamentals of Photonics. Wiley, 2007.

[87] S. L. Chuang, Physics of Optoelectronic Devices. Wiley, 1995.

[88] K. Okamoto, Fundamentals of Optical Waveguides. Academic Press, 2006.

[89] E. Snitzer, “Cylindrical Dielectric Waveguide Modes*,” JOSA, vol. 51, no. 5, pp. 491–498, May 1961, doi: 10.1364/JOSA.51.000491.

[90] K. Kawano and T. Kitoh, Introduction to Optical Waveguide Analysis: Solving Maxwell’s Equation and the Schrödinger Equation. John Wiley & Sons, 2004.

[91] A. W. Snyder, “Coupled-Mode Theory for Optical Fibers,” JOSA, vol. 62, no. 11, pp. 1267–1277, Nov. 1972, doi: 10.1364/JOSA.62.001267.

[92] G. Bellanca, P. Orlandi, and P. Bassi, “Assessment of the orthogonal and non-orthogonal coupled-mode theory for parallel optical waveguide couplers,” JOSA A, vol. 35, no. 4, pp. 577–585, Apr. 2018, doi: 10.1364/JOSAA.35.000577.

[93] H. A. Haus, W. P. Huang, and A. W. Snyder, “Coupled-mode formulations,” Opt. Lett., vol. 14, no. 21, pp. 1222–1224, Nov. 1989, doi: 10.1364/OL.14.001222.

[94] A. W. Snyder and A. Ankiewicz, “Optical fiber couplers-optimum solution for unequal cores,” J. Light. Technol., vol. 6, no. 3, pp. 463–474, Mar. 1988, doi: 10.1109/50.4024.

[95] A. W. Snyder and A. Ankiewicz, “Fibre couplers composed of unequal cores,” Electron. Lett., vol. 22, no. 23, pp. 1237–1238, Nov. 1986, doi: 10.1049/el:19860848.

[96] A. W. Snyder, A. Ankiewicz, and A. Altintas, “Fundamental error of recent coupled mode formulations,” Electron. Lett., vol. 20, no. 23, pp. 1097–1098, 1987, doi: 10.1049/el:19870766.

[97] H. S. Huang and H.-C. Chang, “Vector coupled-mode analysis of coupling between two identical optical fiber cores,” Opt. Lett., vol. 14, no. 1, pp. 90–92, Jan. 1989, doi: 10.1364/OL.14.000090.

[98] A. W. Snyder and J. Love, Optical Waveguide Theory. Springer Science & Business Media, 2012.

[99] Chih-Sheng Chang and Hung-Chun Chang, “Vector normal modes on two-core optical fibers. I. The normal mode solutions,” J. Light. Technol., vol. 15, no. 7, pp. 1213–1224, Jul. 1997, doi: 10.1109/50.596968.

[100] A. W. Snyder and P. McIntyre, “Crosstalk between light pipes,” JOSA, vol. 66, no. 9, pp. 877–882, Sep. 1976, doi: 10.1364/JOSA.66.000877.

[101] K. L. Reichenbach and C. Xu, “Independent core propagation in two-core photonic crystal fibers resulting from structural nonuniformities,” Opt. Express, vol. 13, no. 25, pp. 10336–10348, Dec. 2005, doi: 10.1364/OPEX.13.010336.

[102] Z. Wang, T. Taru, T. A. Birks, J. C. Knight, Y. Liu, and J. Du, “Coupling in dual-core photonic bandgap fibers: theory and experiment,” Opt. Express, vol. 15, no. 8, pp. 4795–4803, Apr. 2007, doi: 10.1364/OE.15.004795.

[103] T. Sakamoto, T. Mori, M. Wada, T. Yamamoto, F. Yamamoto, and K. Nakajima, “Strongly-coupled multi-core fiber and its optical characteristics for MIMO transmission systems,” Opt. Fiber Technol., vol. 35, pp. 8–18, Feb. 2017, doi: 10.1016/j.yofte.2016.07.010.

[104] Horng Shou Huang and Hung-Chun Chang, “Analysis of optical fiber directional coupling based on the HE/sub 11/ modes. I. The identical-core case,” J. Light. Technol., vol. 8, no. 6, pp. 823–881, Jun. 1990, doi: 10.1109/50.54498.

[105] Horng-Shou Huang and Hung-Chun Chang, “Analysis of optical fiber directional coupling based on the HE/sub 11/ modes. II. The nonidentical-core case,” J. Light. Technol., vol. 8, no. 6, pp. 832–837, Jun. 1990, doi: 10.1109/50.54499.

[106] Chih-Sheng Chang and Hung-Chun Chang, “Theory of the circular harmonics expansion method for multiple-optical-fiber system,” J. Light. Technol., vol. 12, no. 3, pp. 415–417, Mar. 1994, doi: 10.1109/50.285344.

[107] Chih-Sheng Chang and Hung-Chun Chang, “Vector normal modes on two-core optical fibers. II. The modal cutoffs,” J. Light. Technol., vol. 15, no. 7, pp. 1225–1232, Jul. 1997, doi: 10.1109/50.596969.

[108] E. Yamashita, S. Ozeki, and K. Atsuki, “Modal analysis method for optical fibers with symmetrically distributed multiple cores,” J. Light. Technol., vol. 3, no. 2, pp. 341–346, Apr. 1985, doi: 10.1109/JLT.1985.1074188.

[109] T. P. White et al., “Multipole method for microstructured optical fibers. I. Formulation,” JOSA B, vol. 19, no. 10, pp. 2322–2330, Oct. 2002, doi: 10.1364/JOSAB.19.002322.

[110] B. T. Kuhlmey et al., “Multipole method for microstructured optical fibers. II. Implementation and results,” JOSA B, vol. 19, no. 10, pp. 2331–2340, Oct. 2002, doi: 10.1364/JOSAB.19.002331.

[111] W. Wijngaard, “Guided normal modes of two parallel circular dielectric rods,” JOSA, vol. 63, no. 8, pp. 944–950, Aug. 1973, doi: 10.1364/JOSA.63.000944.

[112] K. M. Lo, R. C. McPhedran, I. M. Bassett, and G. W. Milton, “An electromagnetic theory of dielectric waveguides with multiple embedded cylinders,” J. Light. Technol., vol. 12, no. 3, pp. 396–410, Mar. 1994, doi: 10.1109/50.285321.

[113] X. Chen, K. L. Reichenbach, and C. Xu, “Experimental and theoretical analysis of core-to-core coupling on fiber bundle imaging,” Opt. Express, vol. 16, no. 26, pp. 21598–21607, Dec. 2008, doi: 10.1364/OE.16.021598.

[114] M. Poulain, M. Poulain, and J. Lucas, “Verres fluores au tetrafluorure de zirconium proprietes optiques d’un verre dope au Nd3+,” Mater. Res. Bull., vol. 10, no. 4, pp. 243–246, Apr. 1975, doi: 10.1016/0025-5408(75)90106-3.

[115] M. Poulain, M. Chanthanasinh, and J. Lucas, “Nouveaux verres fluores,” Mater. Res. Bull., vol. 12, no. 2, pp. 151–156, Feb. 1977, doi: 10.1016/0025-5408(77)90157-X.

[116] D. Tran, G. Sigel, and B. Bendow, “Heavy metal fluoride glasses and fibers: A review,” J. Light. Technol., vol. 2, no. 5, pp. 566–586, Oct. 1984, doi: 10.1109/JLT.1984.1073661.

[117] I. Cozmuta, S. Cozic, M. Poulain, S. Poulain, and J. R. L. Martini, “Breaking the silica ceiling: ZBLAN-based opportunities for photonics applications,” in Optical Components and Materials XVII, Mar. 2020, vol. 11276, p. 112760R, doi: 10.1117/12.2542350.

[118] “Fluoride glasses,” Le Verre Fluoré. https://leverrefluore.com/scientific-world/fluoride-glasses/ (accessed Mar. 07, 2021).

[119] “Summary - Vitron Spezialwerkstoffe,” VITRON Spezialwerkstoffe GmbH. https://www.vitron.de/en/ir-glasses/summary.php (accessed Mar. 07, 2021).

[120] “Infrared Materials product variants | SCHOTT.” /en-us/products/ir-materials/product-variants (accessed Mar. 07, 2021).

[121] “Chalcogenide Glass Fibers | IRFlex Corporation.” https://irflex.com/products/irf-s-series/ (accessed Mar. 07, 2021).

[122] “Infrared Fiber Optics | IRFlex Corporation.” https://irflex.com/products/irf-se-series/ (accessed Mar. 07, 2021).

[123] “Specifications - Vitron Spezialwerkstoffe,” VITRON Spezialwerkstoffe GmbH. https://www.vitron.de/en/ir-glasses/specifications.php (accessed Mar. 05, 2021).

[124] I. Inagawa, R. Iizuka, T. Yamagishi, and R. Yokota, “Optical and thermal properties of chalcogenide Ge-As-Se-Te glasses for IR fibers,” J. Non-Cryst. Solids, vol. 95–96, pp. 801–808, Dec. 1987, doi: 10.1016/S0022-3093(87)80684-1.

[125] S. Shabahang, G. Tao, J. J. Kaufman, and A. F. Abouraddy, “Dispersion characterization of chalcogenide bulk glass, composite fibers, and robust nanotapers,” JOSA B, vol. 30, no. 9, pp. 2498–2506, Sep. 2013, doi: 10.1364/JOSAB.30.002498.

[126] W. S. Rodney, I. H. Malitson, and T. A. King, “Refractive Index of Arsenic Trisulfide,” JOSA, vol. 48, no. 9, pp. 633–636, Sep. 1958, doi: 10.1364/JOSA.48.000633.

[127] A. Ravagli, C. Craig, J. Lincoln, and D. W. Hewak, “Ga-La-S-Se glass for visible and thermal imaging,” Adv. Opt. Technol., vol. 6, no. 2, pp. 131–136, Apr. 2017, doi: 10.1515/aot-2016-0069.

[128] X. Zhang et al., “Complex refractive indices measurements of polymers in visible and near-infrared bands,” Appl. Opt., vol. 59, no. 8, pp. 2337–2344, Mar. 2020, doi: 10.1364/AO.383831.

[129] “Properties: Supplier Data - Polyetherimide (PEI) (Goodfellow),” AZoM.com. https://www.azom.com/properties.aspx?ArticleID=1883 (accessed Mar. 06, 2021).

[130] “Overview of materials for Polyetherimide (PEI).” http://www.matweb.com/search/DataSheet.aspx?MatGUID=65baf7a4f90c4a54a6ace03e16b1125b (accessed Mar. 05, 2021).

[131] “polyetherimide information and properties.” https://www.polymerprocessing.com/polymers/PEI.html (accessed Mar. 05, 2021).

[132] H. R. Philipp, D. G. L. Grand, H. S. Cole, and Y. S. Liu, “The optical properties of a polyetherimide,” Polym. Eng. Sci., vol. 29, no. 22, pp. 1574–1578, 1989, doi: https://doi.org/10.1002/pen.760292205.

[133] “Solvay Specialty Polymers Veradel® AG-320 Polyethersulfone (PESU).” http://www.matweb.com/search/datasheet_print.aspx?matguid=7e21fe9ba4e14e95a879e83092d47814 (accessed Mar. 07, 2021).

[134] “Polyethersulfone (PESU) - Polyether Sulfone (PES) - Matmatch.” https://matmatch.com/materials/mbas038-polyethersulfone-pesu- (accessed Mar. 07, 2021).

[135] “Sulfones-Optical-Properties_EN-v2.0_0.pdf.” Accessed: Mar. 08, 2021. [Online]. Available: https://www.solvay.com/sites/g/files/srpend221/files/2018-10/Sulfones-Optical-Properties_EN-v2.0_0.pdf.

[136] “poly(ethersulfone) information and properties.” https://www.polymerprocessing.com/polymers/PES.html (accessed Mar. 05, 2021).

[137] “Overview of materials for Fluorinated Ethylene Propylene (FEP), Molded/Extruded.” http://www.matweb.com/search/DataSheet.aspx?MatGUID=c782af4519d949349d7c771ff6953314 (accessed Mar. 05, 2021).

[138] “TexLoc Library - FEP Properties.” http://www.texloc.com/closet/cl_fep_properties.html (accessed Mar. 07, 2021).

[139] “What Is Polyetherimide (PEI)?” https://www.thomasnet.com/insights/what-is-polyetherimide-pei-/ (accessed Mar. 07, 2021).

[140] “Polyethersulfone (PESU): Features, Strengths and Limitations.” https://omnexus.specialchem.com/selection-guide/polyethersulfone-pes-thermoplastic (accessed Mar. 07, 2021).

[141] “FEP.” http://polymerdatabase.com/Polymer%20Brands/FEP.html (accessed Mar. 07, 2021).

[142] “Glass Transition Temperature (Tg) of Plastics - Definition & Values.” https://omnexus.specialchem.com/polymer-properties/properties/glass-transition-temperature (accessed Mar. 09, 2021).

[143] “Polyetherimide - online catalogue source - supplier of research materials in small quantities - Goodfellow.” http://www.goodfellow.com/E/Polyetherimide.html (accessed Mar. 09, 2021).

[144] “Polyethersulfone - online catalog source - supplier of research materials in small quantities - Goodfellow.” http://www.goodfellowusa.com/A/Polyethersulfone.html (accessed Mar. 09, 2021).

[145] “Fluorinated Ethylene Propylene Copolymer - online catalogue source - supplier of research materials in small quantities - Goodfellow.” http://www.goodfellow.com/E/Fluorinated-Ethylene-Propylene-Copolymer.html (accessed Mar. 09, 2021).

[146] X. Zhang, J. Qiu, J. Zhao, X. Li, and L. Liu, “Complex refractive indices measurements of polymers in infrared bands,” J. Quant. Spectrosc. Radiat. Transf., vol. 252, p. 107063, Sep. 2020, doi: 10.1016/j.jqsrt.2020.107063.

[147] “Wayback Machine,” Feb. 16, 2007. https://web.archive.org/web/20070216065646/http://las.perkinelmer.com/content/TechnicalInfo/TCH_FTIRATR.pdf (accessed Mar. 29, 2021).

[148] B.-K. Chen, C.-T. Su, M.-C. Tseng, and S.-Y. Tsay, “Preparation of Polyetherimide Nanocomposites with Improved Thermal, Mechanical and Dielectric Properties,” Polym. Bull., vol. 57, no. 5, pp. 671–681, Sep. 2006, doi: 10.1007/s00289-006-0630-3.

[149] E. Hecht, Optics. Pearson Education, Incorporated, 2017.

[150] J. Amirloo, S. S. Saini, and M. Dagenais, “Comprehensive study of antireflection coatings for mid-infrared lasers,” J. Vac. Sci. Technol. A, vol. 34, no. 6, p. 061505, Nov. 2016, doi: 10.1116/1.4963373.

[151] G. Tao et al., “Infrared fibers,” Adv. Opt. Photonics, vol. 7, no. 2, pp. 379–458, Jun. 2015, doi: 10.1364/AOP.7.000379.

[152] A. Nc, “FY 2006 Miniature Spherical Retroreflectors Final Report,” p. 31.

[153] G. Tao, A. M. Stolyarov, and A. F. Abouraddy, “Multimaterial Fibers,” Int. J. Appl. Glass Sci., vol. 3, no. 4, pp. 349–368, 2012, doi: https://doi.org/10.1111/ijag.12007.

[154] B. Luo et al., “Midinfrared Supercontinuum Generation in As2Se3–As2S3 Chalcogenide Glass Fiber With High NA,” J. Light. Technol., vol. 35, no. 12, pp. 2464–2469, Jun. 2017, doi: 10.1109/JLT.2016.2623639.